Theses and Dissertations                                    Student Graduate Works

6-16-2016

# Design, Manufacturing, and Testing of a Small Through-Flow Wave for Use Within the Brayton Cycle

Micahel J. McClearn

Recommended Citation

McClearn, Micahel J., "Design, Manufacturing, and Testing of a Small Through-Flow Wave for Use Within the Brayton Cycle" (2016). *Theses and Dissertations*. 480.
https://scholar.afit.edu/etd/480

Design, Manufacturing, and Testing of a Small
Through-Flow Wave Rotor for Use Within the
Brayton Cycle

THESIS

Michael J. McClearn, 2$^{nd}$ Lieutenant, USAF

AFIT-ENY-MS-16-J-054

**DEPARTMENT OF THE AIR FORCE**
**AIR UNIVERSITY**

# AIR FORCE INSTITUTE OF TECHNOLOGY

**Wright-Patterson Air Force Base, Ohio**

DISTRIBUTION STATEMENT A
APPROVED FOR PUBLIC RELEASE; DISTRIBUTION UNLIMITED.

The views expressed in this document are those of the author and do not reflect the official policy or position of the United States Air Force, the United States Department of Defense or the United States Government. This material is declared a work of the U.S. Government and is not subject to copyright protection in the United States.

AFIT-ENY-MS-16-J-054

DESIGN, MANUFACTURING, AND TESTING OF A SMALL

THROUGH-FLOW WAVE ROTOR FOR USE WITHIN THE BRAYTON CYCLE

THESIS

Presented to the Faculty

Department of Aeronautics and Astronautics

Graduate School of Engineering and Management

Air Force Institute of Technology

Air University

Air Education and Training Command

in Partial Fulfillment of the Requirements for the

Degree of Degree of Master of Science

Michael J. McClearn, B.S.

2$^{\text{nd}}$ Lieutenant, USAF

June 2016

AFIT-ENY-MS-16-J-054

DESIGN, MANUFACTURING, AND TESTING OF A SMALL

THROUGH-FLOW WAVE ROTOR FOR USE WITHIN THE BRAYTON CYCLE

Michael J. McClearn, B.S.
2$^{\text{nd}}$ Lieutenant, USAF

Committee Membership:

Marc D. Polanka, PhD
Chairman

Fred R. Schauer, PhD
Member

Adam L. Comer, Captain, USAF, PhD
Member

# Abstract

With the ever growing popularity of drones and other unmanned aerial vehicles for military, commercial, and private usage, there is a desire to improve performance in terms of range, altitude, and flight speed. Current technology uses either electric motors or internal combustion engines: both piston and jet engine types. These sorts of engines undergo significant efficiency degradation as their size decreases. While some efficiency may be recovered via intensive design studies, the cycles are approaching the limit to their operating physics. A possible solution to this is to change the operating physics to something more immune to scaling losses; a pressure exchange device known as a wave rotor is one option. A wave rotor operates via oscillating pressure waves in order to compress the gas as opposed to the mechanical compression utilized by conventional engines. This thesis outlines the design, manufacture, and component testing of a wave rotor within the Brayton cycle. While the focus of this research was the wave rotor, included in the design and testing were the many support components necessary to drive the cycle, notably a small can-type combustor. Using a NASA developed quasi one dimensional CFD code, the wave rotor cycle was designed to power a kilowatt sized Class 2 UAVs. After the CFD modeling, hardware design and manufacture began on the various components. After manufacture, the various components were tested including the venturis, the combustor, and the wave rotor itself. The component testing showed great promise for the full rig testing. Hardware build up and the test plan is ongoing but expected to show efficiency gains when compared to similar sized combustion engines. Improved efficiency gains will significantly decrease the operating costs of small drones while improving range and altitude performance to all operators.

# Acknowledgements

Thank you does not adequately describe the gratitude towards my friends and family that have supported me during this time. Between the sparse communication and minimal free time, they were always willing to offer encouragement and words of advice. I would also like to thank my advisor, Dr. Marc Polanka, for his guidance throughout this entire process. I'm not sure how much time was spent reading through my drafts and trying to decipher what exactly I meant, but it was significant. I'd also like to thank my thesis committee for their help and support as well and the sponsors, MIT Lincoln Labs, for their financial support.

There is one final group of people that must be thanked and that is the Detonation Group within AFRL. Dr. John Hoke, Dr. Matt Fotia, Dr. Brian Sell, Mr. Andy Naples, Dr. Chris Stevens, Dr. Josh Codoni, Capt Scott Theuerkauf, Mr. Nick Grannan, and Dr. Kevin Cho. In one way or another, you have all helped me immensely. Whether it was encouragement or taking time to show me how to do something, I thank you. Mr. Curtis Rice, Mr. Matt Petersen, and Mr. Justin Goeffna, the lab techs, I had some strange requests for both of you but never once was I disappointed with the results and often, a better way to do something. Dr. Dan Paxson, NASA Wave Rotor guru, thank you for the code, it made life interesting. Lastly, Lt Mark Mataczynski, from the few early mornings to the hours of build up, I could not have done this without your help.

Michael J. McClearn

v

www.manaraa.com

# Table of Contents

# List of Figures

x

xi

# List of Tables

# List of Abbreviations

Abbreviation

ABB     Asea Brown Boveri

AFIT    Air Force Institute of Technology

AFRL    Air Force Research Laboratory

BBC     Brown Boveri Company

CAD     Computer Aided Design

CFD     Computational Fluid Dynamics

CI        Compressor Inlet

CO       Compressor Outlet

COTS    Commercial of the Shelf

DMLS    Direct Metal Laser Sintering

DoD     Department of Defense

ESC     Electronic Speed Controller

EGR     Exhaust Gas Recirculation

FAA     Federal Aviation Authority

FEA     Finite Element Analysis

FMRA   FAA Modernization and Reform Act of 2012

GRC     John H. Glenn Research Center

IC        Internal Combustion

IUPUI   Indiana University-Purdue University at Indianapolis

ISSI     Innovative Scientific Solutions, Inc

MIT     Massachusetts Institute of Technology

MSU     Michigan State University

Abbreviation

NASA   National Aeronautics and Space Administration

PWS   Pressure Wave Supercharger

Q1D   quasi-one dimensional

OPR   Overall Pressure Ratio

RC   Radio Controlled

TO   Turbine Outlet

TI   Turbine Inlet

UAV   Unmanned Aerial Vehicle

# List of Symbols

Symbol

| | |
|---|---|
| $\eta$ | efficiency |
| $\dot{W}_o$ | Work Out |
| $\dot{Q}$ | Heat |
| $T_{41}$ | Turbine Inlet Temperature |
| $H_c$ | Heat of Combustion |
| $EI_{CO}$ | Emissions Index of Carbon Dioxide |
| $EI_{C_xH_y}$ | Emissions Index of the Unburned Hydrocarbons |
| $M$ | Mach Number |
| $T_s$ | Static Temperature |
| $a$ | Sonic Velocity |
| $ke$ | Specific Kinetic Energy |
| $\gamma$ | Ratio of Specific Heats |
| $\rho$ | Density |
| $\mu$ | Kinematic Viscosity |
| $MF$ | Mass Flux |
| $R$ | Specific Gas Constant |
| $A_{web}$ | Web Area |
| $A/F$ | Air to Fuel Ratio |
| $LHV$ | Lower Heating Value of the Fuel |
| $C_P$ | Specific Heat (Constant Pressure) |
| $A/F_{stoic}$ | Stoichiometric Air to Fuel Ratio |
| $q$ | Dynamic Pressure |

Symbol Page

*v*    Velocity

*d*    Throat Diameter

*D*    Inlet Diameter

*C*    Discharge Coefficient

*P*    Pressure

*T*    Temperature

$P_0$    Stagnation Pressure

# DESIGN, MANUFACTURING, AND TESTING OF A SMALL THROUGH-FLOW WAVE ROTOR FOR USE WITHIN THE BRAYTON CYCLE

## I. Introduction

### 1.1 General Issue

Recent years have seen a dramatic rise in the popularity of smaller drones and Unmanned Aerial Vehicles, (UAV) in both commercial industry as well as the Department of Defense (DoD). In this context, smaller refers to Class 1 and Class 2 aircraft, less than 55 pounds (24.95 kg), as defined by the Federal Aviation Authority (FAA) Modernization and Reform Act of 2012 (FMRA) Section 336. Previously, these have been called model or remote controlled aircraft. While many of these drones use electric motors, many others utilize internal combustion (IC) engines or miniature gas turbine jet engines to achieve far greater power density. Often the IC engines are modified single cylinder piston engines from yard equipment such as lawn mowers and weed trimmers and, therefore, were not designed for the rapid altitude changes or simply even the altitude accompanying aerial usage. These altitude changes bring about changes in pressure, temperature, and density of the inlet air. Alternatively, the small jet engines are better able to handle the altitude changes but require greater quantities of fuel. However, both engine types suffer from efficiency issues at the lower mass flow rates given the size and ambient conditions of the operating regime.

While both engine types provide positives and negatives in their usage for powering small UAVs, IC engines generally have improved fuel efficiency at the smaller sizes while jet engines have a pronounced performance advantage. Performance en-

1

hancing modifications to IC engines include designs specific to aircraft or utilizing turbonormalization via superchargers, turbochargers, or pressure wave supercharging wave rotors. Although aircraft specific modifications may sound like a good idea, given the tremendous size range of model aircraft, it is hard to imagine a customized engine for every airframe. That becomes an engineering cost versus production quantity problem. In contrast, adding turbonormalizing equipment to existing designs does offer a boost in performance, but it lowers the efficiency of the system while increasing weight.

Jet engines suffer from a different type of problem as design variation is smaller with size changes. Their shortcoming is relative losses increase dramatically for smaller sized turbomachinery components within the jet engine. This results in the low efficiencies at the lower size and mass flow rates required for Class 1 and 2 aircraft. Little can be done to increase efficiency more than a few percent and, even so, the peak efficiency is lower than piston engines despite power and performance remaining higher.

A potential solution to both sets of issues is to use a wave rotor coupled to a combustor in a modified Brayton cycle configuration. A wave rotor is a dynamic pressure exchange device operating on the principle of oscillating pressure waves rather than mechanical compression in the form of rotating blades (jet engine) or a piston (IC). In this sort of configuration, a wave rotor would replace the turbomachinery components, the compressor and turbine, within the Brayton cycle configuration. This type of design would either convert the available energy within the exhaust into shaft-work and spin a propeller or exit through a nozzle to generate thrust. Wave rotors are able to maintain higher efficiencies at the smaller sizes when compared to jet engines and have comparable or better power and performance than turbo-normalized IC engines. Given the potential for this type of design, this research project focused on the cycle

2

design, component design, and building of a kilowatt power class wave rotor.

## 1.2 Objectives

The overarching objective of this research was to design and test a wave rotor design in a Brayton cycle configuration for use in powering a Class 1 or 2 UAV. Included in this objective was the desire to show operational feasibility while providing efficiency values for a range of mass flow rates and quantifying available power within the exhaust. To achieve the overarching objective, the process was divided into a series of intermediate phases:

1. Computationally model the Brayton cycle wave rotor using the NASA code developed by Paxson [1] [2] [3].

2. Design and manufacture the wave rotor hardware and accessories necessary to achieve the modeled cycle via computer aided design software.

3. Design and build the combustor necessary to drive the energy exchange for the wave rotor.

4. Test the wave rotor and combustor in an uncoupled manner.

5. Couple the wave rotor and the combustor for cycle validation.

6. Analyze off-design operation of the wave rotor.

## 1.3 Methodology

The intermediate steps were completed in a serial manner as information or components from the previous phase was needed for the next one. This subsection will briefly describe the process in which these phases were accomplished.

Because Mataczynski et al. [4] previously verified the accuracy of the National Aeronautics and Space Administration (NASA) quasi-one dimensional (Q1D) computational fluid dynamics (CFD) code at the low flow rates studied within this research,

3

no further validation of the code's accuracy was necessary prior to beginning the cycle design. This permitted immediate the work to design a kilowatt class wave rotor operating within the Brayton cycle. The cycle design yielded the exhaust conditions necessary to calculate the available power within the exit stream of the wave rotor system. It also gave the necessary physical parameters to design a wave rotor. This process and the results will be further detailed in Chapters 3 and 4.

With the cycle computed from the first step, a majority of the hardware was designed utilizing computer aided design (CAD) software. During this step, the wave rotor endwalls, rotor, and bearing arrangement were designed. Further work yielded a shroud design for the rotor and an estimated torque specification for a motor. Choosing the motor enabled the design of a motor mount. The overall mass flow rates through the system were calculated and venturis were designed and calibrated to measure the air flow into and out of the system. One of the most important results of this step was the realization that a custom combustor would be needed. The manufacture or purchase of some parts had to be done before finalizing other parts. All of this will be further detailed in Chapter 3.

The general design of the custom combustor's can and dome components were done with the help of Mr. David Burrus of Innovative Scientific Solutions, Inc (ISSI). The final design was accomplished within CAD software. Along with the can and dome of the combustor, the plumbing to and from the wave rotor endwalls upstream and downstream of the can was also specified. Additional design work was needed to build the separate setup for the testing and characterization of the combustor's performance. More information on this step can be found in Chapter 3.

The fourth step entailed testing the experimental components. The combustor's approximate fuel flow rates were characterized for the required outlet temperature. Other tests were accomplished to determine the operational range for mass flow, inlet

4

conditions, and start up. Concurrent with the combustor tests was mechanical testing on the wave rotor to ensure no vibromechanical modes occurred near the operating speed and further that no detrimental modes occurred beneath the operating speed that would impede the rotor's ability to achieve the design speed. All of the details for these processes are given in Chapters 3 and 4.

The final step necessary to reach the baseline condition of the primary objective was to couple the two separate, experimental components together. This coupling and journey to design point operation occurred over a few substeps including cold flow testing that used pressurized air to leak check the system and finally the hot run testing at the design point to validate the computational model and report power available and cycle efficiency. Hot testing is ongoing.

This research aimed to design and build an alternative cycle, proof-of-concept engine to power small UAVs more efficiently than existing combustion engines. The wave rotor and the combustor were designed, manufactured, and experimentally tested to determine the available power within the exhaust stream as well as the overall efficiency of the cycle.

# II. Background

## 2.1 Introduction

Today's UAVs' operating environment is soaring higher and higher as technology pushes small commercial UAVs to higher altitudes. Despite the growth in operational range, the size of UAVs is only becoming smaller; thus forcing the size of its power supply to also become smaller. Though the majority of UAVs use battery powered electric motors, many of the more robust models utilize combustion powered engines to either drive a propeller or to generate thrust. However, as the engine size decreases, the engine efficiency decreases faster. This efficiency degradation is caused by a number of factors; however, a change in the forces dominating the losses from momentum based to viscous based is the primary factor for small engines, though its manifestation is different for each type.

Although there are many different ways to discuss efficiency, $\eta$, this research will use a fairly simple first law basis as defined in Equation 1. This equation defines the net thermal efficiency of a system at sea level static conditions where work out is represented by $\dot{W}_o$ and $\dot{Q}$ is the heat into the system.

$$\eta = \frac{\dot{W}_o}{\dot{Q}} \tag{1}$$

Regardless of how both work and heat to the system are calculated, the final result is invariant as long as all energy mechanisms are properly accounted for. Additionally, because Brayton cycle (jet), Diesel cycle, and Otto cycle (piston) engines are discussed in this research, keeping the efficiency definition broad and relatively simple allows for an easier comparison across cycle types. Given the low Mach numbers of UAVs, this is best compared to a propeller powering cycle so that propulsive efficiency can be neglected. Neglecting propulsive efficiency is reasonable due to the downstream

6

turbine extracting work from the flow and minimizing the energy in the flow exiting to ambient.

In order to accurately compare this to a propeller driving system, a number of further assumptions must be made about the downstream turbine such as the polytropic efficiency and the propeller turbine power balance. Because of the uncertainty in estimating the turbine values, the research more readily compares to a turbojet analysis utilizing specific kinetic energy further discussed in Section 3.1. Although no propulsive efficiency comparison is made, the uncertainty with the assumption is known.

A possible counteraction to this loss of efficiency as size decreases is to utilize a wave rotor. Wave rotors, as compared to conventional engines, operate on fundamentally different principles. Both conventional engines and wave rotors will be discussed in depth throughout this chapter.

The principles of mechanical compression upon which conventional cycles operate cause the engines to lose performance and efficiency at lower flow rates. Wave rotors are not affected by the same limitations, thus they do not suffer the same loss mechanisms. This makes them viable candidates for use in small scale UAVs. The operating principles, history, and design of wave rotors will be discussed including previous computational models.

## 2.2    Issues with Conventional Small Engines

Historically, small engines providing only a few kilowatts of power were used for mundane tasks such as operating a leaf blower or powering a chainsaw. Today, the market for similarly sized engines to power UAVs is growing rapidly and this market desires more power, greater efficiency, and ever smaller quantities of both mass and volume. This demand has motivated research into this area for both gas turbines as

7

well as internal combustion piston engines.

### 2.2.1 Gas Turbines.

Gas turbine engines lose efficiency rapidly as mass flow decreases to less than 0.045 kg/s [5]. This is due to the size of the blades of the compressor and turbine rotors becoming so small that the viscous boundary layers become significant. Subsequently, the viscous losses grow relatively large with respect to the work done by these components. This forces the components to do more work for less output on a per unit work basis. A team at the Massachusetts Institute of Technology (MIT) examined micro-gas turbines in order to quantify and better understand these effects [6]. In order to baseline their study, Jacobson, et al. first examined the energy conversion efficiencies of high pressure ratio gas turbines such as those found in modern jet aircraft. They found these efficiencies to only be on the order of 40%-45% because driving the compressor requires significant amounts of power. In terms of energy conversion, this is essentially a loss. The compressor's large power consumption is due to adverse pressure gradient present across the system. This means it must force the air to flow from low pressure to high pressure as opposed to the turbine which uses the favorable pressure gradient across it to convert heat energy into work.

After the baselining, the work shifted to ultra-micro-gas turbines. These engines' volume was on the order of 1 cm$^3$. In order to manufacture these tiny engines, the team stacked silicon wafers and machined their components out of the stack. The manufacturing, as opposed to physics, was their limiting factor thus limiting their system to an overall pressure ratio (OPR) of about 3 or 4. It is important to note that this study occurred in the late 1990s when 3-D printing in general was still in its infancy and 3-D printing of metals was non-existent.

Their results were a combination of computational and experimental work. The experimental work demonstrated the trends however the values given are from the computational work. As expected, the team found more pronounced viscous effects largely due to the predominantly laminar flow caused by a factor of 100 decrease in Reynolds number. The larger internal drag effects stem from an approximately threefold increase in skin friction drag coefficient. This led to compressor and turbine efficiency estimates of less than 50% and approximately 60% respectively. Typically, compressor and turbine efficiencies for large modern engines in manned aircraft are 90% and 89%, respectively [7]. These losses and inefficiencies sum to a boundary layer estimated at 7% of the passage area resulting in a 30% reduction in normalized mass flow, while overcoming the Couette drag alone accounted for 25% of the power generation [6].

A more recent study in Italy examined micro-gas turbines up to 100 kW. Bianchi, et al. [8] examined these engines in two very different configurations. They examined a typical Brayton cycle configuration in which the compressor is first and is followed by the combustor and lastly, the turbine. This cycle also included a recuperator to preheat the fuel before injection into the combustion chamber. Their other configuration was an inverted Brayton cycle. This type of cycle inverts the position of the compressor and the turbine thus causing combustion to occur at lower pressures and lower temperature. Typically, this is undesired but at smaller scales such as this research, it works in the opposite manner. This works because the losses that occur during compression are greater than those across a turbine due to the unfavorable pressure gradient, thus allowing the compressor to act as an energy exchanger by converting the hot, low pressure gas to a cooler, above atmospheric pressure gas. This requires an area contraction to increase the density faster than the temperature is dropping.

The group published their results for the system as opposed to the components. Each system has a reported thermal efficiency, which is the amount of energy generated as opposed to the total potential of the reactants, and an electrical efficiency which correlates to power takeoffs to supply auxiliary power to other devices that a typical aircraft would have. The conventional cycle had peak efficiencies of 30.9% for electrical and 51.9% thermal whereas the inverted cycle improved these to 33.2% electrical and 64.9% thermal. The exact size of their test article was not published which makes these values difficult to use in a one to one comparison but gives potential target values for a device roughly the same order of magnitude in terms of power output as the wave rotor.

This all contributes to the physics based limitations for scaling gas turbine engines beyond a certain mass flow point. Eventually, the boundary layer becomes a significant amount of the passage area effectively acting as an area blockage and restricting the amount of mass flow able to pass through. Couette and Poiselle drag forces also become significant at this scale as fluid flow must occur no matter the device.

### 2.2.2 Internal Combusion Engines.

Given the physics based limitations of scaling gas turbine engines and the common availability of small IC engines, many small aircraft use repurposed IC engines as their power source. Often, drone and UAV companies will take the engine off a leaf blower, a weed trimmer, or a small lawnmower and modify it such that a propeller shaft can mate to the crankshaft (or a gearbox attached to the crank) and use the engine without any further modification.

Historically, this was not an issue as the radio controlled (RC) aircraft never went very high and stayed within viewing distance of the operator. The closer proximity and short flight times permitted easy refueling which led to the acceptance of an

10

inefficient engine from a fuel standpoint. Also, because the aircraft typically flew relatively close to the ground, the atmospheric conditions varied little from the ground [9]. This is not the case at higher altitudes. Every 1000 m increase in flight altitude results in pressure decreasing by about 11% and density decreasing by 9%. Husaboe found a 3.5% decrease in power for every 300 m increase in altitude for a single kW class IC engine [10].

Given all of this, there are two sidenotes; first, the small engine market previously lacked the demand to justify the investment for a more efficient power supply and second, the RC controller range and lack of real-time video streaming required the aircraft to stay close to the operator. Today, the market demand is increasing rapidly and real time, high definition streaming allows for beyond visual range flight. Present demands on altitude and aircraft size are beyond the range of the historic norm as IC engines decrease in efficiency faster than they drop in power produced as a function of size [11]. Thus a larger engine than desired is necessary to achieve the necessary power. A larger engine means a heavier aircraft and more fuel required onboard. This type of trend drives UAVs towards a larger size whereas the demand is for smaller and smaller sizes.

This discussion of IC engines to this point has focused on driving engines smaller and smaller. IC engines in the kilowatt power class share many of the loss mechanisms with their smaller counterparts, however, the heat transfer issue is not a dominant component. Rather, it is about 25% of the losses, on par with larger piston engines [12]. As cylinder displacement decreases in size, both engine power and fuel conversion efficiency decrease. While larger engines such as automobile, train, and ship engines have conversion efficiencies near 30% [12], Figure 1, produced by Horn et al.[13], showed the small engines are less than 20% and can be less than 10% for a 28cc engine.

11
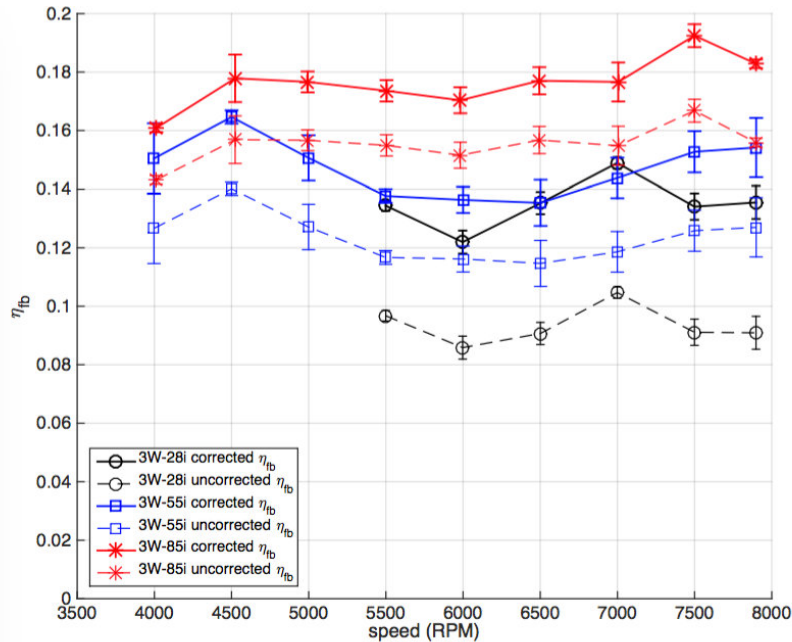
**Figure 1. Fuel Conversion Efficiency for Three 3W Two Stroke Engines Showing Corrected and Uncorrected Values [13]**

Menon, et al. [14] examined a variety of micro IC engines (less than 1 kW of power) ranging in size from 0.16 cm$^3$ to 7.5 cm$^3$ with power outputs from 8 W to 650 W. They found that the corresponding system efficiencies ranged from about 4% for the smallest engine to 12% for the 7.5 cm$^3$ engine. The reduction in efficiency as the engine size decreased is due primarily to mechanical and thermal losses. Although chemistry time scales do not scale similarly to size, the issue with making piston engines smaller is not chemistry related; rather it is a mechanical limit. The fuel-air mixture is compressed by the piston, reducing the volume within the combustion chamber, and ignited at high pressures. As the size decreases, the other components also decrease including the cam shaft, crankshaft, and other moving parts. At these smaller sizes, the amount of power required to drive the moving components becomes greater relative to the total power produced, thus decreasing the mechanical energy

12

density of the system [14]. From a mechanical standpoint, Menon, et al. found that the minimum viable engine would occupy approximately 0.1 cm$^3$ corresponding to a 5 mm long crankshaft. Note this volume is total engine displacement and not cylinder volume for the working fluid.

Thermally, small engines have a number of issues. The most obvious is the increase in surface area of the combustion chamber relative to the chamber volume. This creates a number of heat transfer issues and leads to excess heat loss within the cylinder due to convection. The convective heat loss is due to the surface area of the smaller tubes contacting a larger percentage of the flow as compared to a larger engine. Further, the general guideline is that the cylinder walls must remain at or below a comparatively cool 450 K; therefore, the mean gas temperature within the cylinder is limited to about 850 K [11]. All of these comparatively low temperature requirements contribute in part to the acceptance of a substantial amount of incomplete combustion with only 40%-50% of the reactants undergoing the reaction [11]. A majority of this incomplete combustion is due to cylinder short circuiting. Short circuiting is fuel exiting the cylinder without undergoing the combustion process. This becomes a larger problem for the smaller engines. The combination of small combustion volumes and the need to keep the engines inexpensive drives this result. Some of these factors contributing to the lower cost designs include small engines utilizing carburetors rather than actively sensing and modulating fuel flow rate with $O_2$ sensors and computer controlled injectors. Another factor is these modified yardwork engines rely on cooling fins and utilize air cooling to make them lighter and smaller as opposed to their larger companions that use liquid cooling. The difference between air and liquid cooling capability further drives the acceptance of lower combustion temperatures to further decrease risk of overheating the engine and/or cylinder.

Before moving away from small engines, gas turbines and piston engines are

blended when turbochargers are introduced to the piston engines. Turbochargers utilize turbomachinery to boost the density of the air and therefore appear to increase the mass flow rate into the engine. As previously discussed, turbomachinery efficiency drops as mass flow decreases and at the small flow rates that tiny piston engines use, the turbocharger component efficiencies are fairly low with the compressor efficiency being lower. Compressor efficiency suffers more due to the adverse pressure gradient the air flow must fight across. Equation 2 mathematically shows how compressor efficiency is typically calculated where the $CI$ subscript means compressor in and the $CO$ subscript is the compressor out term.

$$\eta_c = \frac{\left(P_{t_{CO}}/P_{t_{CI}}\right)^{\frac{\gamma-1}{\gamma}} - 1}{T_{t_{CO}}/T_{t_{CI}} - 1} \tag{2}$$

There is a strong Air Force desire to improve the compressor efficiency for both turbochargers and small jet engines given their rising prevalence within the Air Force inventory and the savings it could generate annually in terms of fuel costs.

The key takeaway from this section is that gas turbine and IC piston engines have two different limitations when scaling to smaller flow rates and thus engine sizes. Gas turbines suffer from a rapid increase in viscous forces dominating within the turbomachinery while IC engines suffer from energy management and mechanical design issues limiting both efficiency and performance.

## 2.3  Wave Rotor Operation

A wave rotor is a rotating cylindrical drum with a number of passages evenly spaced along the outer radius as seen in Figure 2. Two air streams enter from the left through a static endwall via two ports with one being cold and at low pressure; the other is hot and at high pressure. Each stream exits separately through its own port on a static endwall to the right with an energy exchange occurring while traversing

14

the channel. This energy exchange boosts the pressure and temperature of the cold inlet stream by lowering the pressure and temperature of the hot stream. Wave rotors are most commonly found as pressure exchange devices utilizing oscillating pressure waves. By utilizing the reflecting pressure waves for energy exchange, flow can either be compressed or expanded and by timing the pressure wave reflections with openings occurring at either end, the flow can be sucked in or pushed out of the rotor. In Figure 2, the two entrance ports can be seen on the left at the 12 and 6 o'clock positions while only one exit port can be seen to the right at the 3 o'clock position. Note the arrow curving around the rotor indicates the direction of the rotation. Using Figure 2 as a guide, the fluidic action occurring within each channel can be briefly summarized in 5 steps.

1. The 3 o'clock port on the exit side opens generating an expansion fan back towards the inlet.

2. Fresh air enters the rotor at the 12 o'clock inlet port.

3. A hammer shock from the 3 o'clock exit ports closure begins the gas compression with the 6 o'clock inlet port's opening generating a second compressive shock propagating towards the exit wall.

4. Hot, pressurized gas enters through the newly opened 6 o'clock port exchanging energy in the form of heat and pressure with the fresh, unburnt air.

5. After the exchange, the unburnt air exits through the 9 o'clock exit port and the newly expanded air exits through the 3 o'clock port.

Fundamentally, wave rotors are described by the number of functional ports they have. They most commonly utilize two or four ports configurations although others do exist. Two-port wave rotors are typically used in constant volume, pressure gain combustion [16]. Four-port wave rotors are generally used for pressure exchange [17] [18] and are the focus of this investigation. Four port wave rotors utilize the hot,

15
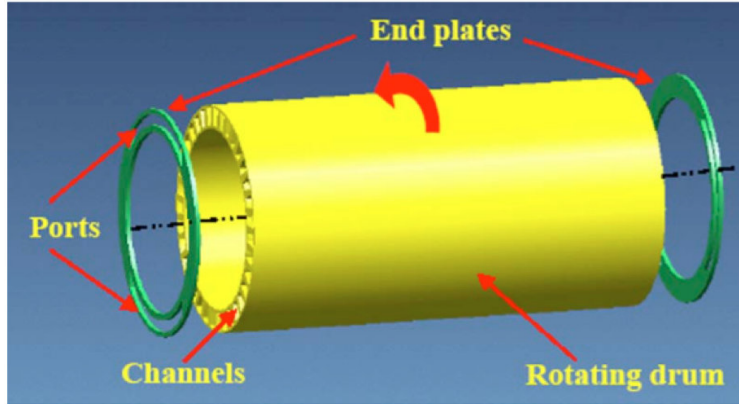
**Figure 2. Basic Wave Rotor Configuration [15]**

pressurized engine gases to boost the pressure of the new unburnt air. Note that a reverse flow four port wave rotor is another option and will be briefly discussed later. Figure 3 shows the general path the mass flow will follow for a throughflow wave rotor coupled to an external burner. The inlet air will enter on the left side of the figure. This gas is then compressed and exits the right side where it traverses to a burner that combusts the pressurized, preheated air. The wave rotor accomplishes this via the oscillating pressure (shock) and expansion waves. These waves traverse the enclosed channels aligned axially in the annulus of the rotor. From the combustion chamber, the exhaust gas reenters the rotor expanding in volume to compress the inlet charge of air before exiting the rotor for the final time.

Figure 4 is a wave diagram showing the primary pressure waves acting over the course of a wave rotor cycle. In wave diagrams such as Figure 4, solid lines are representative of compressive shocks while dashed lines are expansion waves. The cycle begins when the Turbine Outlet (TO) port opens generating an expansion fan that propagates back through the channel towards the inlet side. The Compressor Inlet (CI) port then opens as the expansion fan reaches the wall allowing inlet air to fill the channel. The closing of the TO port creates a hammer shock, which travels the length of the channel slightly compressing the air inside just as the CI port closes.

16
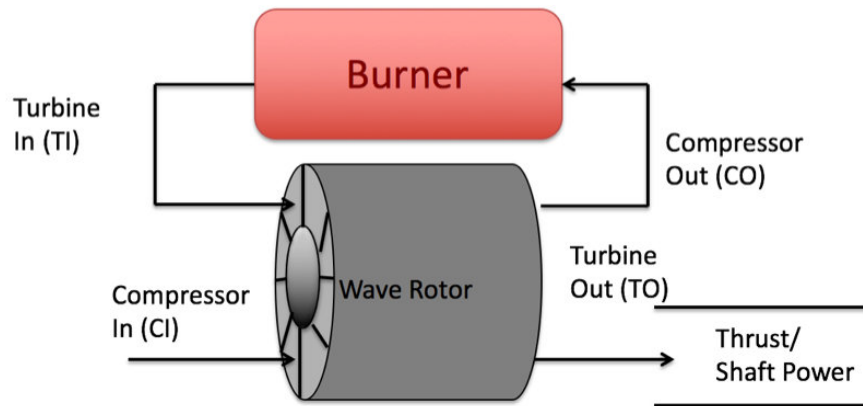
**Figure 3. Illustration of a Through-Flow Wave Rotor**

From the time the CI port closes to the time the Turbine Inlet (TI) port opens, leakage from the channels to the rotor housing occurs. The ports are arranged such that the time between these two events is minimized. The primary compression stems from the shock created from the TI port opening. The shock reaches the exiting side of the channel just as the Compressor Outlet (CO) port opens and reflects back towards the TI port further compressing the air and pushing it through the CO port. Note that there are also numbers on the ports; this is done in order to relate the wave diagram to the example x-t diagram, which will be discussed in depth, corresponding to Figure 5.

This pressurized air is routed to a combustor before re-entering the wave rotor through the TI port. When the TI port closes, it generates an expansion fan that moves along the channel reaching the outlet wall when the CO port is closing. Ideally, this causes the flow to momentarily stop and become essentially quiescent, however, the waves never fully disappear because the timing is never exactly perfect. The opening of the TO port creates a new strong expansion fan traveling towards the inlet side beginning the cycle again. Note that there may be a reflection(s) of either the shocks or expansion fans off of solid walls but paramount here is the correct wave

17
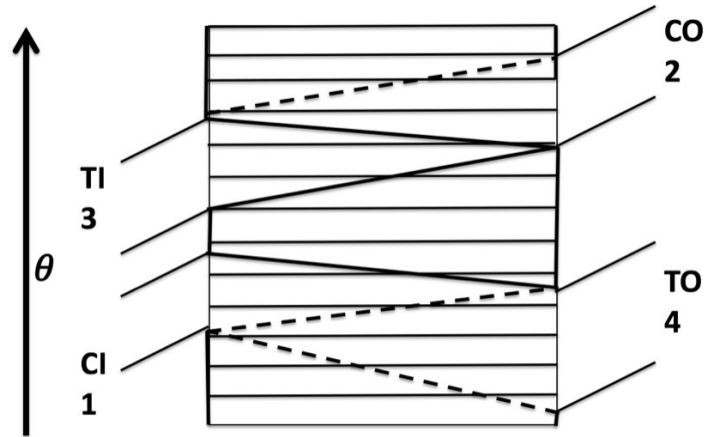
**Figure 4. Wave Diagram with Ports**

type coincides with the opening of the port. Note that wave diagrams such as Figure 4 only show the dominant waves.

Although not explicitly addressed yet, the rotating nature of the wave rotor implies that some sort of tangential velocity is imparted to the flow. This tangential velocity is addressed primarily with the angling of the inlet and outlet ports on the endwalls. They are angled such that the flow enters and exits the wave rotor relatively parallel to the tangential velocity implied within the cycle. Improperly angled ports will generate further pressure loss within the system. This pressure loss could be related to the flow impacting the rotor or endwall and requiring redirection, spurious pressure wave reflections of the endwall ports, or both.

Although wave diagrams are useful in order to explain how the oscillating pressure waves work, an x-t diagram such as the one shown in Figure 5 is more beneficial for describing the functional process. These diagrams represent a one-dimensional spatial axis (x) as it progresses in time, (t), on the y axis. Typically, x-t diagrams for wave rotors come in pairs with one showing pressure (left in Figure 5) and one showing temperature (right). These pressure and temperatures presented within the x-t diagrams are static properties for this research. Although not explicit in the

18

figures, x-t (and wave) diagrams represent an unrolled wave rotor such that the "top" and "bottom" are representative a single cycle. As can be seen, low pressure and temperature air surrounds Port 1 (CI), since this is representative of ambient air conditions. The highest pressure is around Port 2 (CO), as this is the air that that has been compressed within the wave rotor. The highest temperature exists around Port 3 (TI), since this air has just reentered the wave rotor from the heat source, the combustor. Lastly, the air being pushed out of Port 4 (TO) should have both an elevated temperature and pressure relative to Port 1 since this port's conditions represent how much work or power can be removed from the exhaust.
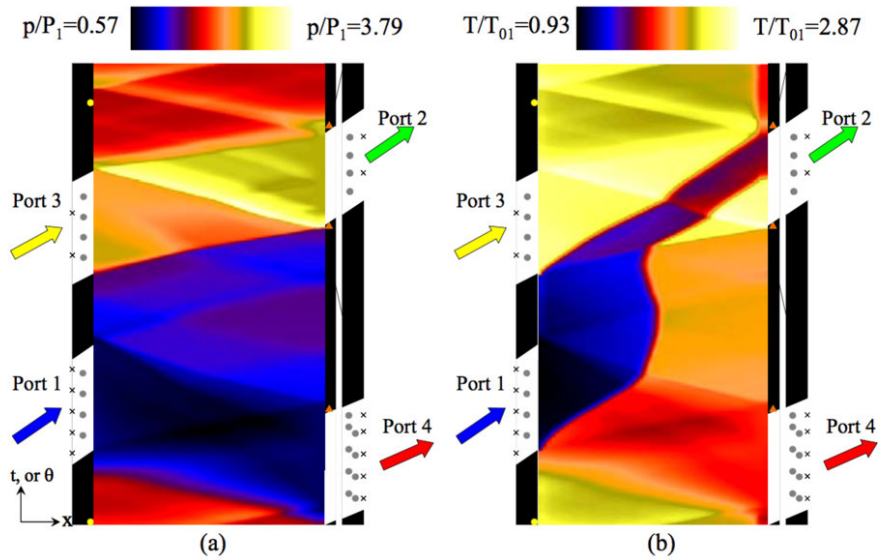


**Figure 5. Sample x-t diagram from Wilson, et al. [17]**

Wave rotor operation is characterized by the size and rotation of the rotor along with wave speed; the port location correlates to the time it takes for the wave to propagate the length of the channel and arrive at the correct port as it is opening. Operating a throughflow wave rotor off-design is similar to throttling a gas turbine engine. A throughflow wave rotor's off-design operation is affected by changing both the rotor speed as well as the fuel flow rate into the combustor. Altering both such

that the wave speed maintains correlation to the rotor rotational speed in effect creates a throttle line. Wave speed is directly proportional to the local sonic velocity as sonic velocity is a function of temperature. The temperature is directly related to the fuel flow into the combustor.

Generally, two distinct types of four port pressure exchange wave rotors have been studied. The first is the throughflow type that has been discussed exclusively to this point. The other type is the reverse flow type characteristic of pressure wave superchargers (PWS). It is important to note that to this point, all wave rotors built and studied at the Air Force Institute of Technology (AFIT) have been reverse flow, PWS designs such that the cooler, unburnt air enters and exits on one side while the hot engine exhaust enters and exits on the other side in order to boost manifold air pressure to an IC engine [4][19][20]. Figure 6 compares a reverse flow wave diagram (left) used by previous investigators such as Mataczynski to a throughflow wave diagram (right) used in this investigation to illustrate the differences in the cycles, especially the port locations.
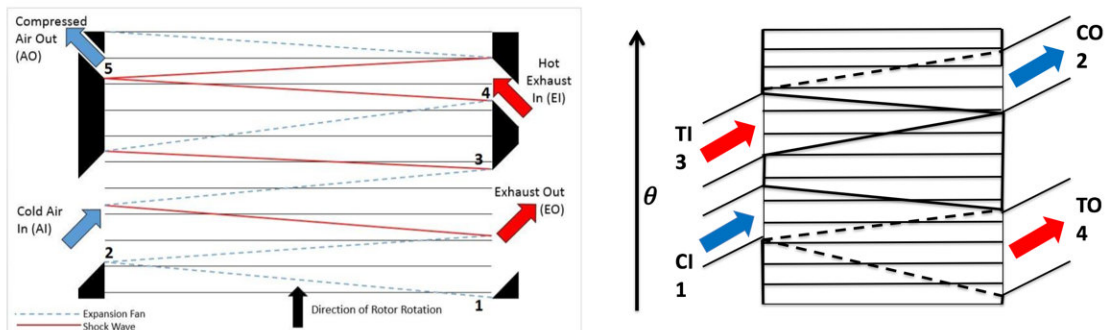


**Figure 6. Comparison of Wave Diagrams, Reverse Flow [21] (left), Through Flow (right)**

The emphasis of this figure is to illustrate the reverse flow having a hot and cold side whereas the throughflow has an inlet and outlet side. This also shows how the general angles of the ports is dependent on the cycle as the reverse flow has two

20

ports angled left and two right while the throughflow has all four angled in the same direction.

Section 2.2 concluded with a brief discussion on compressor efficiency. In theory, wave rotors have higher compression efficiency at the low flow rates and thus could fit the niche that the small turbochargers and jet engines struggle in. The difficulty though is in calculating what the compression efficiency for a wave rotor. Equation 2 does not easily fit with wave rotors for calculations for a variety of reasons primarily relating to the mass flow such as the presence of EGR. Equation 2 assumes a constant mass flow rate through the device with no change in chemical composition. The presence of EGR violates both of these assumptions. One of the ongoing efforts of wave rotor research is to quantify the compression efficiency, but at this stage, a good method does not exist. Given that issue, this research will only look to quantify the total efficiency as described in Section 2.1.

## 2.4  History of Wave Rotors

Pressure exchange devices were first patented in 1906 when Knauff [22] invented a static pressure exchange device. The first of his two patents that year was a cylindrical drum that had a pressure exchange via a method not involving pressure waves. Knauff intended the drum to have curved rotor blades and canted inlet vanes in order to extract shaft power. The second of his two designs simplified this original idea to a simple pressure exchange device, similar to what today has become known as a wave rotor. Five years later, Burghard [23] patented the first dynamic pressure exchanger utilizing pressure waves. His idea would later be implemented by Lebre's patent in 1928 [24] for what would become known as Lebre's machine.

It was not until the 1940's that the understanding of fluid mechanics advanced enough for the next step in application. The Brown Boveri Company (BBC), later

21

Asea Brown Boveri (ABB), accomplished this when they successfully designed a topping stage for a locomotive gas turbine (2200 hp or 1640 kW) [15]. The theory gave them good performance expectations, however, the manufacturing and implementation of the device left much to be desired, and thus, it performed poorly. ABB did succeed in 1956 with a wave rotor used as a topping cycle for diesel powered tractors. This wave rotor was a PWS.

Starting in 1955, this work was done in conjunction with ITE Circuit Breaker Company in the U.S. and the Swiss Federal Institute of Technology (ETH Zurich). Supercharging diesel automobile engines came from ITE in the mid 1950s; ABB provided the knowledge and ETH did the manufacturing [15]. The first successful prototype test was in 1971 on an Opel 2.1 diesel engine. The primary advantages were the light weight and rapid response time as compared to conventional superchargers and turbochargers. Mainstream usage did not occur until 1987 when the Comprex® was placed in a gasoline fueled (Otto cycle) Mazda 626 Capella. More than 150,000 Capellas with a PWS have been produced since 1987 [15]. Other successful vehicle tests of the Comprex® included those on Mercedes-Benz and Ferrari [21]. Though called a pressure wave supercharger, a PWS utilizes the exhaust gas to compress the fresh air more similarly to a turbocharger; however, it also shares traits with typical superchargers in that they sometimes run off of the crankshaft.

In addition to functioning within Diesel and Otto cycles, wave rotors have been studied as a part of the Brayton cycle for decades. Specifically, relevant work to this investigation began at the NASA John H. Glenn Research Center (GRC) in 1988. Wave rotors were studied as a topping cycle to be used between the high-pressure turbomachinery spool and the combustor in the Brayton cycle [17][18]. NASA GRC conducted multiple tests on their four-port rig, which shares many similarities with this study. In the NASA four-port study, cryogenic, low-pressure air entered the wave

22

rotor and underwent the compression half of the cycle. This outflow was measured for temperature, pressure and mass flow then dumped. A separate, high-pressure air supply was pumped through an electric heater and elevated to a temperature corresponding to the desired temperature ratio and then fed back into the wave rotor to undergo the expansion half of the cycle. It is important to note that although the cycle was open loop, operations always entailed matching the flow exiting the heater to the mass flow rate dumped overboard such that the cycle was effectively closed loop. The NASA studies examined the potential work in terms of temperature and pressure ratios rather than power or torque output as this study does. The NASA studies also used much higher flow rates with the smallest flow rate on the order of 0.41 kg/s [17]. This work served to validate the Q1D CFD code NASA developed to assist in the design of wave rotor cycles in Section 2.5. It will be discussed more in depth later [3][17][18].

Parallel to their use as a pressure exchange device, wave rotors have also been examined for constant volume pressure gain combustion applications. For these applications a premixed fuel-air mixture was injected into the passages and combusted with ignition via recirculated hot gases. This concept has been investigated by Indiana University-Purdue University at Indianapolis (IUPUI) [25][26] and Allison/Rolls-Royce LibertyWorks [16]. These two organizations have been working closely together for more than a decade and built a proof of concept rig in 2009 [26][27]. Though operation was extremely short, it proved that a wave rotor could function as a pressure gain combustor. The short, three second operation was not cycle limited; rather the data collection equipment could only withstand the violent operating environment for a few seconds [27]. Although a pressure gain cycle was initially considered for this research, it was eventually ruled out due to the high risk and significant difficulty of scaling the combustion time scales to low mass flow rates as the combustion time

23

scales are unrelated to physical size.

Michigan State University (MSU) has examined ultra-micro wave rotors as well as other wave rotor applications. MSU's published work relating to wave rotor never included any experimental results and their computational work was similar to that of Nalim's at IUPUI. The experimental ultra-micro wave rotor work implied a machining problem for the small intricate passages [28]. Today, these machining issues are mitigated through metal 3-D printing techniques; however, despite the improvements to these technologies, no publications regarding wave rotors have come out of MSU since the mid 2000's. Some work regarding wave disk engines was published in the latter part of the decade though that deviates significantly from wave rotors.

At AFIT and the Air Force Research Labs (AFRL), Smith [20] began the process of validating the Q1D NASA code (further discussed in Section 2.5) at low mass flows for use in turbo-normalization of a small IC engine. This work involved extensive investigation of the Comprex®, shown in Figure 7, in which they began the validation of the Q1D code for use at the smaller dimensions as compared to the NASA rigs. This validation was necessary because the Comprex® OD was 9.4 cm [20] compared to the NASA four-port rig's OD of 20.3 cm [18], and the Comprex's® mass flows on the order 5.9 kg/min of air flow while the NASA rig was on the order of 18 kg/min [17]. Smith demonstrated the code's ability to replicate the physics at the smaller scale and showed a maximum deviation of 7.55% [29]. Following the work of Smith, Mataczynski [21] furthered the Comprex® study by reaching typical engine operating temperatures.

Smith also began the design of a smaller PWS; however, this initial design only utilized one cycle per revolution [29]. This design was completed by Mataczynski [21], who added a second cycle per revolution in order to increase the efficiency. When designing the PWS hardware, many of the design features of the Comprex were used

24
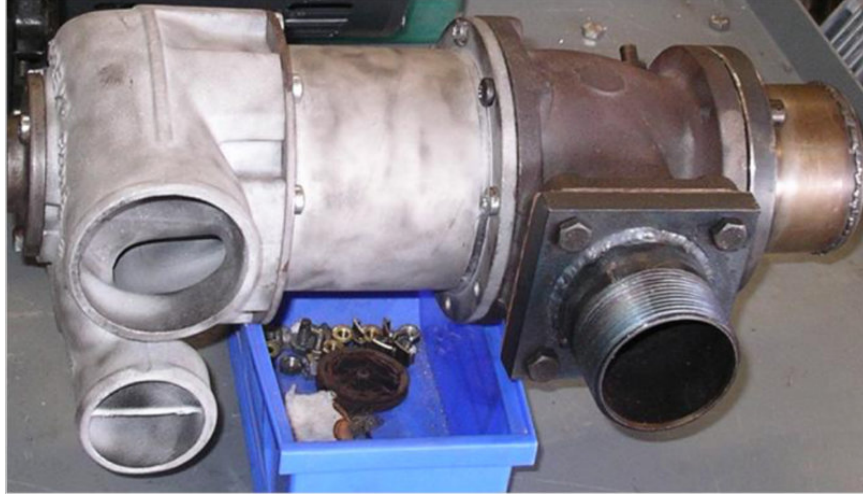
**Figure 7. Assembled Comprex® PWS [29]**

such as a cantilevered support. Subsequent testing revealed various insights on how to improve the design on future wave rotors to be further discussed. This smaller PWS (OD of 4.1 cm) was designed to interface with a 95cc Brison IC engine operating at sea level conditions. This size engine is typical of the smaller UAVs with altitude issues such that the pressure boost provided by a wave rotor could solve. Mataczynski's work was motivated by the effort to boost manifold air pressure (MAP) going into the piston of the IC engine in an effort to simulate sea level conditions at altitude. Figure 8 is an exploded view picture of the scaled PWS wave rotor designed by Mataczynski [21]. This work also confirmed the code's accuracy for extremely low, on-design mass flow rates (approximately 1.2 kg/min ) [19]. Although tests showed differences in off design cases, both computational and experimental data showed the same trends. Note this rotor was driven by an external electric motor not shown in the figure.

www.manaraa.com
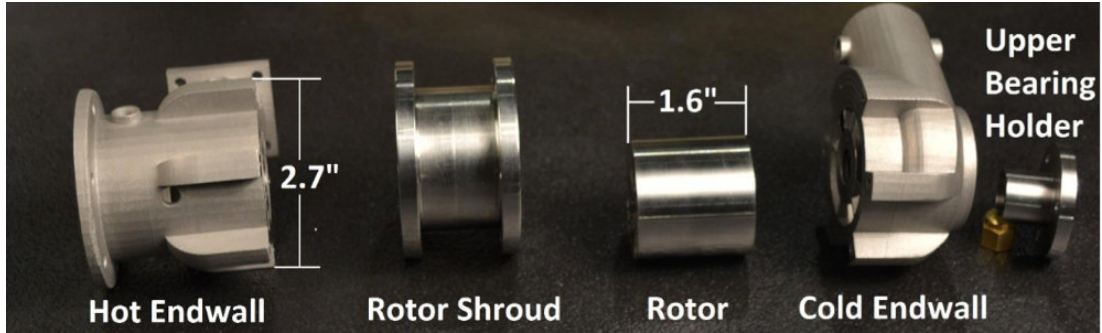
**Figure 8. Scaled PWS Exploded View [21]**

## 2.5   Design Code

Beginning in the early 1990s, Dan Paxson at NASA GRC began the development of a Q1D code in order to simulate wave rotor operation. This code, a 2nd Order Lax-Wendroff scheme based on the method of Roe, utilizes a high-resolution finite volume scheme. It is a quasi-one dimensional model of a single wave rotor passage traversing between the ports on each side [1]. Although the model does not account for the effects of multiple passages (amongst many other initial simplifications), over the span of a couple years Paxson refined the code. He added modeling for more of the governing physics making the code more computationally intensive and accurate. By 1995, the code was able to accurately quantify the wave rotor's governing physics and the loss parameters. [2][3]. Note that computationally intensive in 1995 easily runs on modern laptops in seconds to minutes.

Though initially treating the boundary conditions at the ports as instantaneous changes between open and closed, a temporal aspect was quickly added in order to simulate the dynamic effects of opening and closing the ports [2]. This rate directly correlated to the rotational speed as well as the port's arc length. In addition to adding the time dependent boundary conditions, a leakage model was also added [3]. This modeling is necessitated by the minute axial clearance necessary for physical

26

operation, as the rotor cannot spin freely if impacting a stationary end wall. This leakage modeling also includes accounting for the discharge coefficient of the tube. The first round of improvements also included a viscosity term [2] through a Reynolds number in order to account for both momentum and viscous forces.

The code itself is entirely non-dimensional and tracks mass fluxes and ratios of various properties as a function of the inlet port. These various properties are the temperature, pressure, density, and velocity within the channel. In its present state, the code's primary input is a temperature ratio which drives the cycle. The code itself consists of three distinct modules that are used iteratively. The first module is a basic ideal cycle design using the temperature ratio. The second adds a variety of real effects and is used to generate the non-dimensional rotor. Finally, the last module adds in the various loss mechanisms in order to fully model the real physics seen during experimental operation.

Once fully converged, the code will yield a completely modeled wave rotor cycle with the port locations and the various inlet/outlet conditions as non-dimensional values. The process also utilizes a non-dimensional size and rotor speed which, when coupled to the Reynolds number term, essentially forces the user to determine the real size of the rotor. This process will be further discussed in Section 3.1. Note that the code only allows for a straight rotor channel with arced bottom and top walls.

The verification and validation of this code, including a mesh refinement study, initially occurred during NASA's wave rotor experiments in the mid 1990s [3][18]. A heat transfer model was added to the code during the experimental testing. Originally the code was written with an uncoupled burner loop for a throughflow wave rotor. The section of the code accounting for heat transfer also includes the potential to tie the CO and TI port mass flows together. The mid-90s work also discusses that the range of wave rotor operation this code was originally intended to supplement

27

was between 0.23 kg/s and 2.27 kg/s. The Rolls-Royce Allison Model 250 engine the NASA experiment was tested to augment has a nominal flow rate of about 1.36 kg/s [18].

The initial comparison between computational and experimental testing showed the same trends and yielded similar values for temperature, pressure, etc. However, the actual values differed due to differences in measurement locations. Therefore, the team hesitated to make a definite conclusion about the code. NASA tackled these challenges and in 2007 published a paper discussing the improvements to the experimental rig as well as definitively showing the codes accuracy. The improvements to the experimental set up included more instrumentation closer to the rotor exits in order to match the measurement locations to the code as much as physically possible. The physical design was also modified to include a moveable end wall that better accounted for rotor expansion as well as improving the sealing between the rotor and end wall. This improved sealing enabled greater prevention of the mixing between the high and low pressure loops. Wilson, et al. presents an in-depth discussion of these experimental modifications as well as showing the improved matching between computational and experimental values [17].

Recently, the code has been modified to work with pressure wave supercharger wave rotors such as the Comprex® which required further verification and validation as this wave rotor had a reduced mass flow of 5.94 kg/min, (0.099 kg/s). Mataczynski, et al. [19] verified the modified codes accuracy to within 5.6% for all conditions except CO pressure. CO pressure accuracy was around 17%; however, this can be attributed to pipe flow losses due to measuring pressure far downstream of the end wall.

Mataczynski also built a scaled PWS and validated the code results against it while operating at less than 1.36 kg/min [19]. The code performed very well at on-design conditions. During off-design operation, the code demonstrated the same

28

trends as experimental results but the exact values differed with the code actually underestimating performance. Much of the codes loss of accuracy at off-design conditions was due to the experimental wave rotors containing endwall pockets to dampen undesirable waves, which the code lacks. In order to model a PWS, Paxson modified the code in order to simulate a reverse flow wave rotor. While these modifications did not change the physics within the code, they did change the flow path within it. The CI and CO ports were then located on the left side of the code (assuming left to right flow for the overall cycle) and the high pressure ports were both located on the right side. In depth details on using the code can be found in Appendix B.

## 2.6  Heat Addition

One of the primary components of any engine cycle is heat addition. Wave rotors can either be integrated into an existing engine as a pressure exchange device such as turbine topping (NASA) or turbo-normalization (AFIT) or they can stand alone as an engine when coupled to some sort of heat addition. This heat addition could come in two different manners: combustion within the tube (IUPUI/Rolls-Royce) or coupled to a separate burner.

The path pursued for this research aimed to integrate a combustor with a wave rotor. Two primary choices were investigated for the burner. A turbulent diffusion flame jet was considered; however, the flame length was significantly longer than the rest of the hardware's combined flow path. A can-type combustor, the second option, was chosen for the low pressure drop and relative simplicity given the low mass flow required for this project.

Can-type combustors have been used in aircraft for decades and are still prevalent in many jet engines today. Their primary usage has been within engines requiring a high turbine inlet temperature, $T_{41}$, on a mass flow basis [30]. The main benefit to the

29

can-type combustor is the short length of the combustion chamber when compared to something utilizing a conventional diffusion flame such as a Bunsen burner. This is due to a strong recirculation zone generated by a few key features of modern can-type combustors. Modern is a relative term as the basic design has changed little in the last 50 years [31].

A can-type combustor, as shown in Figure 9, has a fuel injection system that is in or around a radial swirler (swirl vanes in Figure 9) bringing 15-20% of the total air-flow into the chamber. This swirling air forms a recirculation zone just downstream of the injector head. This recirculation (primary) zone is strengthened by the primary jets (or secondary air holes) approximately one chamber diameter downstream of the injector face. The jets, not only leaning out the rich recirculation zone, enhance the turbulence inside it while also helping to move the mixture downstream. These features only account for 60%-75% of the air flow that will exit the combustor. The balance of the air comes from cooling the liner. Goebel et al. [32] examined removing the dilution holes in order to increase airflow percentages through the swirler and primary jets. This had the unexpected effect of decreasing efficiency because the dilution holes were then shown to be the primary contributor to the smoothing of the combustor exit profile called the pattern factor. Pattern factor, as defined in Equation 3, is essentially the temperature distribution at the combustor exit.

$$PF = \frac{T_{exitmax} - T_{exitavg}}{T_{exitavg} - T_{inletavg}} \tag{3}$$

A low pattern factor is indicative of a uniform exit temperature. A high pattern factor would indicate hot spots that would likely cause minor thermodynamic issues in the short term and significant structural issues over the lifetime. These temperature gradients would likely result in a shortened useful life span for the combustor and any downstream components, typically the turbine. All of the combustion should

30

occur within the flame tube as this has the cooling necessary to withstand the peak combustion temperatures.
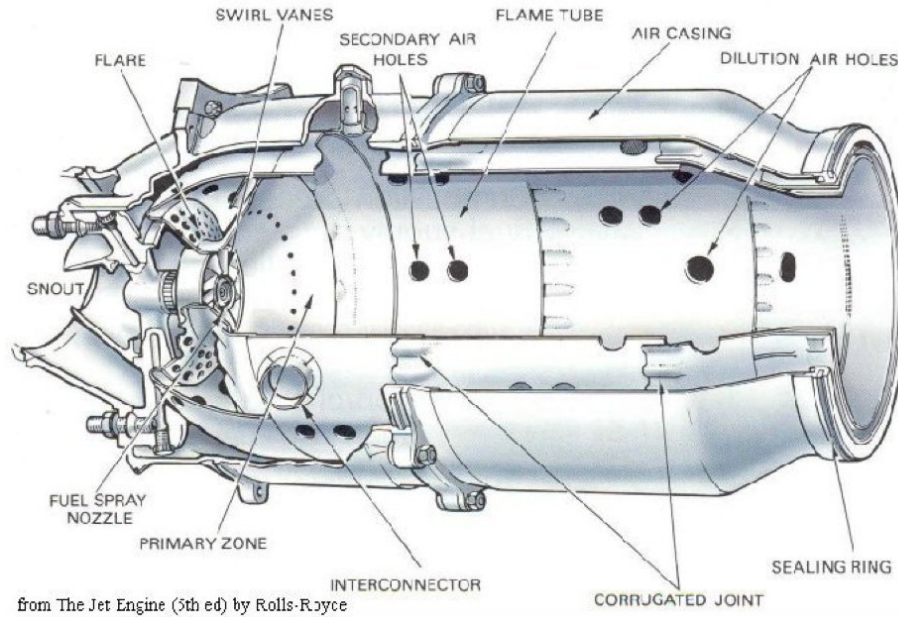


**Figure 9. Conventional Can-Type Combustor [33]**

Figure 9 has a couple of terms requiring further explanation. The flare (or heat shield) is a cooling feature that creates a physical barrier preventing the recirculation zone from impacting the upstream part of the case and utilizes the air injection holes upstream of it for cooling and positive axial momentum to the recirculating air mass. The corrugated joint serves as an air injection point, however, it introduces air in the axial direction to form a thin film of cooler air along the liner to protect the surface from the flames. Cool here is relative to the combusting mixture in the center. The interconnector serves to connect multiple cans together for engines using a can-annular burner. These are in larger jet engines and will not be discussed further. The snout and sealing ring serve to connect the burner to the other components of the engine. The dilution holes serve to dilute the equivalence ratio and stabilize the exit wake in order to acheive the desired exit temperature and profile [31].

31

Can-type combustors have efficiencies greater than 90%. Typically, combustor efficiency is defined using burner emissions. By analyzing the emissions for carbon monoxide content and residual hydrocarbons in parts per million, the completeness of the combustion can be quantified by Equation 4, where $H_c$ is the heat of combustion for the given fuel, $EI_{CO}$ is the emissions index of Carbon Dioxide and $EI_{C_xH_y}$ is the emissions index of the unburned hydrocarbons. The emissions index provides a quantification of the molecules present within the exhaust gas from the system.

$$\eta_b = \left[ 1 - 10109\frac{EI_{CO}}{H_c} - \frac{EI_{C_xH_y}}{100} \right] * 100 \tag{4}$$

One of the biggest influences on combustion efficiency is the turbulence within the mixing zone, as turbulence shortens flame length and improves air and fuel molecular distribution [34]. A homogenous mixture will have enhanced combustion versus a stratified one. Because the swirl vanes, center left in Figure 9, introduce swirl to the incoming airflow, they have the greatest effect on the upstream mixing turbulence; however, for a given design, increasing the inlet temperature and pressure will also increase the combustion efficiency [31]. This is due to the increase in molecular reaction rate of the fuel and air with elevated temperature and pressure. Note that while the swirl vanes are generating the turbulence, the secondary air holes, seen in Figure 9, create a recirculation zone which serves to stabilize the flame during the combustion process.

Faster reactions lead to more complete reactions within a given space and thus a decrease in unburned hydrocarbons. This also causes comparatively greater concentrations of carbon dioxide and lower carbon monoxide concentrations as pressure and, especially, temperature directly correlate to the molecular reaction rate of the fuel and air. These concentrations are an important factor in determining the completeness of the combustion process. Numerous studies on combustion efficiency and its

32

quantification exist including those by Bicen et al.[31], Diehl et al.[30], and Weigand et al. [35][36].

## 2.7  Foil-Air Bearings

One of the significant mechanical challenges associated with the operation of any small rotor is the bearing design. Bearing design for a wave rotor is made more difficult given the high temperature operating environment. A cursory glance through ball bearing specification sheets will show that most are limited to operating conditions below 500 K. The temperature limits of conventional bearings led to the usage of a foil air bearing. A foil air bearing is a static bearing utilizing high pressure gas as a lubricant. The most basic design of a foil air bearing consists of three thin sheets of foil, typically a nickel superalloy. [37][38]

Foil bearings operate through the use of hydrodynamic forces that essentially allow a shaft or rotor to sit cushioned on a thick boundary layer of air. This boundary layer is generated by the viscous effects between the spinning rotor and the leaves of the bearing. Because there is minimal contact between the rotating and stationary parts, friction is minimized [39]. This lack of friction allows for higher rotational speeds on the order of 250,000 RPM according to manufacturers [40], however most manufacturers do not list a top speed because it greatly varies from bearing to bearing depending on size. Instead they refer to a DN number which is the bore diameter in millimeters multiplied by RPM. The lack of friction also means that extra heat does not build up such that the only temperature consideration is the existing environmental temperature. This allows for an operating temperature approaching the lowest metal operational temperature of the various components within the operating environment. In many cases, this is going to approach 1500 K as the superalloys typically begin to leave their loaded operational range around this temperature.

In foil bearing designs the outer most foil (labeled bearing sleeve in Figure 10) is on the inner surface of the shroud while the innermost foil sits on the exterior of the rotor (which is confusingly named the top foil as it sits on the shaft). The corrugated middle foil, called the bump foil, is connected to the bearing sleeve. The name comes from the bumps on it shown in Figure 10. The bump foil allows for substantial misalignment as compared to typical rigid journal and thrust bearings. The top foil (see Figure 10) and bump foil generate Coulomb damping which improves dynamic rigidity and stability during operation.
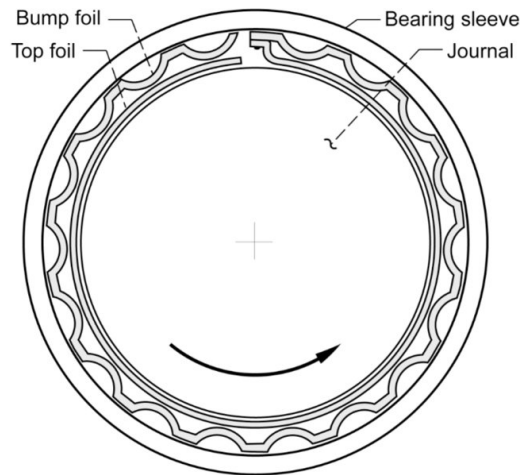


**Figure 10. Example Foil Air Bearing [37]**

Rotor rotation generates a pressurized fluid that pushes the top foil out radially and allows the rotor to "float" within the sleeve. At low rotational speeds, significant friction will cause wear over time and also necessitates a high start-up torque [37]. Foil air bearings have been in use for decades and are found in a variety of different platforms including many 4th generation Air Force aircraft [38]. They become preferable for a number of reasons although two stand out. The first is the previously mentioned operating range. Their operational temperature range spans all the way from cryogenics to combustion temperature environments, far greater than metal or

www.manaraa.com

ceramic bearings. In addition to their temperature range, they typically have a minimum rotational speed, and as the speed increases, the dynamic stabilizing forces of the bearing increase. In addition to the significant environmental advantages, their lack of lubrication requirements improves reliability while lowering operating costs. Their primary downside, however, is the comparative difficulty in manufacturing as well as shelf price. Price becomes a tradeoff between the upfront shelf cost and the life time operating costs.

# III. Experimental Setup

With the overarching goal of this project being the development of a wave rotor functioning as the key component of a kilowatt class Brayton-cycle engine, a number of intermediate steps were required before achieving an operational system. The first of these steps was the computational design utilizing the Q1D NASA code. With the computational 2D design in hand, the laboratory hardware could be designed. As part of the component design, it was realized that a suitable commercial of the shelf (COTS) combustor was unavailable, sparking the need for a custom design. As the design approached completion, manufacturing began as well as the identification and acquisition of the support parts such as the foil air bearing, the venturis, and the necessary measurement devices, i.e. Kiel probes, pressure transducers, and thermocouples.

The components required individual checkout before the system could be fully integrated. The first series of tests was characterizing the combustor. This consisted of startup and examining performance at various inlet pressure and temperature levels of the air flow. Occurring concurrently with the combustor testing was the flow calibration of the venturis and spinning the rotor. Rotordynamic analyses and stress calculations on the rotor were also performed to ensure survivability within the operating regime for key components. With the wave rotor accessories tested, the components were fully assembled for testing. This chapter details the various set ups necessary to achieve these tests as well as how to quantify their results in relation to the overall goal.

## 3.1 Computational Setup

The cycle design began by first learning to use the Q1D NASA code. After familiarization with the code, work on the cycle could begin by iterating between the code and dimensional calculations. The code inputs and outputs were all non-dimensionalized, therefore calculations were created to relate the dimensional values to the code. Prior to using the code, a target exit pressure and temperature as well as a system mass flow had to be estimated for a given power output. While the mass flow can be estimated mathematically from the definition of power given a specific kinetic energy, exit temperature and pressure had to sensibly estimated. The estimated temperature and pressure are used to calculate the specific kinetic energy, and the associated mass flow rate falls out. Remembering the discussion from Section 2.1, this series of equations is later used to calculate the thermal efficiency of the wave rotor cycle. Unstated within this are the assumptions of net power generation for a static (no free stream velocity) case.

Because this research is a modified Brayton cycle, using the exit conditions of a comparably sized jet engine would put the user in the right range for temperature and pressure values. For this research the starting estimates were a mass flow of 1.3 kg/min, a temperature of 867 K, and a pressure of 137 kPa. These conditions would produce 1.56 kW of power.

The first series of equations were used to establish approximate target values for the wave rotor exit conditions based on a priori conditions. These conditions were an exit temperature ratio of three accompanied by a 30% increase in pressure when compared to ambient as well as a rotor diameter (40-50 mm) and power output. These values target a kilowatt class engine acting as a test bench for a future Class 2 UAV. The final a priori condition was the max rotor diameter: 1.65" (41.9 mm), the OD of Mataczynski, et al.'s rotor [21]. This condition was not directly used to

37

determine the power calculation, but used in a later step to determine the size and to dimensionalize the initially non-dimensional rotor.

A few iterations between the power calculation and the mass flow rate enabled work to proceed to the Q1D code. Equations 5-10 utilized the various a priori conditions to estimate the mass flow. Equation 5 is the exit Mach number, $M$, calculated by expanding the total exit pressure to ambient. Mach number is used to determine the static exit temperature, $T_s$, in Equation 6, a necessary value to determine the exit sonic velocity, $a$, in Equation 7. The Mach number and sonic velocity were used to determine the exit velocity, 8, which was used to determine the specific kinetic energy, $ke$, within the exit flow. The specific kinetic energy multiplied by the mass flow rate determine the power. Since the power was a previously estimated target, this equation was used to determine an initial mass flow estimate. Then, during design iterations, it was used to calculate the cycle's power since the code output is dimensionalized to a mass flow.

$$M = \sqrt{\frac{2}{\gamma - 1}\left(\frac{P_{TO}}{P_{CI}}^{\frac{\gamma-1}{\gamma}} - 1\right)} \tag{5}$$

$$T_s = \frac{T_{TO}}{1 + \frac{\gamma-1}{2}M^2} \tag{6}$$

$$a = \sqrt{\gamma R T_s} \tag{7}$$

$$v = Ma \tag{8}$$

$$ke = \frac{v^2}{2} \tag{9}$$

38

$$P = \dot{m}ke \tag{10}$$

Although not listed as a priori conditions, the ratio of specific heats ($\gamma$) is relatively constant during stable operation. A $\gamma$ of 1.31 was used. This value is based on an estimate of the gas conditions exiting the wave rotor. The next couple of sections are a walk through of the code operation as used in this investigation, but is not the only means to use this code. Note that this $\gamma$ is the ratio of specific heats for the exit conditions. All of the steps found here and in Appendix B should be considered a general guideline and not a hard rule.

### 3.1.1 WRITR Q1D Module.

The Q1D code was a series of three interrelated codes that began with the previously mentioned a priori values and ended with a completed cycle design. The first of these codes, WRITR, was a two step code that used most of the a priori conditions to determine the port timing as well as the approximate pressure and temperature conditions at each port. Although WRITR had thirteen separate inputs for the code, only six were parameters of interest in this study, the others were for use in previous NASA work. The six parameters of interest were the expansion ratio (EXPRAT), ratio of specific heats (GAM), non-dimensional opening time (THETOT), cycle temperature ratio (T4T1), the spacing between CI and TI (IDLAND), and how much of the cycle was analyzed (UPCYC). The parentheticals are the input names for the code listed in Figure 11.

The expansion ratio, EXPRAT, represented the expansion of the gas between the TI and TO ports. This value drove the energy exchange within the wave rotor. An expansion ratio of 1.0 would equilibrate TI and TO pressures; however, this is not desired and, therefore, was iteratively decreased to the minimum converging value

39

```
EXPRAT=    0.30000
   GAM=    1.34800          RATIO OF SPECIFIC HEATS
    DX=    0.02000          SPACIAL STEP
   DTI=    0.01000          TIME STEP
THETOT=    0.57400          NON-DIMENSIONAL OPENING TIME
  FSSC=    0.29800          FRICTION FACTOR
  PNTS=         51          # OF INTERIOR CELLS PLUS ONE
   PRI=    1.00000          INLET SHOCK PRESSURE RATIO
   NCT=    1.00000          EXHAUST CLOSING TIME 1.0:U=0.0 0.0:U=U_UNIFORM
  T4T1=    3.10000          EXHAUST TEMP / INLET TEMP
 BLEED=    1.00000          COOLING BLEED- INLET FLOW / EXHAUST FLOW
 UPCYC=          1          1=FULL CYCLE 0=ONLY BOTTOM
IDLAND=    1.00000          # OF O.T.'S BETWEEN INLET CLOSE AND DELIVERY OPEN
```

**Figure 11. WRITR Module Inputs**

such that the TO pressure would be as high as possible. $\gamma$ was estimated through a weighted average of the combustion products and the fresh flow within the rotor. A weighted average was used due to throughflow wave rotors having a larger mass flow in the burner loop. Fresh air had a $\gamma$ of 1.4 and hydrocarbon combustion products were estimated to be 1.31; the 1.348 value was the result using a weight of 1.35 for the combustion products and 1.00 for the reactants due to the recirculation favoring the products. The non-dimensional opening time, THETOT, was how long the CI port was open and was the reference scale to determine the port timing for all four ports. The opening length could either be a time or a distance depending on what step of code usage the user is at: at this stage, this was a time. It became a length in the next module when other parameters were engaged. The spacing parameter, IDLAND, was the number of THETOTs between CI and TI. For this study the minimum value, 1.0, was used. The minimum is 1.0 based on how the code was written, not a calculation.

The cycle's temperature ratio, T4T1, was the a priori condition calculated previously to produce the power. The code nomenclature uses port numbers but this term is identical to $\frac{T_{TO}}{T_{CI}}$. The last important term, UPCYC, was a time saving feature that enabled examining the whole cycle versus half of the cycle. It allowed quick computations of the inlet and outlet conditions to see if basic convergence was possible

40

and what the outlet conditions were by not computing the burner loop values (CO and TI). This feature was used to determine the approximate expansion ratio and opening time for a useful cycle. These two values were further iterated along with minute changes in the temperature ratio when designing the full cycle.

Figure 11 is the final design values used for this study. Most of the work with this aspect of the code was minor tweaks to the six variables mentioned above. The tweaks were the result of completing the WRITR aspect and adding in non-dimensional sizing within the next module, WR. Based on WR's preliminary results, slight modifications to EXPRAT, T4T1, and THETOT were made to guide the wave rotor to the approximate desired power output. More details on this process will follow. It is important to keep in mind that the series of three code modules follow the general usage order of WRITR, WR, then SIMBC; however, the cycle design results in multiple loops. A user may use WRITR and WR in a loop four or five times before moving on to SIMBC where adding in the loss models promptly results in a bad cycle requiring a new start from WRITR.

WRITR's output was the non-dimensional, ideal cycle for a wave rotor with the specified temperature ratio. It determined the pressure and temperature ratios at each port as well as the size and location of the four ports, but was entirely detached from rotor size. It could be used to design a wave rotor with a 2.0 mm rotor or a 2.0 m rotor. In addition to the desired port conditions, the output file also included the majority of the remaining design variables necessary to design a converged, non-dimensional cycle corresponding to a specific rotor size. This output file only required minor modification to become the input file for the next module, WR.

The other input terms were not varied in this study. They were either for building the computational mesh (PNTS, DX, and DTI) or for examining the physics within the code (PRI and NCT). FSSC, the friction factor, was set to a constant value of

0.298 based on previous NASA work. A published citation for this does not exist but the value used was given by the code's designer, Dr. Dan Paxson [41].

### 3.1.2  WR Q1D Module.

With the no loss, non-dimensional cycle output from WRITR, the dimensional relations within WR began. The first step of this process was to change the references from WRITR's output. WRITR used the conditions present with the rotor channel immediately prior to CI's opening as the reference while the other modules, WR and SIMBC, use the CI conditions as the reference. This re-referencing made CI pressure and temperature outputs 1.0 as opposed to 0.36 and 0.27 respectively which WRITR computed them to be. This process makes the non-dimensional values intuitive to look at as their value becomes $n$ times reference (atmospheric) pressure or temperature. While they would deviate away from 1.0, it was never more than a few thousandths ($\pm 0.003$). After the re-referencing, relations (DONL, HONL, RADIUS, and WALONL) between the physical size of the rotor were input to the code as WRITR was entirely cycle based with no correlation to any sort of non-dimensional size. Many of these terms are defined in Appendix A. These values related the rotor diameter and channel height to the rotor length. The final a priori condition, Mataczynski's PWS rotor diameter (41.9 mm), was used here. It is important to keep in mind that although non-dimensional sizes were introduced within WR, they did not yet correspond to a single absolute value; that would not happen until the RESTAR term was added. The rotor speed and number of channels were also established here as they directly relate to the rotor sizing. The number of channels was a simple calculation based on the computed THETOT term such that $2\pi$ divided by THETOT is the number of channels. This calculation is rounded to the nearest whole number as partial channels are not feasible. The rotor values are listed below in Table 1.

**Table 1. Final Rotor Design Values**

| Length | 63.5 mm | Diameter | 41.9 mm |
|---|---|---|---|
| Channel Height | 6.35 mm | No. of Cells | 29 |
| Rotor Speed | 38,500 RPM | Wall Thickness | 1.27 mm |

Although it may appear to the reader that the decision process for these terms is somewhat arbitrary, in fact, this is the iterative part of the design loop where the code user will input various sizes into the WR input file. Iteratively modeling the different size combinations and their effects on the exit pressure and temperature ratios allowed the user to converge on the best values, effectively sizing the rotor with respect to itself. Best values means resembling the ideal cycle's port ratios computed by WRITR. It was also at this point that the design moved from a non-dimensional time for the port "locations" to radially locating them on non-dimensional endwalls. A succeeding step properly sized the ports to fit on a 0 to $\pi$ radians arc length necessary for a two cycle per revolution design.

Although more realistic than WRITR's output, this stage of the design was still an ideal case and required the implementation of various real world effects began. The first of these real effects was RESTAR, a Reynolds number based on CI's sonic velocity, defined by Equation 11.

$$RE = \frac{\rho a_{CI} L}{\mu} \tag{11}$$

This uses the average density ($\rho$), sonic velocity ($a$), and kinematic viscosity ($\mu$) as determined by the static reference conditions of 289 K, 101.33 kPa, and a gas constant of 286.9 J/kg-K. The Reynolds number term also fully sizes the term by relating the length unit (i.e. m, cm, mm) to other parameters.

With the initial non-dimensional rotor sizing done, the length, speed, rotor radius, and channel height were iterated, to balance the mass fluxes, MF, as shown in Figure

www.manaraa.com

12. Balanced is used loosely as WR does not force this condition; balancing here was getting ports 2 and 5 within a few thousandths of each other while simultaneously getting ports 1 and 4 similarly close. WR has different port numbers than shown previously in Chapter 2's x-t diagrams as the left endwall uses 1-3 and the right 4-6. For this work, CI=1, CO=5, TI=2, and TO=4. This numbering is due to the code's application to other wave rotor types as well. It was quickly revealed that the length and speed caused the greatest amount of change and, although the radius and channel height did affect the mass flux balancing, only significant deviations to these parameters caused any sort of change. These significant deviations generally had detrimental effects to the cycle's overall pressure and temperature ratios. This led to focusing on the length and speed of the rotor as well as cycling back to the very beginning with WRITR and starting over with tweaks to T4T1 and EXPRAT.

Generally, a shorter length rotor requires a higher rotational speed and vice versa. The only rules of thumb concerning the rotor length and the speed were to maintain the rotor length to diameter ratio on the order of 1 whereas the speed was desired to be in the vicinity of previous AFIT wave rotor work, i.e. $35,000 \pm 10,000$ RPM.

|   | MF | EF | MO | UB | PB | TB | P0 | T0 | ALPH |
|---|------|------|------|------|------|------|------|------|--------|
| 1 | 0.502 | 0.498 | 0.934 | 0.564 | 0.803 | 0.944 | 1.001 | 1.000 | -0.007 |
|   |      |      |      | 0.524 | 0.802 | 0.944 |      |      |        |
| 2 | 0.735 | 2.818 | 3.019 | 0.868 | 3.053 | 3.713 | 3.493 | 3.844 | -0.006 |
|   |      |      |      | 0.843 | 3.052 | 3.713 |      |      |        |
| 3 | 0.000 | 0.000 | 0.000 | 0.000 | 0.000 | 0.000 | 0.000 | 0.000 | 0.000 |
|   |      |      |      | 0.000 | 0.000 | 0.000 |      |      |        |
| 4 | 0.492 | 1.501 | 1.479 | 1.128 | 0.967 | 2.837 | 1.293 | 3.059 | -0.003 |
|   |      |      |      | 1.109 | 0.966 | 2.837 |      |      |        |
| 5 | 0.745 | 1.815 | 2.558 | 0.659 | 3.492 | 2.370 | 3.944 | 2.446 | -0.008 |
|   |      |      |      | 0.626 | 3.490 | 2.370 |      |      |        |
| 6 | 0.000 | 0.000 | 0.000 | 0.000 | 0.000 | 0.000 | 0.000 | 0.000 | 0.000 |
|   |      |      |      | 0.000 | 0.000 | 0.000 |      |      |        |

**Figure 12. Sample WR Output**

The iteration also included minor adjustments of the port incidence angles, non-dimensionalized as ALPH, to help minimize pressure losses. An ALPH of zero implies

the ports are aligned properly to the rotor channel with minimal losses whereas non-zero values indicate losses due to improper port-channel alignment. This is the most time consuming part of the design process as "rules" on how the parameters will affect the output do not exist. Once the mass fluxes are "balanced", the next module was used to force the complete balancing of the mass fluxes as well as add in the other loss terms within the SIMBC module. After completing the SIMBC steps, WR was run a final time as it also outputs a file used to generate the x-t diagrams.

### 3.1.3  SIMBC Q1D Module.

SIMBC, the final module, added the various loss mechanisms to the code as well as an external heater model that forced a coupling between the CO and TI ports. SIMBC could be used to design a wave rotor utilizing an electric heater or a fuel powered combustor as the heat source. The type of burner modeled was implied by the user's selection of $\gamma$ as an electric heater powered wave rotor would use 1.4 whereas a combusting heat source would have something less than 1.4 such as this work's 1.348. The most important parameter of this module was QCORR as seen in Figure 13. This was a non-dimensional heat addition term that raised the temperature between CO and TI. Given the number of sub-equations, this parameter will not be further defined mathematically. The completed design point used a QCORR of 4.0. This QCORR does not directly correlate to a specific fuel flow rate; instead, a better comparison would be a non-dimensional enthalpy term based on the change in CO and TI temperature ratios. Calculation of the fuel flow rate based on the enthalpy gain and fuel choice is discussed in Section 3.3.1.

The various loss mechanisms had to be added piecewise or the code could not converge given the deviation from its previous solution. Therefore, the leakage modeling was added in first. This was done in a two step process with the first step

45

being placing a gap between the rotor and endwalls. This gap, normalized by the channel height, was designed to be 0.127 mm similar to Mataczynski[21]. With the non-dimensional gaps, PGAP and WGAP in the code, the discharge coefficient, CD, of 0.8 was added. This discharge coefficient was given by Paxson as the typical wave rotor value [41].

With leakage fully enabled, the various parameters relating to the burner had to be iterated upon in order to return the outputs to the necessary temperature conditions while maintaining as much exit pressure as possible. Note that the losses primarily show up as pressure drops as increasing QCORR overcame any temperature drops. The completed design point used a QCORR of 4.0. At this point, the final loss mechanism, heat transfer was added. This was done by including a Prandtl number of 0.7. By adding a non-zero Prandtl number, the energy equation was effectively turned on and allowed thermal energy to convect to the rotor walls requiring more heat added to the flow between CO and TI. Again, the heater parameters, primarily QCORR, had to be iterated upon to restore the necessary cycle temperature ratio. A side effect of SIMBC coupling CO and TI was that it forced the MFs of CO and TI to be equal which indirectly caused CI and TO to be essentially equal. The SIMBC output is shown in Figure 13. The enforced port balancing as well as the changes to the pressure and temperature ratios can be seen when compared to Figure 12.

The outputs from SIMBC were used to determine the mass flow rates between the various ports as well as their temperature and pressure conditions. While the temperatures and pressures were simply multiplication of the appropriate value by the reference condition, the mass flow calculation was more complicated and is given as Equation 12. Definitions for port areas and *MFCORR* are given in Appendix

$$\dot{m} = \frac{2(MFCORR)(A_{CI})(P_{CI})(A_{web})}{\sqrt{R(A_{CI})}} \tag{12}$$

46

```
              P0        T0
     1    1.00000   1.00000
     4    0.87976   3.06394
     2    3.35930   4.27350
     5    3.39141   4.27350
   CAV    1.87910   2.98571
 MFFRAC    1.33138
 WDOTIN   -0.00292
 EPSILON    0.33799
 KLOSS    1.24854
 QCORR    4.00000

          MFCORR    P4/P1     T4/T1     OMEGA
          0.49946   1.31464   3.06394   0.76572

      MF      EF      MO      UB      PB      TB      P0      T0     ALPH
  1  0.485   0.481   0.924   0.545   0.814   0.948   1.000   1.000  -0.000
                             0.501   0.814   0.948
  2  0.646   2.754   2.895   0.871   2.987   4.140   3.374   4.272   0.000
                             0.844   2.987   4.140
  4  0.485   1.483   1.488   1.077   1.009   2.862   1.315   3.064   0.000
                             1.056   1.010   2.862
  5  0.646   1.752   2.440   0.658   3.400   2.645   3.791   2.721  -0.000
                             0.622   3.400   2.645
```

**Figure 13. SIMBC Module Outputs**

R is the gas constant and $A_{web}$ is the web area between the rotor channels. The mass flow is doubled as each revolution contained two complete cycles. Note that the Port 4 conditions are the exit conditions and corresponds to 133 kPa and 885 K while the mass flow was calculated to be 1.59 kg/min. These values were those used in Equations 5-10 in order to calculate the available system power.

### 3.1.4 Visualization.

Although SIMBC's output was used to determine the power available and to design the experimental hardware, the flow visualization was done using WR. WR, while incapable of calculating the losses, remained operable with their inclusion as they simply appeared as pressure and temperature gradients. WR created a separate output file which was read into a MATLAB script written by Dr.Paxson. This script created the x-t diagrams previously discussed in Section 2.5 and shown in Figure 14.
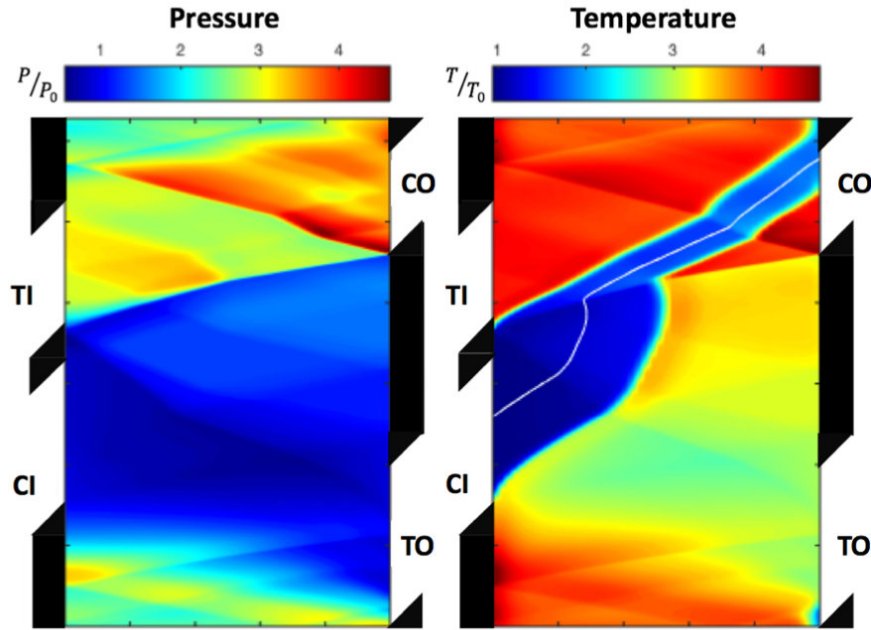
**Figure 14. x-t Diagram**

The x-t diagrams come in pairs with one depicting static pressure (left) and the other static temperature (right). They have a couple of important features. Their most important feature shows the gradients that occur within the rotor as it is spinning. The diagrams have the cycle beginning at the bottom and moving forward in time, or spinning as these are the same, in the y-direction while the x-direction is the flow moving from the inlet wall (left) to the exit wall (right). In both diagrams, the pressure waves can be seen reflecting back and forth within the channel as well as their effect on the flow. This effect of the pressure waves on the flow is especially clear on the temperature diagram as the white line is a streamline. The numerous inflection points along the streamline are the pressure waves causing instantaneous changes to the flow. Also shown primarily on the temperature diagram is both the exhaust gas recirculation, (EGR), by the abundance of hot gas exiting through CO as well as the small amount of unburnt air that does not go through the burner loop and simply exits through TO at only a moderately higher pressure and temperature. Al-

48

though designing a cycle without the unburnt air missing the burner loop is possible, the time and effort to do so are not worth anticipated gain. This expected efficiency gain is far from a guarantee and a "perfect" cycle with no bypassing air may be worse than a cycle with some bypassing air [41].

### 3.1.5 Off-Design.

In addition to modeling the design point, off-design operation of the rotor was examined in order to make a more complete comparison to a comparable gas turbine engine. This was done by modulating both the rotor speed as well as the heat addition within the burner. Because a wave rotor functions as a coupled compressor and turbine, an operational line was created by changing the rotor speed and heat addition terms within the Q1D code. Initially, this was done by increasing or decreasing the rotor speed by 5% and iterating upon the heat addition term until a fairly linear relationship appeared. This process was repeated to fully characterize the throttle line. Two relationships were pursued, a direct correlation between rotor speed and heat addition such that both went up or down together or through an inverse correlation such that if rotor speed went up, heat addition went down. Both of these methods have some physical basis as wave rotor functionality is based on the port timing. There are two methods to deal with the port timing, increase the rotor speed to match the increased sonic velocity present due to higher temperature (direct method) or decrease the rotor speed such that the number of reflections is increased by integer multiples. The inverse method was quickly discarded as the results were extremely unfavorable. A $\pm$ 30% design RPM range was examined for both methods. The lower limit was defined for both by a lack of convergence whereas the upper limit came from the burner temperature becoming too high for realistic operation. The results of this analysis will be presented within Section 4.2.2.

49

## 3.2 Wave Rotor Design

With a target wave rotor cycle from the Q1D code, the individual components were conceived. The hardware design was primarily done with CAD software. The initial designs were done using Solidworks 2013 while some of the final components were completed in Siemens NX 9.0. This section will address the design of the rotor and the endwalls as well as the air bearing, the containment shroud, and the motor mount.

### 3.2.1 Rotor Design.

The Q1D code defined a majority of the dimensions and other aspects of the rotor. The rotor's length, number of channels and the radial dimensions of the channels were all obtained from the code and were listed previously in Table 1. This yielded a rotor with straight channel side walls and thin inner and outer radial walls. At this point, the rotor was given realistic inner and outer walls capable of withstanding the rotational forces the rotor would undergo during operation. The exterior surface was given additional thickness to allow for balancing resulting in an inner wall thickness of 1.45 mm and an outer wall thickness of 2.54 mm. The decision was made to make the rotor diameter slightly larger rather than change the flow area. The rotor also lacked an attachment point for a shaft. Previous work from Mataczynski et al. [19], showed difficulty in utilizing a press fit shaft and led to the decision to have an integrated shaft. Additionally, rather than using a cantilevered rotor as previous research had done [4][19][20], a rotor supported at both ends was chosen to mitigate potential vibrational mode issues. A rotordynamics analysis of the built rotor is included in Section 4.4.1.

Though mitigating potential mechanical difficulties was done first, potential thermal issues were equally important. The Q1D code estimates a rotor cavity tempera-

50

ture around 850 K. This operating environment required a few physical modifications in order to increase the chances for success. The first change, though less visually obvious in Figure 15, was not using a single shaft through the entire rotor. Instead, two concentric shafts were used. This was due to the likelihood of uneven heating within the rotor channels and the cavity within the rotor. If a single shaft were used and uneven heating occurred, it may have led to unnecessary thermal stresses in the axial direction. Similar thermal stresses also drove the other alteration, curving the walls dividing the rotor channels. The walls were curved in the direction of the rotation (Clockwise when examining Figure 15) rather than opposing the incoming flow to prevent any unexpected wall effects. Additionally, the channel corners were all chamfered to decrease any stress concentrations from the multiple potential sources. The wall shape did not correspond to any particular curve and was deemed good by the positive results of the finite element analysis (FEA).
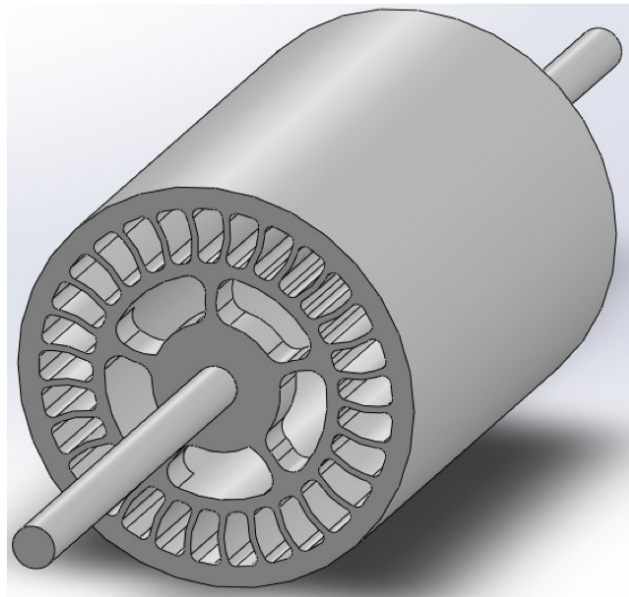


**Figure 15. Isometric View of Design Rotor within CAD**

51

A final aspect of the rotor design was a finite element analysis to analyze the structural and thermal loading. The FEA was done by Emily Henry of AFRL/RQTI. The results showed the rotor would survive with a factor of safety of 5.4. The maximum stress and strain occurred on the walls dividing the rotor channels. The maximum stress was found to be 171.4 MPa while the strain was 1.03 mm/m. The maximum displacement occurred on the ends between the arms to the shaft and was 0.00876 mm. The design point conditions were used for the FEA study. Figure 16 shows the stress analysis as this was the primary concern.
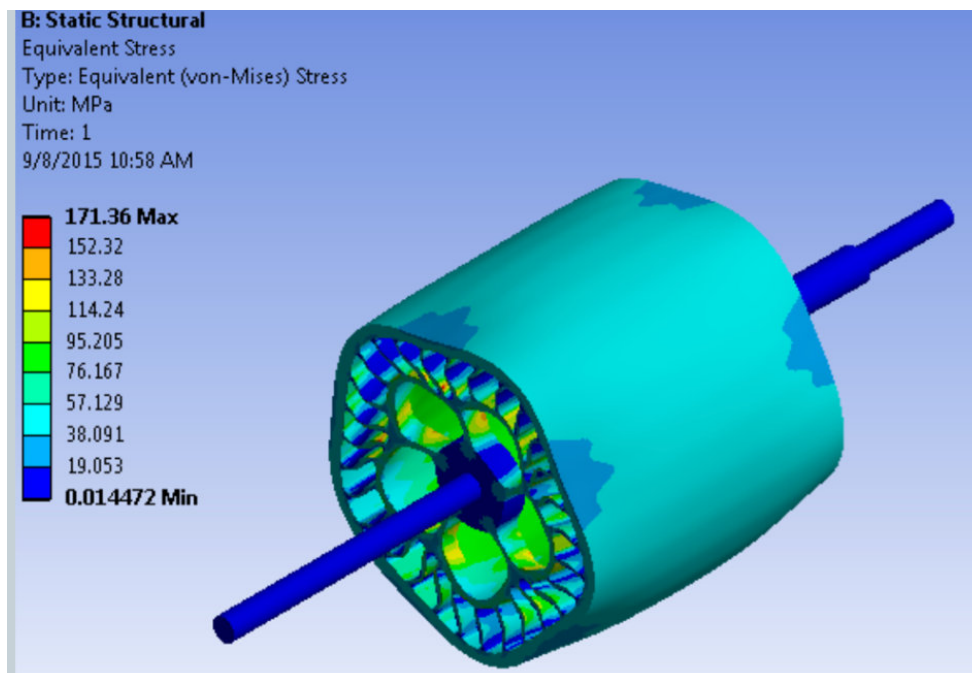


**Figure 16. Rotor Stress FEA**

The other study of interest was a rotordynamic analysis; however, this was unable to be accomplished as the double shaft with a gap design required a more advanced setup then ANSYS, the simulation software used for the analyses, could handle. Due to time and budgetary constraints, the rotordynamics were discussed with an expert, Dan Gillaugh of AFRL/RQTI, and the results were that the bearing arrangement should push the vibrational modes above the operating point but that there were

52

too many factors to model in a simple system, i.e. bearings, shaft seals, and motor. When it was asked if modeling the rotor with a solid shaft through the center was possible, the rotordynamicysts said that would change the modes too much to be of use; therefore a ping test was accomplished after the components were manufactured and will be discussed later in Section 4.4.1.

The final aspect of the rotor design was the shaft length. Shaft length was determined after the end walls were designed. They were long enough such that each end protruded from the end walls by about 6 mm. The total rotor length, though designed to be 63.5 mm, had to be estimated for the hot conditions. Given the designed operating environment as well as radial loading during operation, the rotor was chosen to be produced from Inconel. From here, the thermal coefficient of expansion for Inconel was used to determine the approximate growth. This was found to be up to 0.8 mm or 1.26% of the rotor length. An analysis to determine the growth direction showed the overall growth would be split near 50/50 between growth towards the inlet wall and growth towards the outlet wall. To complete the design, both the cold length and the maximum estimated hot length had to be known. 0.13 mm were also added to each side in order to accommodate the endwall gaps. The inlet wall shaft and exit wall shaft were designed to be the same length, 57.2 mm long. The step on the shaft for the bearing arrangement, further discussed in Section 3.2.3, was the final 19.1 mm.

### 3.2.2 Endwalls.

After the rotor was designed, the endwalls were next. Similar to many of the rotor parameters coming from the code, the primary design aspects of the endwalls, the port locations, were known from the code output and are listed in Table 2. The code calculated the cycle on a 0 to $\pi$ radians basis. This wave rotor was intended to be

two cycles per revolution and therefore, rather than each end wall having two ports, they had four. Based on this, the inlet wall has two CI ports and two TI ports offset by 180°. The exit wall had the same type of configuration.

Table 2. Radial Port Locations

| Port | Open/Close Cycle 1 | Open/Close Cycle 2 |
|------|--------------------|--------------------|
| CI   | 0.75/1.61          | 3.89/4.75          |
| TI   | 1.83/2.64          | 4.97/5.78          |
| CO   | 2.30/2.92          | 5.44/6.06          |
| TO   | 0.00/0.99          | 3.14/4.13          |

These locations, along with a center hole for the shaft, formed the two dimensional plate that had to be extruded three dimensionally. The CAD model also included dead pockets. This was an oversight as previous AFIT designs had used them. They were used by a PWS wave rotor [21][29] to assist in off-design operation. Throughflow wave rotors, such as the one discussed here, do not need the pockets as both speed and TI temperature is modulated to create a pseudo-design point during off-design operation. Although the dead pockets are included in the CAD modeling, their mitigation is discussed in Section 3.8.1.

The end walls were extruded, the shaft hole was "cut," and the ports were located on the surface but not yet cut. The routing of the ports was the most difficult part of the CAD work as the various ports had to be maneuvered around each other as well as the shaft hole. For illustration purposes, a simple end wall is shown in Figure 17. Both ports labeled T had to exit through T on the right and both C's had to exit through the far left C. Though not easily seen in any of the CAD images shown in Figures 18 and 19, the side cylinders contained a horizontal separation to split (or combine) the flow towards (or from) either the upper or lower cycle.

The side cylinders were designed to connect to the venturis and combustor plumbing. Square flanges were included as part of the design to serve as solid attachment

54
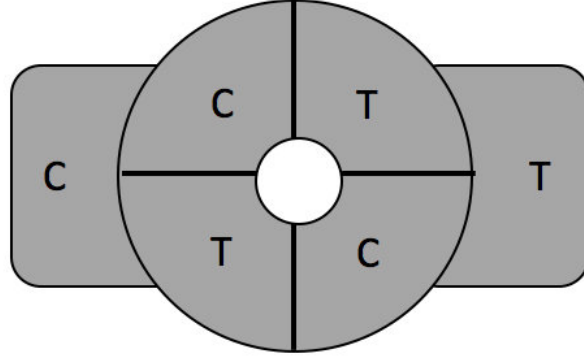
**Figure 17. Illustration of Port Locations to Inflow/Outflow**

points. The flanges can be seen in the figures below. Other features that can be seen in the CAD models include the bolt holes to maintain the shroud connecting the two end walls together and containing the rotor and the dead pockets previously discussed.

Although a little difficult to see in the top set of images, the bottom image displaying the top down view of each endwall shows a ridge located on the active face of the end walls. These ridges were concentric to the shaft hole and acted as a centering piece for the shroud. They were added to aid in the alignment of the shroud containing the rotor and the air bearing. Since the rotor was primarily supported by the air bearing and the air bearing was a locational fit into the shroud, the shroud had to be aligned perfectly with the end walls. The ridges were cut into the endwalls and a lip was placed onto the shroud such that a loose interference fit exists between them to concentrically "lock" their locations into place with the bolts. Originally, the bolt holes were designed for 6-32 screws; however, during the growing process to be discussed later, they came in slightly oversized. Because of this, they had to be redone as 8-32 screw holes. This will be further discussed in Section 3.8.2.
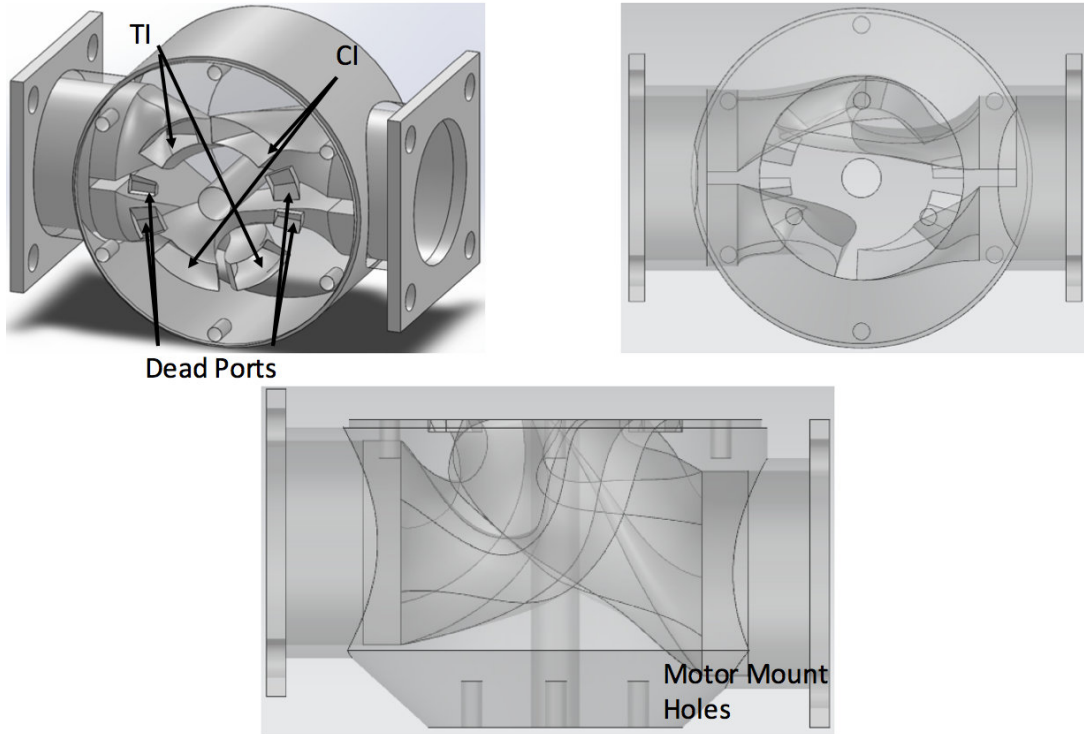
**Figure 18. Transparent Inlet Wall (top left-isometric, top right-front, bottom-top view)**

A final feature existed in the exit wall that was not added to the inlet wall. On the back side of the exit wall as shown in Figure 19, a bearing cavity was located in order to provide the axial loading necessary to prevent the rotor from impacting the endwalls due to any longitudinal motion. A brief examination of the pressure differential between the inlet and outlet ends of the channel demonstrated on average 22.1 kPa pushing towards the outlet. Two unshielded SKF 619/5-2Z deep groove ball bearings were fit into the cavity and separated by a small spacer to counteract this force and maintain the axial position. Although one of the primary concerns with these conventional bearings was excessive heating via conduction through the shaft and end walls, small air holes were placed in the design to route pressurized cooling air to the shaft just before the bearing cavity. This cooling air, depicted in Figure 20, would then be able to convectively cool both the end wall surrounding the bearings
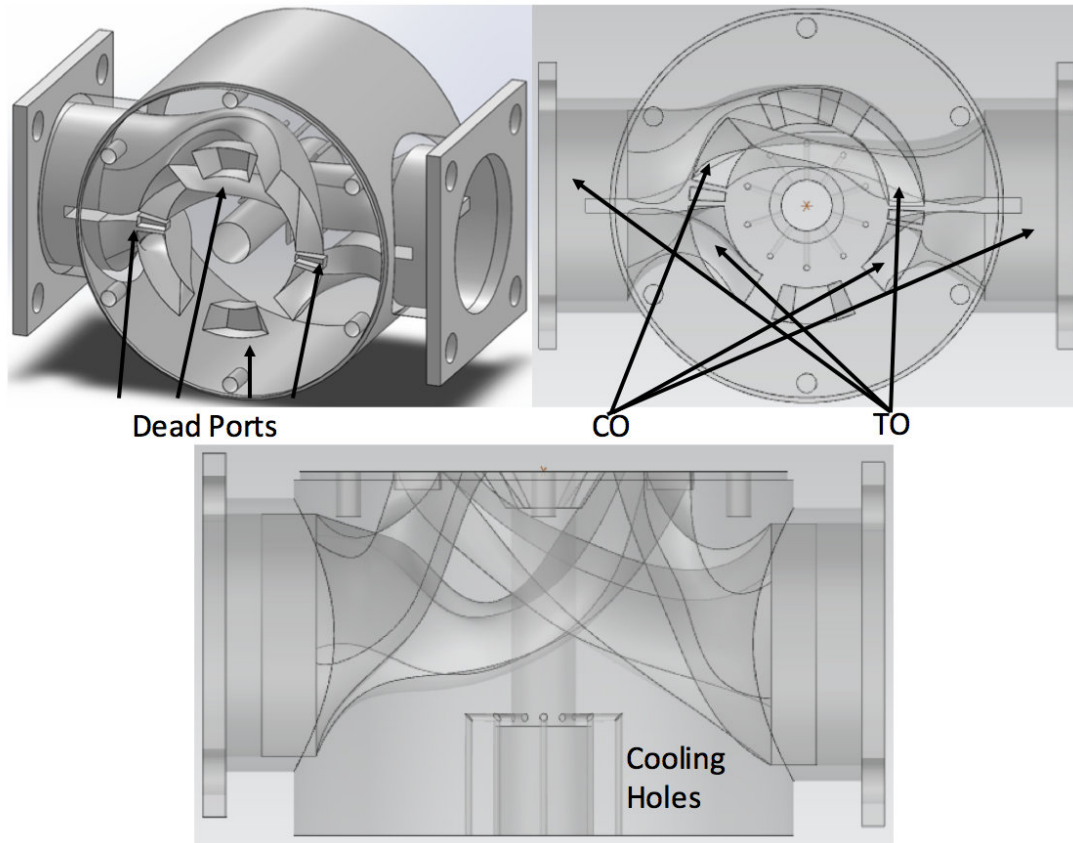
**Figure 19.  Transparent Exit Wall (top left-isometric, top right-front, bottom-top view)**

as well as the shaft just prior to the bearings. The inlet wall also contained a distinct feature. It included a three-hole pattern opposite the active face to accommodate the motor mount. This will be further discussed in Section 3.2.5.

Given the design complexity and the one-off nature of the components, casting or machining the rotor and the end walls was either too expensive or near impossible. Therefore, these parts were grown using Direct Metal Laser Sintering (DMLS). After the growing process, the outer surfaces were machined to a smooth surface. To do this, most of the parts were grown slightly oversized and ground down to the specification. In order for the rotor to maintain its strength while operating at extreme temperatures, the available DMLS material choices to make this were either Inconel or Cobalt-Chrome. Inconel 718 was available for DMLS and used for the manufacturing
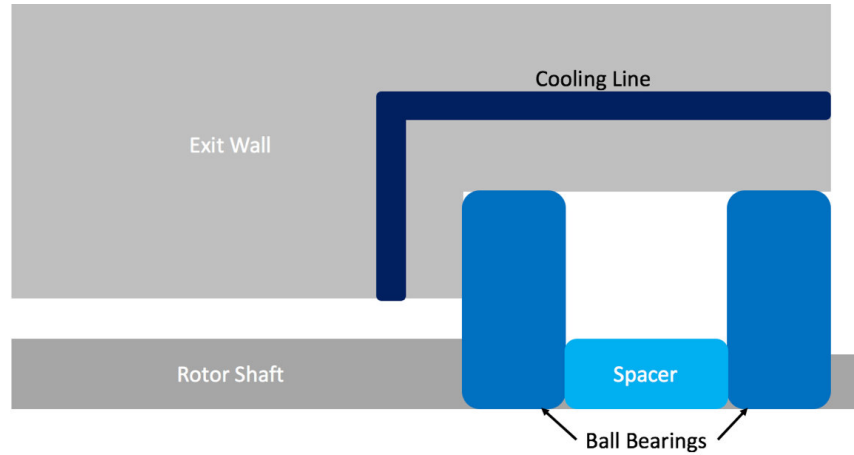
**Figure 20. Convective Cooling of Aft Bearings**

as Cobalt-Chrome was far more expensive and not necessary. In order to produce all of the components in a single batch, everything (two rotors, the endwalls, and the combustor swirler) was made of the Inconel 718. Although other materials i.e. stainless steel and titanium, are available for DMLS, they did not have the required strength at elevated temperatures to survive the rotor's stress loading.

### 3.2.3 Air Bearing.

Because of the harsh operating environment and the cooling difficulty on the inlet wall, an air bearing was used to radially support the wave rotor. Air bearings are all custom to the customer's design specifications. After contacting Dr.Daejong Kim of the University of Texas and Bellkim Energy LLC., the design process for an air bearing to fit the wave rotor began. He and his group required the rotation speed, the operating temperature, available cooling, and a CAD model of the rotor that included the polar moments of inertia and mass in addition to the dimensions. With this information, they determined a bearing 50 mm long with an inner diameter of 48.4 mm and an outer diameter of 54 mm would best fit this project's needs. Within the inner diameter, there were three leaves that utilize hydrodynamic forces to generate

the boundary layer that cushioned the wave rotor and provided the "stiffness" keeping the rotor centered radially.

Bearing stiffness is essentially how much force the bearing is capable of exerting in order to prevent radial displacement. Typically, air bearings have a much lower stiffness compared to conventional bearings. For example, this air bearing has a stiffness of 2-4 MN/m whereas the deep groove ball bearings at the aft end of the shaft have a stiffness around 22 MN/m. Air bearings have a stiffness range because their stiffness is dependent on the rotational speed of the inner object and the amount of hydrodynamic force the bearing generates at that speed. The faster the rotor spins, the more "rigid" and "stiff" the boundary layer becomes. A finished air bearing is pictured in Figure 21.
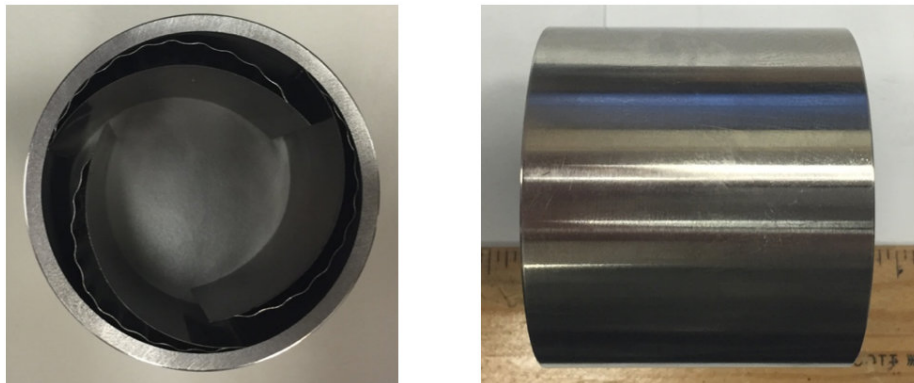


**Figure 21. Top-down and Side Views of the Air Bearing (Before Operation)**

This bearing only prevented radial motion and the rotor was free to move axially, thus necessitating the aft bearing formation. Because it only acted radially, the air bearing had to be concentric to the rotor shaft. This was accomplished via the locational fit into the shroud. Since the air bearing operates under high pressure and temperature, the leaves and outer body were all produced from Inconel.

www.manaraa.com

### 3.2.4 Shroud.

Between the two end walls and encompassing the rotor was the shroud. The shroud design could not be finalized until the end walls, air bearing, and rotor dimensions were known. This was due to the tolerance specifications of DMLS printing. The shroud's radial dimensions had to be controlled to a 0.0254 mm tolerance for the various interference fits with the other components. Therefore, the shroud was not manufactured until the necessary measurements of the actual interfacing components were determined. The shroud, as shown in Figure 22, was a hollow cylindrical piece. The inner volume of the shroud was designed for a locational fit. As can be seen, a step is located near the right end of the shroud. This step allowed the air bearing to sit against it and using a short ring that slid in behind the bearing this step held the air bearing in place axially. The ring and the step, preventing the bearing from moving axially, were designed to keep the hydrodynamic pressures centered on the rotor. Centering these pressures prevented any uneven force that could have caused the rotor to wobble. The walls of the shroud were approximately 1.55 mm due to a need to match the bolt pattern of the shroud to that of the endwalls. While this seems thin, a thin walled pressure vessel such as one this mimics is capable of containing far greater than the average inner pressure of 197 kPa. The thin walls came from the required bolt pattern.

The flange-like portions at the end were designed to accommodate a 6-32 screw head. The heads on 6-32 socket caps were approximately 5.7 mm in diameter. To permit this size with some clearance, the flanges were designed to be 6.35 mm tall with the bolt hole centered within them. An issue with the endwalls led to a new requirement of 8-32 screws. The head of an 8-32 screw is about 7 mm in diameter. Because of the precise sizing requirements as dictated by the air bearing's outer diameter and the bolt circle for the two end walls, making a larger flange height to

60
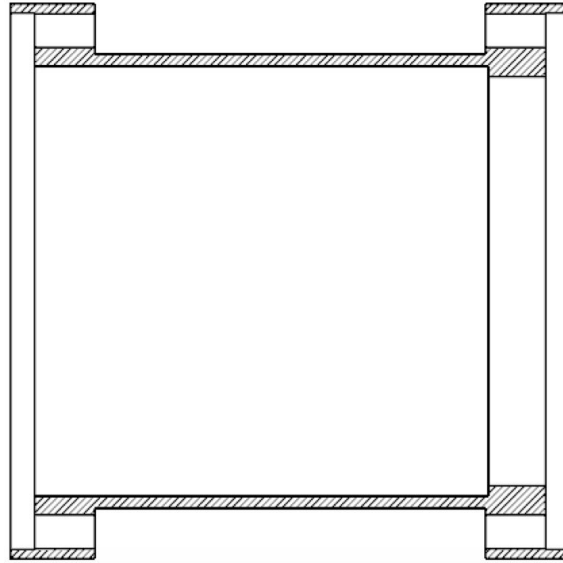
**Figure 22. Cutaway View of Shroud CAD Model**

accommodate the larger screwhead was not an option. Therefore, the holes were sized to allow an 8-32 to slide through but the heads of the screws would later be ground down to approximately 6 mm to fit the flange.

The last features of the main shroud piece are the lips that extend axially. These were the previously discussed lips to ensure centerlines' alignment by maintaining concentricity between the shroud and the endwalls. Unlike the components discussed previously, the shroud was a simple enough design that it was machined in-house and produced from stainless steel 304.

### 3.2.5  Motor Mount.

The final aspect of the wave rotor design was the lower half of the motor mount. The upper half of the mount was previously designed to test the other small wave rotors within the facility as they all utilized the same electric motor. The lower half of the motor mount coupled to the inlet wall with the three-hole pattern using 6-32 screws. The mount, shown in Figure 23, had an open central area that was sized

61

such that it was the length needed to couple the shaft to the motor with the claw couplings. Also shown on the right half of Figure 23 is the previously designed upper half with the motor installed.

Similar to the connection between the shroud and end walls, the upper and lower half of the motor mounts align with a raised ridge concentric to the motor's centerline that fits into a depressed annulus on the lower half. The lower half also uses a similar sort of feature to center itself within the inlet wall. It used a raised ridge a few millimeters long to align itself with the shaft hole and keeps everything else concentric.



**Figure 23. Upper Half of the Motor Mount (left), Lower Half of the Motor Mount (right)**

## 3.3 Combustor Design

The design from the Q1D code stipulated that the pressure decreased by about 42 kPa between the CO and TI ports of the wave rotor, while the temperature rose approximately 450 K at the design point. Note that while the absolute pressure drop varies with throttle changes, the pressure drop averages about 10.8% of the CO pressure. This pressure and temperature change is characteristic of a typical jet engine combustor. Note that the combustor itself was designed to be a 5% drop with the remainder off the pressure drop due to the plumbing to the combustor. Initially

62

a COTS burner was planned for this research. However, it became apparent that a COTS burner matching the requirements for the wave rotor was not available. Therefore, a combustor design became integral to the research. After briefly looking into swirl-stabilized combustors, a meeting with Mr.Dave Burrus of ISSI led to a simple can-combustor design shrunk down to accommodate the small flow rate. The can design was chosen for its simplicity as well as the relatively low pressure drop associated with these combustors. The combustor design was a two-step process. The first step was to design the combustor itself, specifically the can and the dome, while the second step was to design the plumbing and connections to the wave rotor endwalls.

### 3.3.1 Can Design.

With the help of Mr.Burrus, a simple can design consisting of multi-sectioned can approximately 190 mm long with an average inner diameter of 64 mm was conceived. The combustor design, shown in Figure 24, had five annular sections with the first acting as the attachment point for the dome and the other four were the liners containing the combustion zone. Each panel was 44.5 mm long with about 4.6 mm of overlap to weld together. All of the can components, with the exception of the swirler, were machined from Inconel 718 rods while the outer shell shown in the figure below is a 3" (76.2 mm) stainless steel 304 pipe. The manufactured can without the dome installed can be seen in Figure 25.

Warm, pressurized air arrived through the plumbing from CO as the inlet feed to the combustor. The plenum flow had a design point of 2.12 kg/min of air entering the combustor at 786 K and 384 kPa. Beginning at the upstream end of the combustor, left in Figure 24, the dome and the swirler are the first components in the mass flow's path through the combustor itself. Twenty percent of the mass flow enters the

63
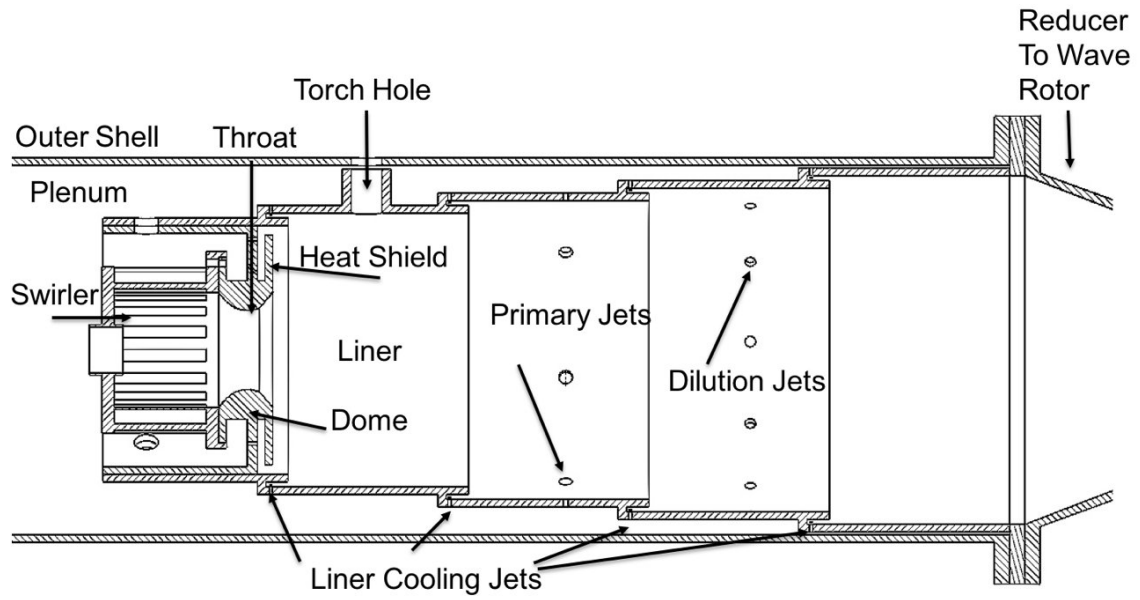
**Figure 24. Combustor Drawing Cutaway with Labels**



**Figure 25. Manufactured Can**

64

combustor through the swirler. The swirler, as shown after manufacture in Figure 26, was a DMLS part that utilized 15 passages angled at 30° to inject mass flow into the combustor dome radially with the pressure gradient pulling the unburnt reactants downstream through the throat and around the fuel line (not shown in the figure but located along the centerline of the swirler). Based upon the advice of Mr. Burrus as well as the sizing and material strength limitations, the swirler design was relatively simple. The desired mass flow rate as well as the density and bulk fluid velocity through the swirler were known and therefore, the area was easily calculated. Combining the total passage area with the dimensions the swirler had to fit within as well as the necessary wall thickness required for manufacturing, the approximate number of passages was quickly calculated. Their angle was found by iterating the number of passages with the total flow area of the inner radius and the cylindrical dimensions until the swirler fit within the dome.



**Figure 26. Radial Swirler**

Ethylene was chosen as the fuel for the burner. This was because it was readily available within the facility and was gaseous at the inlet conditions making mixing and ignition relatively simple compared to more conventional liquid fuels. The ethylene utilized an injector that impinged the gaseous vapor on the dome just prior to the

65

throat. The mixture of fuel and air then passed through the throat and entered the primary combustion zone located just downstream of the heat shield. Just upstream of the heat shield were three rings of injection holes that provided cooling to the heat shield. The shield cooling air was designed to be approximately 10% of the total air flow and because it actively entered the combustion zone was not included in the cooling fraction of the total mass flow rate.

Note that the heat shield and the throat face are a single piece and attached to a separate annular section. This section, the dome, was designed to be a removable piece. This piece also included the attachment point for the swirler for a variety of reasons. The swirler was made removable to allow for multiple radial swirler designs to optimize pressure drop or some other potential flow characteristics such as a different flow area. The remainder of the dome components were made separate in case they needed to be repaired. For example, excessive temperature loading on the heat shield could cause it to bend and close the cooling gap or perhaps a different throat size is needed. Making the dome removable allowed for a modularity depending on available components. The manufactured dome, heat shield up, can be seen in Figure 27.



**Figure 27. Combustor Dome**

The recirculating primary combustion zone was reinforced by the primary jets injecting 25% of the total mass flow radially approximately 63.5 mm downstream of the heat shield. Their purpose was to create the recirculation that enabled the can to be kept short compared to the typical laminar flame length of an ethylene-air flame. The recirculation created by the radial injection caused turbulent eddies to form vigorously mixing the flame with the unburnt mixture. During this process the fuel-air mixture had a relatively rich equivalence ratio, estimated at approximately 0.72, when compared to the global equivalence ratio as the primary zone contained all of the fuel but only around 55% of the total air mass flow rate. The middle annulus contained all eight primary jet holes with each hole being 2.77 mm in diameter. The global equivalence ratio was estimated to be around 0.4 based on the necessary temperature rise and the heating value of ethylene. Equations 13-15 along with Table 3 show this. Note $F/A$ is air to fuel ratios, $LHV$ is the lower heating value of the fuel, $C_P$ is the specific heat, and $F/A_{stoic}$ is the stoichiometric air to fuel ratio.

$$\frac{F}{A} = \frac{\frac{T_{TI}}{T_{CO}} - 1}{\frac{LHV_{C_2H_4}}{C_{Pavg}T_{CO}} - \frac{T_{TI}}{T_{CO}}} \tag{13}$$

$$\dot{m}_{fuel} = \frac{F}{A}\dot{m}_{air} \tag{14}$$

$$\phi = \frac{\frac{F}{A}}{\frac{F}{A}_{stoic}} \tag{15}$$

After the flow moved beyond the primary jets, it encountered the twelve 2.51 mm dilution jets, which injected cooler, fresher air radially to cool the exiting combustion products to the desired exit temperature and smooth out the pattern factor. The dilution jets injected 20% of the total mass flow into the center of the can. The final 25% of the mass flow was used to cool the liner and will be discussed in the

67

Table 3. Fuel Flow and Equivalence Ratio Estimates

| $\frac{A}{F}_{stoic}$ | 14.687 | $LHV_{C2H4}$ | 47.2 MJ/kg | $Cp_{C2H4}$ | 2.65 kJ/kg |
|---|---|---|---|---|---|
| $T_{TI}$ | 1233 K | $T_{CO}$ | 785 K | $\frac{A}{F}_{global}$ | 37.06 |
| $\phi_{global}$ | 0.40 | $\frac{A}{F}_{rich}$ | 20.38 | $\phi_{rich}$ | 0.72 |
| Global Air Flow Rate | 2.12 kg/min | Primary Zone Air Flow Rate | 1.17 kg/min | Fuel Flow Rate | 0.057 kg/min |

following paragraphs. The global equivalence ratio includes the cooling and dilution jet mass flows and was calculated with the total fuel and total mass flow through the combustor. Because of the richness in the primary combustion zone, the fuel leaned out as more air was injected into the combustor simultaneous to the fuel being burnt. The mass flow distribution is shown in Table 4.

Table 4. Mass Flow Distribution Through the Combustor

| Mixer | 20.5% |
|---|---|
| Shield Air | 9.4% |
| Primary Jets | 25% |
| Dilution Jets | 20% |
| Cooling Air | 25.1% |

The cooling air entered along the four downstream annuluses of the liner where each annulus had 38 cooling holes evenly spaced on the overlap portion. Each of the cooling holes were 0.7 mm in diameter while the overlap was 5 mm long. This overlap, in addition to providing a weld point, also directed the cooling air axially along the liner preventing direct contact between the hot combusting gases and the metal liner. To ensure the cooling air was being injected, momentum ratios were computed for each panel with the first and smallest annulus having a momentum ratio near 2.0 while the largest section was still greater than the 1.0 necessary to not have recirculation. The momentum ratios are calculated according to Equation 16.

68

$$MR = \frac{q_{panel}}{q_{dome}} = \frac{\rho v_{panel}^2}{\rho v_{dome}^2} \tag{16}$$

Note $q$ is the dynamic pressure and $v$ is the axial velocity. The dome axial velocities were assumed to be those seen immediately upon reaching the lip of the overhang while the dome velocity is the bulk flow velocity exiting through the dome's throat. The values for each panel are shown in Table 5. Note that in the table the annuluses are labeled 1-4 where 1 was the furthest upstream and 4 was the furthest final one downstream. The fully assembled can burner can be seen in Figure 28.

Table 5. Momentum Ratios for Combustor Liner

| Annulus | Density (kg/m$^3$) | Velocity (m/s) | Dynamic Pressure (Pa) | Ratio |
|---------|--------------------|----------------|------------------------|-------|
| Dome | 0.855 | 7.67 | 50.3 | - |
| 1 | 1.664 | 7.79 | 100.9 | 2.00 |
| 2 | 1.664 | 7.12 | 84.36 | 1.68 |
| 3 | 1.664 | 6.56 | 71.61 | 1.42 |
| 4 | 1.664 | 6.08 | 61.51 | 1.22 |



Figure 28. Assembled Combustor Can

69

A final design feature of the combustor can was the inclusion of a torch for ignition. The torch, shown in Figure 29, was a simple but robust method to ensure reliable ignition during start up. Because the torch had to traverse the plenum and exit the outer shell to connect to the spark power, air, and hydrogen supplies, a more conventional sparkplug was discarded as an option. This was due to the 785 K inlet air within the plenum, which could cause significant operational issues to the sparkplug as the casing is not designed to sit in that environment. A stainless steel tube with a filament within it would be capable of withstanding this environment.
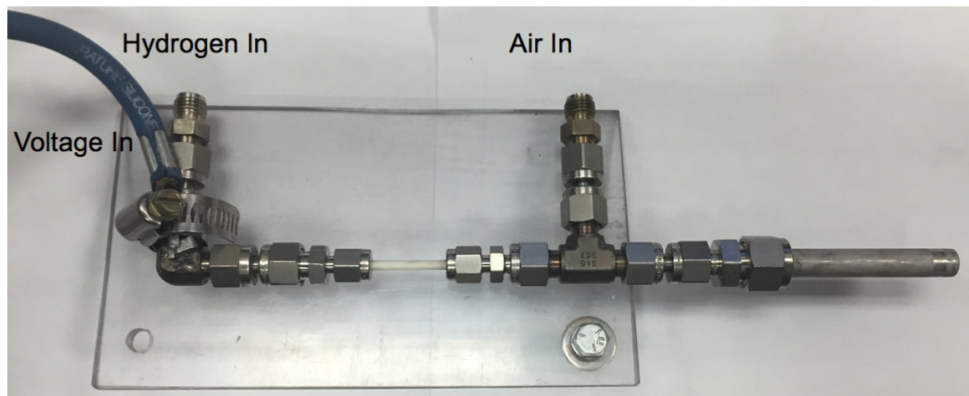


**Figure 29. Torch Ignitor Used for Start Up**

Two ports outside the outer shell flowed pressurized air (right connection above) and hydrogen fuel (left connection) down the tube and a single filament, when powered, would arc to the tubing and create a flame jetting into the center of the combustor. The cable seen to the far left of the figure is the power line that connected the filament to the power supply. This flame would then ignite the fuel-air mixture within the combustor. After a stable flame existed, the ignitor would be shut down so no extra mass flow was introduced to the system.

Between the combustor exit plane and the entrance to the TI pathways, a custom reducer was originally designed to reduce the flow area from an approximately 77.7 mm diameter circle to one with the area of a 33.3 mm diameter circle. This also

70

needed to happen very quickly to reduce heat loss. Utilizing the favorable pressure gradient produced by TI's opening to the ambient air, this was done in approximately 51 mm. This corresponds to a 66.48° angle as shown in Figure 30. The ends of the reducer would each have flanges to connect to either the wave rotor TI pathway or the combustor exit.
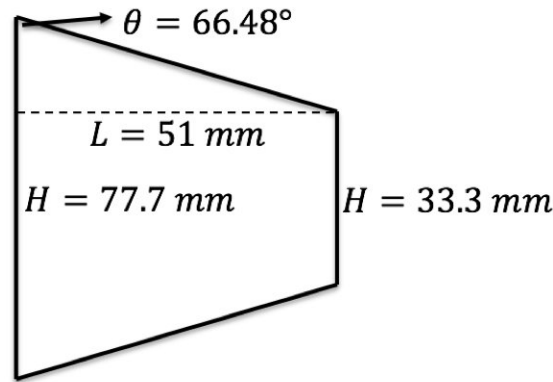


Figure 30. Geometry of Reducer

This design was later changed to be a simple conical stainless steel 304 reducer from 3" pipe to 1.5" pipe. 1.5" pipe inner diameter is close enough in size to the OD of a 1.5" (33.3 mm) tube that it can be welded inside. Then a flange was fitted to the other end of the tube to connect back to the wave rotor. This piece was also slightly longer than the custom piece at 88.9 mm without the flanges. This change was purely due to cost. It was far cheaper to purchase a reducer and weld short tubing section and the flanges to it then to fabricate the entire reducer from scratch.

Not to be overlooked for the design were the gaskets between all of the flanges. Initially the intention was to manufacture gaskets out of graphite similar to the majority of the high pressure lines within the facility. This high-temperature graphfoil was limited to operating conditions less than 730 K. Therefore, the gaskets located downstream of the combustor would potentially melt. This led to the use of metal-faced vermiculite. This material has electrolytic tin plated surfaces with the vermiculite

71

core. This setup is able to withstand operating conditions up to 1275 K and is designed to handle the expansion and contraction of multiple heating cycles. It is also resistive to vibration, a bonus given the vibromechnical loads on the system from the rotor rotation. All gaskets were approximately 1.6 mm thick prior to outgassing.

### 3.3.2   Combustor Plumbing.

The remainder of the combustor plumbing moved the air from the CO exit of the end wall to the plenum. This was done with four distinct pieces. The first of these was a 1.5" (33.1 mm) pipe flex line. Originally this piece was not in the design; however, due to thermal growth, it was added. Given the temperature difference that the reducer back to the wave rotor will see compared with the plumbing immediately following CO, about 2.5 mm of difference will be present in the two parallel straights. Additionally, the distance between the two parallel straights will increase by about 2.0 mm. This thermal gradient would cause one of two issues. Either the flanges on the endwalls would be damaged or the stainless steel plumbing would crack and break. The other three components consist of an off-center expander, a wye piece, and a U bend. The off-center reducer expanded the flow area from 1.5" tube ID (33.1 mm) to 3" tube ID (72.6 mm). From here, the larger reducer end was welded into a 3" pipe as the OD of a 3" tube fits inside the ID of schedule 40 3" pipe (77.7 mm). This 3" pipe was the the wye piece. A wye was used in order to permit start up air to be injected into the rig. The other end of the wye was welded to the U. Most of the plumbing can be seen connected to the the wave rotor in Figure 31 however the flex line is not shown and the reducer has not been welded into the wye. This figure was the initial design that would have utilized a short tubing section to overcome the gap shown.

72
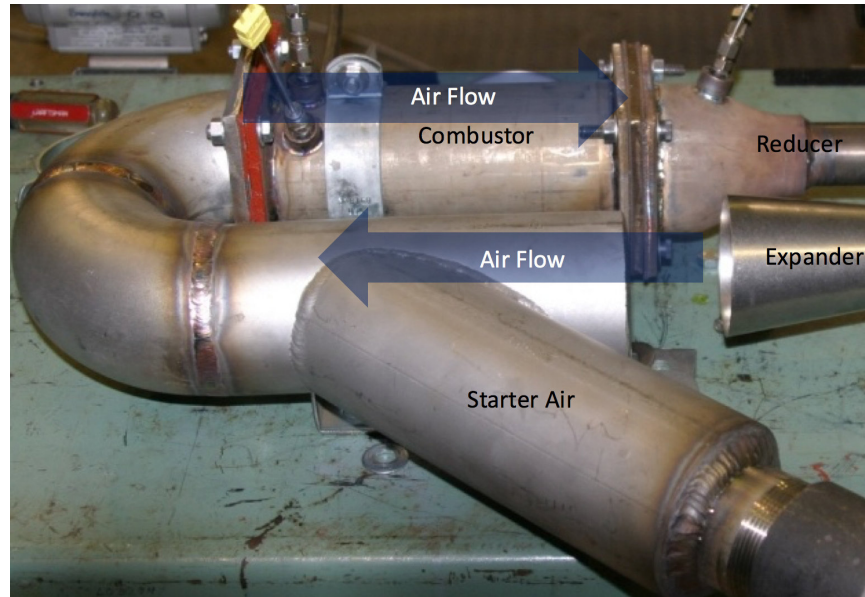
**Figure 31. Incomplete Plumbing, Missing Flex Line**

The unwelded end of the custom U was fitted with a flange that would connect to the plenum. Making a 180° turn in the tight manner this design required necessitated a standoff distance between the end of the turn and the combustor dome. This standoff distance was needed to ensure the flow has smoothed out from the likely separation occurring along the inner part of the curve. The separation and the turbulence it generates could cause flow injection issues to the combustor if they propagate too far downstream. These injection issues could lead to hot spots along the liner eventually causing leaks in the flame containment. This would end the combustor's usable life span if not repairable. Beginning with the reducer and tracing the flow path backwards the lengths of all of the burner loop components are given in Table 6. An image of these components is shown at the end of this Chapter as the components have not been completed yet.

Table 6. Lengths for Combustor Plumbing

| Component | Length (mm) |
|---|---|
| Reducer to TI Port | 197 |
| Combustor Plenum | 210 |
| U Bend (Burner Side) | 229 |
| U Bend (width) | 229 |
| Wye and U Bend | 337 |
| Expander | 159 |
| Flex Line | 203 |

## 3.4  Data Acquisition

The DAQ chassis and DAQ cards used to record temperatures and pressures for the venturi testing were the same ones used for all of the succeeding tests. The chassis was manufactured by National Instruments (NI) and was a cDAQ-9184. Four different DAQ cards were used. The thermocouple card was a NI-9214 with available channels for eight distinct temperature measurements. Depending on the test, one to seven of these channels were used. Two different types of pressure DAQ cards were used although both were NI 9215s. One had four BNC input channels while the other had eight channels to wire pressure transducers in directly. In addition to the DAQ equipment, the pressure transducers all had to be powered with 28 V. This was done using a variable output BK Precision DC Regulated Power Supply. A variety of different types of pressure transducers were used throughout. The Omegadyne PX-329's had a reported error of 0.25% full scale. The Omegadyne PX-429's had a reported error of 0.08%. The Honeywell Sensotec absolute pressure transducers had a reported error of 0.05% while the Honeywell differentials were accurate to within 0.1%. The K-type thermocouples had a reported error of 0.75% above 273 K.

Once testing proceeded to the point that the wave rotor was spinning, the fourth DAQ card was needed to measure the digital signal from the motor. This digital

74

signal was divided by the number of pole pairs (2) in order to output motor and thus rotor RPM. The digital signal was sampled at approximately 4000 Hz. A 4000 Hz collection rate ensures a sample is taken every 0.25 ms. 38,500 RPM is equivalent to 641.67 Hz, and therefore the 4000 Hz sampling frequency will sample at least 1.5 times between pole passes.

## 3.5 Venturi Design and Calibration

### 3.5.1 Design.

This research required the use of two venturis to monitor the mass flow into and out of the system. One was the air intake leading to the CI port on the inlet wall and the other was the final dump back to ambient after the TO flow exited the exit wall. The latter venturi also attached to a gate valve to provide back pressure on the system if necessary. The venturis were used to monitor the mass flow of the system ensuring no leakage was occurring. A balanced mass flow between CI and TO indicated there was no leakage. Note that balanced refers to the TO flow rate equating to the CI flow and the fuel flow rates. Knowing the exact mass flow was also necessary to know where the wave rotor was operating with relation to the design point.

The design and build of the two venturis was done by Fox Venturi of Fox Valve Development Corporation. After providing them with the flow rate, fluid type, temperature, pressure, and approximate ratio of specific heats, they produced a design for each. Their designs specified length and throat diameter. The throat diameters were different due to the vastly different conditions flowing through them. The TO venturi had a density about half that of the CI venturi but the exit velocity did not increase enough to counteract this stipulating the area increase. Also included in their design process were options for measurement devices (Swagelok NPT fittings) and the connection type (buttweld to 1.5" (33.1 mm) tubing). Lastly, a few material

choices were given and stainless steel 304 was chosen. The various parameters are given for each in Table 7. The fully assembled venturis can be seen in Figure 32.

Table 7. Venturi Design Parameters and Throat Diameter

|  | CI Venturi | TO Venturi |
|---|---|---|
| Temperature (K) | 288 | 885 |
| Pressure (kPa) | 101.3 | 133.4 |
| Ratio of Specifc Heats | 1.4 | 1.35 |
| Flow rate (kg/min) | 1.59 | 1.59 |
| Throat Diameter (mm) | 20.07 | 23.88 |
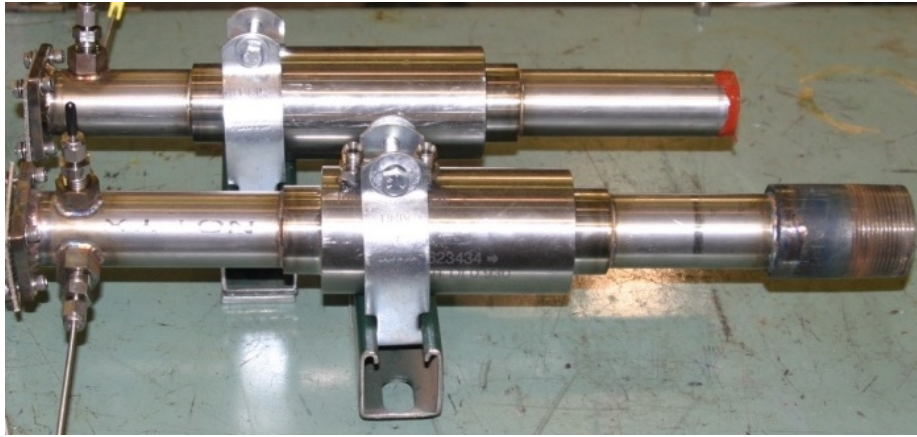


Figure 32. Venturis (CI top, TO bottom)

System level design for the venturis required a few more components. The venturis included ports to instrument static pressure at its inlet and throat but the wave rotor rig would require more measurements as depicted schematically in Figures 33 and 34. Additionally, they had to be fit with tubing of appropriate lengths to steady the flow. Convention dictates the tubing length into a venturi's inlet be 5 throat diameters long. Because the throat diameters were so close in size and to add in some extra margin, 127 mm inlet lines were added. Additional lines had to be added to the outlet of each. A short 77 mm line was added to the TO venturi and a 152 mm line was welded into the back of the CI venturi. Both venturis required flanges welded to one

76

end to attach to the correct endwall port as well as a thermocouple and a port to place a Kiel probe to a pressure transducer. The ports for the measurement devices were placed near the flanges. On the CI line, the flange was at the end of the outflow tube while the TO venturi had the flange and ports at the very front. Note that in Figure 34 the gate valve, if needed, would be to the right of the hardware shown.
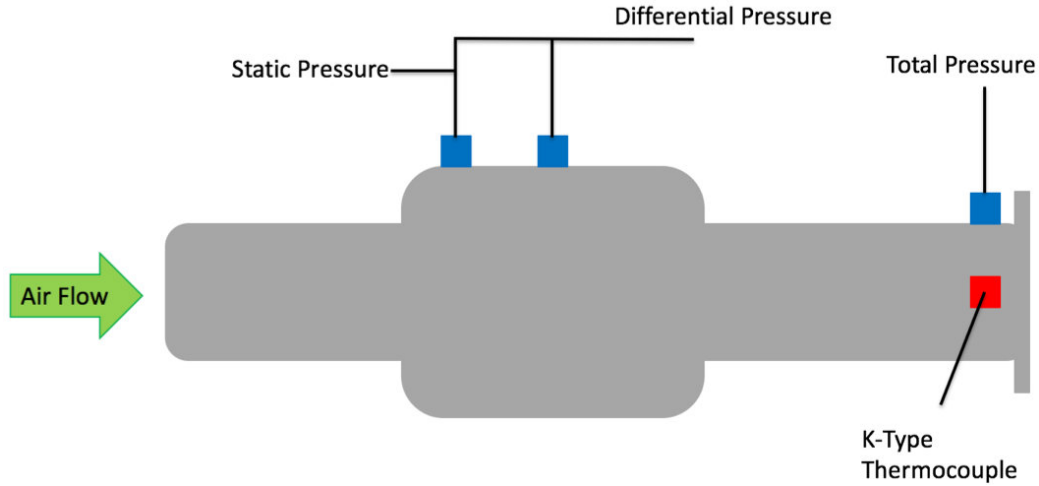


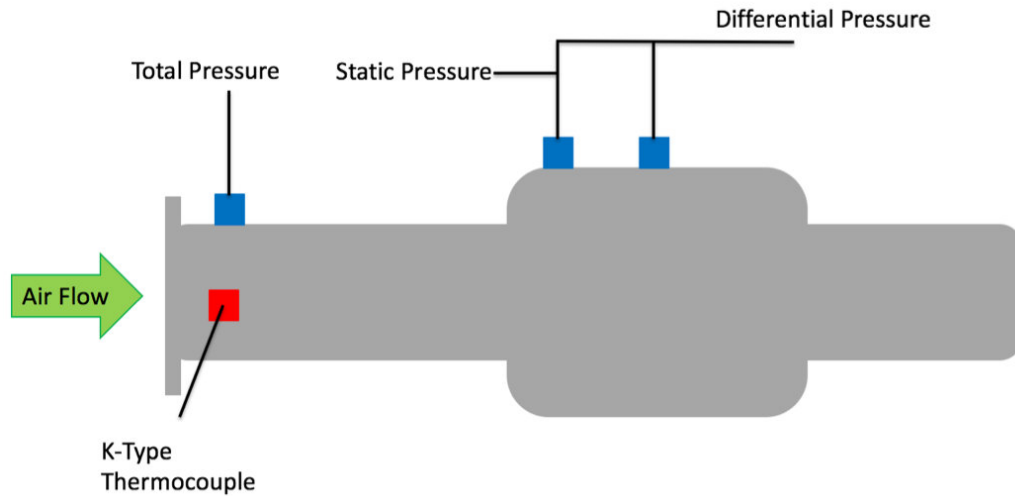**Figure 33. CI Venturi with Hardware**



**Figure 34. TO Venturi with Hardware**

In the two figures there are multiple flow measurements being taken within the

venturis. The total pressure and temperature measurements are the CI and TO measurements that will be compared to the code with the TO values also being used to calculate available power. The static pressure and differential pressure were needed to measure the mass flow rate through the venturis using the equations discussed in the next section. Both venturis used the same types of measurement devices: a K-type thermocouple, a 0-50 psia (0-344.7 kPa) Omegadyne PX-329 pressure transducer for the static pressure, a 0-1 psid (0-6.9 kPad) Honeywell Sensotec differential transducer, and a 0-50 psia (0-344.7 kPa) Omegadyne PX-429 pressure transducer to measure the total pressure. The total pressure measurements utilize KB3-C Kiel probes manufactured by United Sensor Corp.

### 3.5.2 Venturi Calibration.

In order to accurately measure the mass flow through the venturis, a known mass flow had to be passed through them and, using the equations below, a discharge coefficient calculated [42]. Using this known discharge coefficient and the active pressure and temperature measurements, the mass flow could be calculated in real time. Equation 17 is the mass flow calculation through a venturi with the succeeding equations explaining the various terms within the equation. Note that the subscript 1 refers to the inlet and 2 is the throat while $d$ is the throat diameter and $D$ the inlet diameter. Equation 21 provides the uncertainty measurement for the calculated parts of this equation while everything else is already written in terms of measureable quantities, with the exception of density which is calculated in Equation 22. The $R$ is the specific gas constant for air, $C$ is the discharge coefficient, $P$ is pressure, $\rho$ is density, and $T$ is temperature.

$$\dot{m} = \frac{CYA_2}{\sqrt{1 - (\frac{A_2}{A_1})^2}}\sqrt{2\rho_1(P_2 - P_1)} \tag{17}$$

$$Y = \sqrt{r^{\frac{2}{\gamma}} \frac{\gamma}{\gamma - 1} \frac{1 - r^{\frac{\gamma-1}{\gamma}}}{1 - r} \frac{1 - \beta^4}{1 - \beta^4 r^{\frac{2}{\gamma}}}} \tag{18}$$

$$r = \frac{P_2}{P_1} \tag{19}$$

$$\beta = \frac{d}{D} \tag{20}$$

$$Y_{uncert} = \pm \left( (4 + 100\beta^8) \frac{P_2 - P_1}{P_1} \right)\% \tag{21}$$

$$\rho = \frac{P}{RT} \tag{22}$$

To calibrate the venturis, they were connected to the facility air supply. This air was compressed by two Sullair TS32 compressors that discharged and stored the air in two large tanks at pressures up to 1014 kPa. With the main air valve on, the flow path was selected in the control program and the desired mass flow rate was set. The control program specified air flow in units of pound (mass) per minute and at the low flow rates necessary for this calibration, the flow rates could be held accurate to 0.01 lbm/min (0.045 kg/min). The air flow was metered by passing it through Flowmaxx sonic nozzles and pressure measurements on each side of the sonic nozzle were used to calculate the mass flow similarly to the venturi calculation above. Eventually, the plumbing was necked down from a 2" (50.8 mm) pipe to a 1" (25.4 mm) pipe size and plastic flex lines connected the air supply to the venturi being calibrated. This final part can be seen in Figure 35.

Figure 35 shows not only the venturi connected to the air supply but also the thermocouple and pressure ports. Note the plugged port near the venturi is a total

79
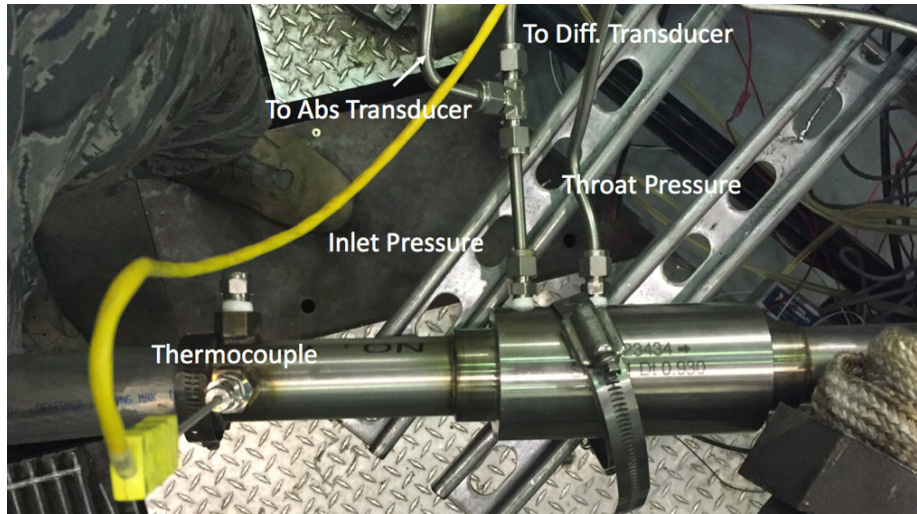
**Figure 35. Venturi Calibration Set Up**

pressure port that while necessary to measure the pressure during wave rotor operation, was not necessary for flow calibration. The two metal tubes are the static measurements. The upstream port (flow is moving left to right) is the inlet static pressure. The tee allowed both the measurement of the inlet static pressure as well as a differencing through the differential transducer.

Because the control program works in Imperial units, most of values presented in the following paragraphs will be Imperial with metric in parenthesis. The venturis' design mass flow rate is 3.51 lbm/min (1.59 kg/min). The initial flow calibration looked to test a flow range above and below this. This range was 1.25 lbm/min to 5.50 lbm/min (0.57 kg/min to 2.49 kg/min). The data reduction to determine the discharge coefficient, $C$ in Equation 17, will be discussed further in the next section. Those results for the TO venturi ($D_t$=23.88 mm) stipulated a second calibration set as a significant amount of the flow points were within the bottom 10% of the differential transducer's range. The second range tested spanned 2.75 lbm/min to 7.50 lbm/min (1.25 kg/min to 3.40 kg/min) and occupied 11% to 88% of the full scale of the transducers measurement range.

### 3.5.3   Venturi Discharge Coefficients.

For the CI venturi, though the range of 1.25 lbm/min to 5.5 lbm/min (0.57 kg/min to 2.49 kg/min) was tested, a few data points were within the top or bottom 10% of the differential transducer range and therefore were neglected. The range used for the calibration was 1.75 lbm/min to 5.00 lbm/min (0.79 kg/min to 2.27 kg/min). Following the equations above, the average discharge coefficient was calculated to be 0.951. The full discharge coefficients spanned from 0.937 to 0.963. A tight band was expected. Of note is one of the points was very close to the design point of 1.59 kg/min or 3.51 lbm/min. 3.50 lbm/min was a tested point and yielded a discharge coefficient of 0.956. Because the equations provided above also included an uncertainty calculation for Y, the measurement uncertainty was determined, and the largest Y uncertainty of 0.36% was used for all calculations in an effort to assume the worst case scenario. Using the standard Kline-McClintock method for uncertainty, the discharge coefficient's uncertainty was calculated with one caveat. The caveat is an assumed 5% error in the mass flow. Previous work has shown an uncertainty of a couple percent for mass flow at the sonic nozzle, however, this does not account for the leakage between the sonic nozzle and the test setup. Future work looks to quantify this area in order to attain a more accurate mass flow error. This analysis led to a discharge coefficient of 0.951 ±0.019.

The TO venturi was tested over the initial range yielded discharge coefficients between 0.69 and 0.95. This large discrepancy was the alert to the differential transducer operating within the measurement noise. After retesting the venturi over the 2.75 lbm/min to 7.50 lbm/min (1.25 kg/min to 3.40 kg/min) range, a much tighter span of discharge coefficients was calculated. They spanned 0.957 to 0.974 with an average of 0.967. Although the design point mass flow was tested, it was not tested at the elevated temperature and pressure expected during operation so reporting the

81

discharge coefficient for the mass flow near the design point could be potentially mis-leading. The Y uncertainty for this venturi was 0.56% over the larger range. The same uncertainty analysis for the TO venturi led to a discharge coefficient of 0.967 ±0.009.

## 3.6  Injector Nozzle Testing

### 3.6.1  Injector Test Setup.

One of the key aspects of any combustor is the fuel injection method. This research used Delavan peanut nozzles. The facility for this testing had a variety of different nozzles spanning a range of flow numbers from previous work. All of the nozzles available on-site were sized for 1/4-32 threads and approximately 12 mm long. The flow number, Equation 23, characterizes each nozzle by its fuel flow rate and the pressure differential between the injection pressure and the pressure of the fluid being injected into. A differential of at least 172.4 kPa is desired for full expansion of the cone. In Equation 23, $\dot{W}$ is the fuel flow rate in lbm/hr and $\Delta$P is in psid. The English units are necessary as the flow number will change based on the units used.

$$FN = \frac{\dot{W}}{\sqrt{\Delta P}} \tag{23}$$

Although the facility had flow numbers for a variety of fuels tabulated, it did not have the cone angles for the different nozzles and these had to be experimentally determined. The cone angle of a nozzle is independent of injection media; therefore, water could be used for determination purposes. The setup, as shown in Figure 36, consisted of a concentric target at a known distance from the injection plane.

Because the test injected into air, the ambient pressure of 98.6 kPa was used as the reference pressure. This was done by attaching a bottle of compressed nitrogen gas

82

**Figure 36. Test Set-up of Peanut Injectors**

to a pressure vessel full of distilled water (shown in Figure 36) and setting a regulator to hold the pressure vessel at approximately 413.7 kPa. The plastic line was 3/8" (9.5 mm) tube and used a Swagelok piece to hold the injectors. A 3/8" tube plug was drilled and tapped for 1/4-32 threads to screw the injectors into place. The fitting going off to the right of the pressure vessel attached to the nitrogen bottle while the regulator shown was attached to a relief valve that would vent if the pressure vessel reached 100 psid (689.5 kPa differential).

### 3.6.2 Injector Results.

The test procedure was to place the injector in the hole on the plate above the target and turn the water flow on. Pictures were taken of the cone that formed while the nominal angle estimate was written down. Analysis of the cone angles was done by loading the pictures into a program such as MS Paint and counting pixels. Figure 37 outlines the triangle formed by the half angle of the cone. This enabled the exact

83

cone able to be determined within 1°.



**Figure 37. Devalan Nozzle Spray Cone Half-Angle Highlighted**

Although the full x-length in the above picture cannot be seen, it was known to be 152.4 mm as measured on the test stand. The inverse tangent of the y-length divided by the x-length yields the cone's spray half angle. With a known half angle and the diameter of the circle defining the impingement location, the axial position of the nozzle could be calculated. Nine injector nozzles were tested with three being clogged and two having almost no angle. The other four nozzles had half angles between 24° and 46°.

Calculating the exact angles of these four nozzles yielded half angles of 44°, 46°, 28° and 24°. Determining axial positions needed based on the impingement diameter resulted in the best injector for use in the combustor. Injector number 26 was chosen. It had a half angle of 44° and had to be 10.7 mm upstream of the dome. The results of all the injector nozzles can be seen in Table 8. Note that NF means no flow and NA is no angle.

Table 8. Results of Injector Testing

| Nozzle | 26 | 22 | 42 | 35 | 5 | 27 | 21 | 23 | 3 |
|---|---|---|---|---|---|---|---|---|---|
| Angle (°) | 43.8 | 45.7 | 28.1 | 24.1 | NA | NA | NF | NF | NF |
| Dist. (mm) | 10.7 | 11.1 | 11.7 | 12.2 | NA | NA | NF | NF | NF |

## 3.7 Combustor Test Setup

The combustor characterization was the first major experimental test of this research. Care was needed to evaluate the combustor due to the increased danger of the test as not only were fuels used but the temperatures were capable of causing significant damage to the surroundings if proper safety procedures were not followed. After the setup, the combustor was tested at the design point. Testing the design point followed ignition to maximize test time usage. Following the design point testing, the operating range of the combustor was characterized by modulating the air and fuel flow rates as well as varying inlet temperature and pressure.

### 3.7.1 Hardware Setup.

Before detailing the individual parts of the setup, it is worth noting that because the minimum temperature all aspects of the combustor would encounter is approximately 785 K for design point testing, all materials were either stainless steel or Inconel. This includes not only the plumbing and major components, but also the nuts, screws, and washers. This temperature required these materials as other forms of steel would potentially create blockages in the combustor due to oxidation particulate.

The testing did not incorporate any of the extra plumbing necessary for turning the air and expanding the flow area to 3" (76.2 mm) pipe, including it only included the can and the reducer back to the wave rotor. The test section, shown in Figure 38, differed such that it connected to a nipple and reducer rather than the plumbing

for the wave rotor coupling. This was a 3" (76.2 mm) to 2" (50.8 mm) pipe reducer and connected to the 2" (50.8 mm) pipe outlet from the air supply. The plenum shell was instrumented with a K-type thermocouple and a United Sensor KBC-3 SS Kiel probe coupled to a 0-150 psia (0-1034.2 kPa) Omegadyne pressure transducer in the same configuration needed for the coupled operation. These sensors measured the incoming conditions from the air supply. The combustor outflow was measured within the reducer using a K-type thermocouple and a United Sensor KBC-3 Inconel Kiel probe coupled to a 0-150 psia (0-1034.2 kPa) Omegadyne pressure transducer. The heated, vitiated air was supplied by a modified T-63 combustor using hydrogen as the fuel. The air supply to this was the same discussed previously in Section 3.5.2 other than one valve was switched to direct the air to the T-63 rather than an unheated outlet.
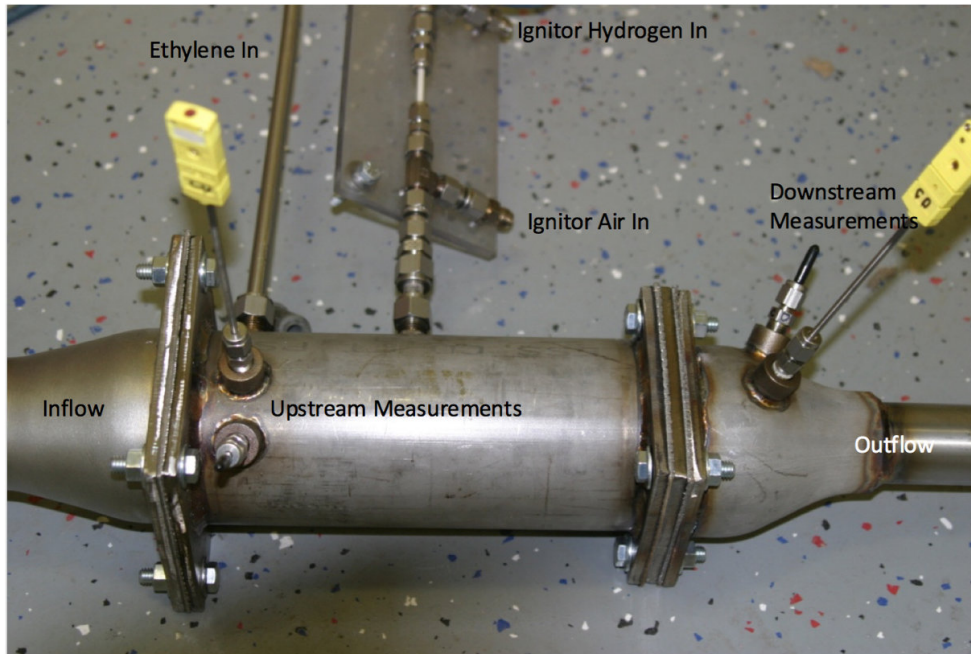


**Figure 38. Combustor Test Components**

The only portion of the test setup not shown in Figure 38 is the outlet. The outlet itself is a 1.5" (38.1 mm) tube with a flange to connect to the wave rotor TI port.

During the coupled operation, the outlet area was equal to 870 mm$^2$. It was also backpressured by the cavity pressure of the wave rotor, approximately 196 kPa. In order to match the pressurized conditions during the combustor characterization, a steel square was manufactured to attach to the flange and a hole was drilled into it. A hole with approximately a 11.5 mm diameter matched the backpressuring conditions.

The final component of the physical setup was the ignitor. Although design point testing occurred near the auto-ignition for ethylene, the combustor testing program required external ignition for all test points. With the ignitor locked in place, it utilized a third fuel line and a secondary air line. The ignitor used 0.23 kg/min of air and operated at an equivalence ratio of 0.3. The hydrogen and air lines were both pressurized to approximately 414 kPa in order to discharge into the pressurized burner operating at the design point in case flame reignition was required. For the ignitor to function properly, the gap between the steel ports for the fuel and air inlets had to be at least 2 cm apart to allow the air to dissipate the voltage to prevent arcing. Furthermore, a plastic port connector was needed between the hydrogen port and the line carrying the hydrogen from the pneumatic valve to prevent the current from grounding to the cart. Figure 39 shows a simple representation of the setup including the measurement locations and types of measurement.

Given that five separate, pressurized lines were necessary for operation, each had to be metered to calculate flow rates and equivalence ratios. This was accomplished through the use of five sonic nozzle or orifice set ups. The choke diameter and line size can be seen in Table 9. As previously stated, mass flow accuracy was assumed to be 5%.

Because this testing included combusting fuels and high temperatures, safety was a large component of this setup. The facility typically places two pneumatic valves on every single fuel interlocked to the test cell's door. If the door was open, no fuel
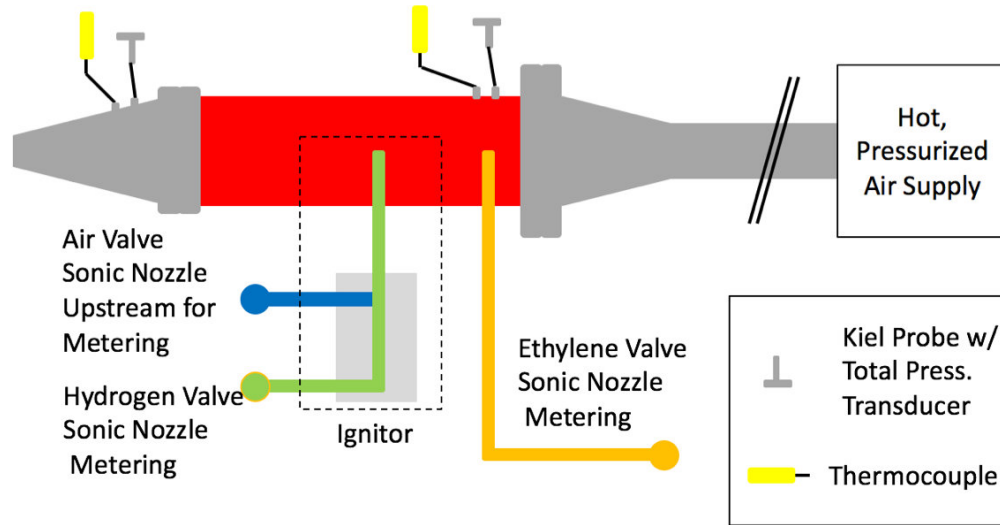
**Figure 39. Schematic of Combustor Test Setup**

**Table 9. Sonic Nozzle Diameters and Line Sizes**

| Line | Orifice Diameter | Line Size |
|---|---|---|
| Primary Air Supply | 6.40 mm (0.252") | 50.8 mm (2") |
| Primary Hydrogen Supply | 0.41 mm (0.016") | 25.4 mm (1") |
| Burner Ethylene Line | 0.69 mm (0.027") | 12.7 mm (0.5") |
| Ignitor Air | 1.65 mm (0.065") | 12.7 mm (0.5") |
| Ignitor Hydrogen | 0.04 mm (0.016") | 12.7 mm (0.5") |

could flow ensuring the safety of the people working inside. This experiment required the installation of three new valves on the test cart. Only three valves were required because the heated supply air already existed and required no modification. The three new valves controlled the ethylene flow and the ignitor flows. By including the valves on the test cart, the length of tubing between the valve and burner was minimized, therefore reducing the amount of fuel available in case of failure. All of this can be seen in Figure 40.

Prior to operation, the entire rig was pressurized to about 517 kPa in order to check for leaks. The initial check showed the upstream flange was leaking. Red RTV
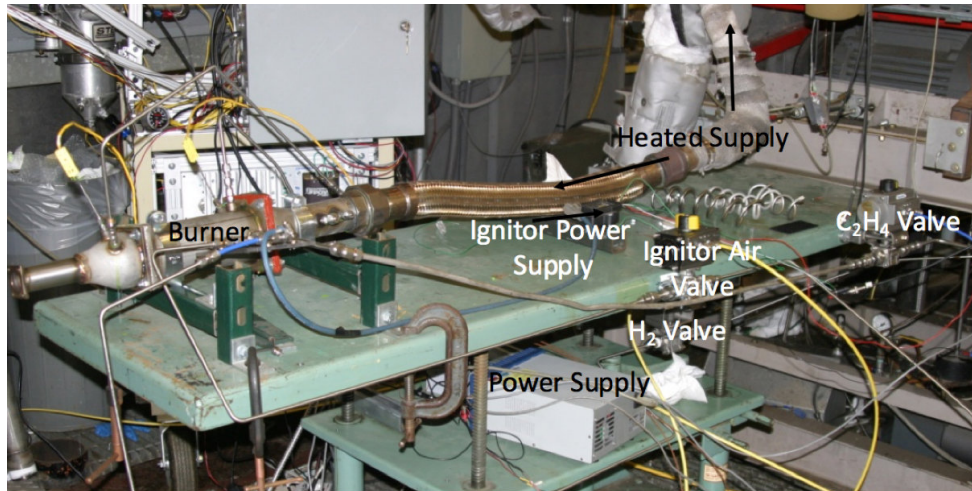
**Figure 40. Test Cart of Burner Test Connected to Supply**

was placed around the edge in an effort to decrease this leakage. One consideration was that the maximum operating temperature for red RTV is listed as 616 K and the inlet temperature is 785 K. Testing demonstrated there was enough heat loss to the surroundings that the RTV did not melt or evaporate away.

### 3.7.2 Design Point Testing.

This section outlines the general test procedures for running the various aspects of the test and gathering data. The two air lines were pressurized by connecting to dome loaders which are connected to a control computer. This allowed the mass flow rate to be varied during the test without shutting down the whole operation. The facility's setup allowed the hydrogen line to the heated air supply to be modulated in situ via a regulator valve; however, the ignitor hydrogen and the ethylene regulators could not be changed without entering the test cell. Therefore, these were set before the test began. In order to do this, the mass flow rate had to be known.

The ignitor flow rates were known from previous experiments. The air mass flow rate was 0.208 kg/min and the hydrogen flow rate was 0.0018 kg/min. Although

the air flow rate was metered by the dome loader, the hydrogen was run through a sonic nozzle with the upstream stagnation pressure, $P_0$, controlled by a regulator. This pressure was governed by Equation 24. Other terms within the equation are the nozzle discharge coefficient, $C$, throat diameter, $d$, hydrogen ratio of specific heats, $\gamma$ (1.41), hydrogen specific gas constant, $R$, and the gas temperature, $T$.

$$\dot{m} = C\frac{\pi d^2}{4}P_0\sqrt{\frac{\gamma}{RT}}\left(1 + \frac{\gamma - 1}{2}\right)^{\frac{-(\gamma+1)}{2(\gamma-1)}} \tag{24}$$

The calculated stagnation pressure is a gage pressure relative to the downstream pressure. The downstream sonic nozzle pressure is the desired inlet pressure to the combustor. The upstream pressure was found to be 59.8 psig as the regulator used Imperial units. The regulator pressures were set prior to the experiment by attaching the fuel lines to a nitrogen bottle and flowing this through while reading the output of the pressure transducer. Initially, the ethylene flow rate was intended to be set in a similar manner; however, changes were made to improve both testing speed and to ensure the metered ethylene flow was gaseous. The ethylene was stored in high pressure bottle in a supercritical state (850 psig, 5860 kPa). Although ethylene exits the bottle as a gas, a dramatic pressure drop could create a phase change to a liquid which could cause metering issues. To mitigate this, a regulator was placed on the bottle exit and limited the exiting pressure to 400 psig (2758 kPa). The 1/2" (12.7 mm) tube exiting the regulator also included a coil to increase the travel distance and thus surface area to pick up ambient heat. All of the ambient heat would ensure the ethylene was gaseous when it reached the dome loader and would remain so as the pressure dropped by half or more again.

The dome loader was a TESCOM Venting Regulator Model No. 26-2065D24A370 metered by a Control Air Inc Type 500X I/P pressure regulator. The pressure regulator had an inlet with a 100 psig nitrogen line and allowed between 3 and 120 psia

90

(20.7-827.4 kPa) output. It was electrically controlled with a 4-20 mA input. Rather than using a current supply, the resistance was measured to be approximately 268 Ohms. The 4-20 mA output corresponds to voltages between 0.80 V and 5.36 V. This enabled the dome loader to flow up to 1600 psig (11,031.6 kPa) of ethylene, a far greater pressure than needed for this experiment or delivered by the bottle.

Both sonic nozzle spool pieces use a Honeywell Sensotec 0-500 psia (0-3447.4 kPa) pressure transducer with a 0-5 V output. The hydrogen line has a 0-250 (0-1724.7 kPa) psia Omega PX-429 0-5 V output pressure transducer downstream while the ethylene has a 0-250 psia (0-1724.7 kPa) Omega PX-429 0-5 V downstream pressure transducer.

With the fuel line pressures set, the testing began. Supply air began flowing at 4.67 lbm/min (2.12 kg/min) and when the inlet to the combustor reached the appropriate temperature, the ignitor valves were opened. Once the ignitor was lit, the ethylene line was opened to allow fuel flow. Once the downstream thermocouple registered a temperature rise, the ignitor was shut down. A detailed step-by-step operating procedure for this part of the testing can be found in Appendix C.

Although most of the parameters were held constant over the testing sequence, the ethylene flow rate was actively metered to determine the exact amount needed to reach the 1235 K target exit temperature. This was done by adjusting the voltage on a variable power supply that connected to the dome loader's pressure regulator. Initial testing also permitted a deviation from the planned test procedure. Burner ignition did not require both fuel and air actively flowing through the ignitor; rather, ignition only required a minuscule amount of hydrogen doping of the fuel to light. This discovery simplified the procedure by removing the ignitor air flow steps from operation.

### 3.7.3 Ignition and Range Finding.

The remainder of the combustor testing looked to examine ignition at ambient conditions and examining the functional range. Given the approximately 1.5 hour warm up time to reach the inlet condition, it was decided to test the ignition in a time efficient manner. Beginning at 450 K, fuel flow and the ignitor were enabled approximately every 30 K to determine the minimum inlet conditions necessary for stable ignition. A stable ignition was one where a flame was sustained after the hydrogen fuel to the ignitor was shut off.

## 3.8 Wave Rotor Mechanical Test

In addition to testing the combustor in an uncoupled manner, the wave rotor components were assembled and spun up to the design RPM to look for any mechanical or vibrational issues. This test was a simple series of spinning the rotor up and down in an unpressurized, unheated manner.

### 3.8.1 Deadports.

It was during the setup for this testing that the final decision on a particular endwall feature was made. On previous pictures of the endwalls (Figures 18 and 19), there were closed ports on the active surfaces between air flow ports. These ports, typically called deadports, are useful for off-design operation in PWS wave rotor designs. As previous AFIT work was of the PWS type, they were included on this design. After the parts were printed, the oversight was realized and numerous discussions on mitigating them took place. These discussions entailed the necessity of blocking them and how to block them if it was needed. The downside to not blocking the ports would be reduced efficiency during operation at all conditions.

The first idea was to machine thin plates with the shaft and air ports machined

92

out to block the deadports. These plates had a fundamental flaw that would cause significant operational issues. Given the uneven heating on the thin plate, it would likely deform from the temperature gradient, especially on the inlet side. That bending would likely impact the rotor or shaft and could cause a mechanical or structural problem. The second idea was to pack the deadports with graphite and although the graphite is only rated to 730 K for use as a gasket, the melting point of graphite far exceeds the operating conditions of this work. The final idea was to weld the deadports closed, however, this would require many cycles as they would have to be filled in completely. If not completely filled, an air pocket could form within the end wall and undergo strange pressurizing and heating cycles during operation.

Given the high potential for issues with the first and third ideas, packing the deadports with graphite was determined to be the most sensible. Given that the rotor mechanical checkout would be unaffected by graphite in the endwalls, it was decided the wave rotor would be tested with unblocked ports and that the coupled, final setup would be run both with and without the blocked ports. The configuration with the open deadports is the least damped configuration; however, it has no pressure waves reflecting off the end walls due to a lack of energy exchange. During pressurized testing, graphite packing around the shafts to assist with sealing will add some damping to the system while the pressure wave reflections could alter the vibrational loading. Note that as none of the solutions has been implemented yet, no illustrations of the solutions exist.

### 3.8.2 Hardware Defects.

After receiving the DMLS parts, the endwalls required surface clean up for the active surfaces and the flanges. The exit wall also required clean up for the bearing cavity. Most of the clean up work for these parts was focused on the active surfaces

93

and the concentric ridge to ensure both parts were identical and perpendicular to the shaft. One of the dead ports on the exit wall also required some work to prevent leakage between it and the air ports. A tiny amount of material was welded into place and the surface was then ground flat.

The first rotor had zero issues as most of post-sintering machining was done, but the second rotor had a significant issue with the motor-side shaft. After sending the rotors out to be balanced, it was revealed the motor-side shaft was ground off-center by about 0.05 mm. This would cause a 0.10 mm wobble during operation making the rotor impossible to balance. The part was returned to the DMLS company, C&A Tool, and they reground the shaft down to a slightly undersized diameter (4.8 mm vs 5.0 mm) but it was centered and usable. The rotors are kept in separate wrappings with a 1 or 2 written on outside. 1 is the ground down shaft while 2 was the unmodified one. The numbering was arbitrary and done upon arrival to distinguish between them.

With the rotors produced and the shafts centered, they had to be balanced. The first time they were sent to The Balancing Company led to the discovery that the one shaft was ground off-center. The second time they were sent for balancing, the machinists removed material around the O.D. of the rotors near the edges giving the rotors a slightly tapered appearance; however, this tapering is too slight to appear in a photo.

### 3.8.3  Wave Rotor Setup and Test Plan.

The setup consisted of the wave rotor components and the motor. The only measurement taken during the testing was accomplished by the electronic speed controller (ESC). The ESC controlled took an input voltage and drove the motor. The motor, a Neumotors 1509-1/Y sensored motor, was capable of monitoring how often the poles passed a sensor. This number was then divided by two as the motor contained two

pole pairs. The final number was then converted to RPM. The setup can be seen in Figure 41.
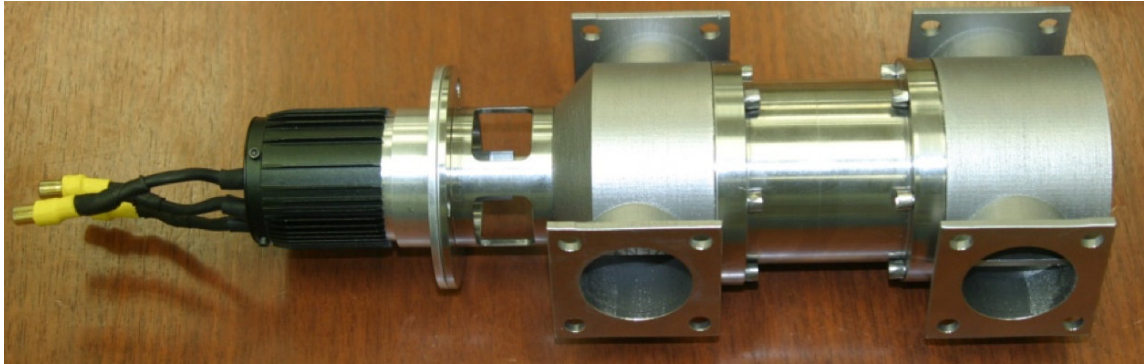


**Figure 41. Hardware Setup for Mechanical Checkout**

The first attempt to spin up the rotor used a standard Lovejoy L035 jaw coupling with a set screw and a SOX Nitrile Butadiene Rubber spider between the rotors. This setup is shown in Figure 42. Note that the gap between the coupling and the shaft is greatly exaggerated for illustration purposes. The set screw failed to transfer enough torque to the shaft for start up and only the coupling spun up grinding down the set screw against the harder Inconel shaft.
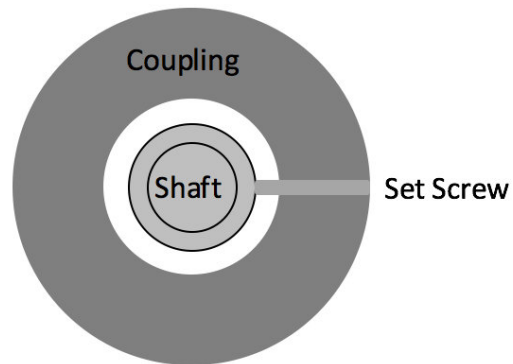


**Figure 42. Standard Lovejoy Coupling Arrangement**

The failure of the set screw led to a modification of the wave rotor's shaft. Two different solutions were considered. The first was to grind a small flat spot on the

95

shaft, as shown to the left in Figure 43, and torque the set screw onto the flat to take advantage of the greater surface area. This solution has a couple of difficulties though. First, the false center on the shaft limited how large this flat area could be. The second issue was the flat could potentially unbalance the rotor and cause more problems at speed. The other solution was to drill through the shaft and have a set screw go all the way through, as shown on the right in Figure 43, and take advantage of more contact area to distribute the force over the entire set screw. These setups would change the failure mode of the set screw from grinding down in the original configuration to a shearing type failure.
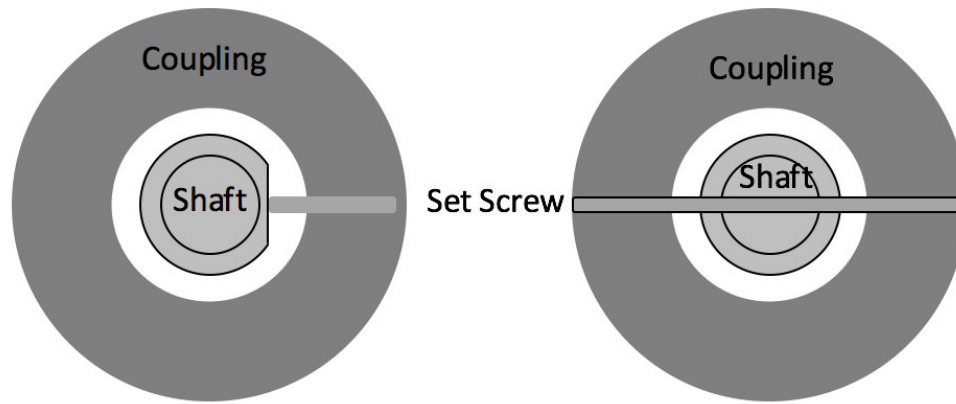


**Figure 43. Flat Surface Modification (left), Drilled Modification (right)**

In both of these modifications, a different set screw would be used. Changing the set screw to a harder metal allowed the set screw to survive a greater amount of forced applied to it. Additionally, a harder metal would be less susceptible to the grinding failure seen in the first spin test. Due to the difficulty in aligning the coupling to a small drilled hole, the flat portion was added to the shaft. A second flat surface was added directly opposite for balance purposes. In addition to using a flat surface, DuPont Multi Use Lubricant with Teflon was also sprayed to reduce the static friction between the rotor and the air bearing. The lubricant had to be reapplied immediately before testing began as it evaporated fairly quickly.

96

Subsequent tests using the flat surface modification would occasionally have a skipping where there would be enough jostling of the shaft within the coupling that the set screw would skip to the other flat. This was mitigated by modifying the coupling to use a second set screw 180° off and can be seen in Figure 44. Note the gap between the coupling and the shaft remains exaggerated.
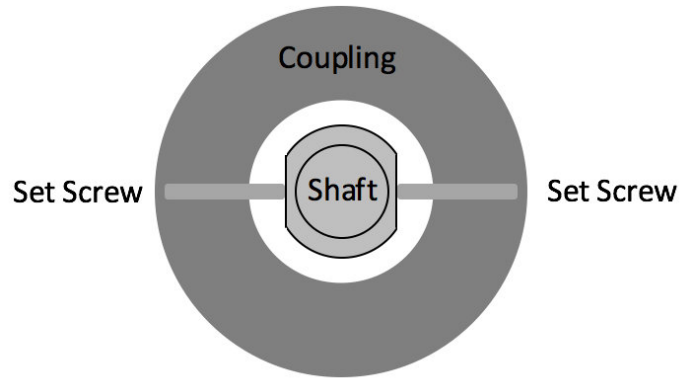


**Figure 44. Final Shaft Coupling Configuration**

The wave rotor's electric drive motor was controlled by a Phoenix Edge 100 ESC, though a Phoenix Edge 200 ESC was purchased as it doubled the maximum continuous current available. Because the wave rotor continuously looked to draw so much power, the combustor characterization setup was attached to the TI port as a connection between the TI port and the supply system's 2" (50.8 mm) pipe output. This enabled air to be pumped into the system thus lowering the power required to spin the rotor. The power decreased because the endwall ports and rotor passages were designed such that the air would push the rotor in the desired rotational direction. In addition to the small electric motor, an old turbine drive motor had become available and was also considered for use in order to test the low speed off design points as it was limited to 30,000 RPM. This testing in ongoing.

97

## 3.9 Conclusion

This chapter has described the setup for both the computational and experimental aspects of this research. This serves as a guideline for designing a throughflow wave rotor cycle from a few a priori conditions to a completed model of a realistic cycle. With the numerous parameters from the code, the CAD design methodology of the rotor was discussed leading to the manufacture of the wave rotor and the combustor. The manufactured parts required a handful of supplemental parts such as the venturis. The data acquisition and the experimental accuracy of the anticipated measurements was detailed as well as the different setups for the various aspects of the testing program. Chapter 4 will detail the results of code usage and the experimental tests. The ongoing testing of the complete assembly can be seen in Figure 45. This figure lacks the final parts of the plumbing and does not shown all of the instrumentation but is representative of the rig.
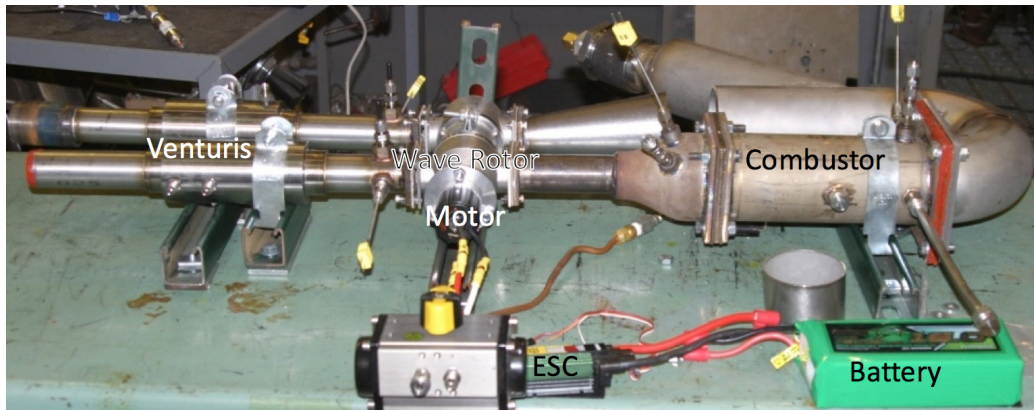


**Figure 45. Near Complete Rig**

# IV. Results and Discussion

This chapter discusses the results of the design and testing of the wave rotor and its supporting components. The first sections will entail the computational design results. Although those results were discussed sporadically within Chapter 3, they are detailed in depth here. Notably, they also include the original cycle design that attempted to generate approximately 3 kW of power. This design was changed to the 1.5 kW design point due to the high temperature required to obtain 3 kW. The 1.5 kW computational results detail both the design point and the off-design, throttled wave rotor. Following the computational results are the experimental results beginning with the combustor testing before moving to the wave rotor components. The combustor testing contains design point, off-design, and ignition results. The wave rotor results are primarily mechanical testing to look for vibrational and rotordynamic issues. They present both the ping test of the wave rotor as well as the unpressurized start up.

## 4.1 Computational Results: Design of 3 kW Wave Rotor

Although Chapter 3 revolved around building a wave rotor utilizing a total temperature ratio of about 3.0, the first iteration was a more aggressive design seeking to generate around 3 kW of power via a mass flow rate of 1.8 kg/min with a cycle temperature ratio of 4.0 and a 1.4 cycle pressure ratio.

This initial cycle was designed to completion and the code's output can be seen in Figure 46. The port conditions can be seen in Table 10. To achieve the desired temperature ratio, the required exit temperature of Port 2, TI, was greater than 1550 K. While this is not excessive when compared to high performance afterburning turbofans such as those found in modern fighter aircraft, this temperature was above the safety threshold desired within the lab and the component materials desired for

use. This temperature would have required an increased need for cooling as these temperatures were well within the melting range of Inconel and most other engine metals.

| | MF | EF | MO | UB | PB | TB | P0 | T0 | ALPH |
|---|---|---|---|---|---|---|---|---|---|
| 1 | 0.399 | 0.396 | 0.766 | 0.533 | 0.821 | 0.950 | 1.000 | 1.000 | -0.002 |
| | | | | 0.494 | 0.821 | 0.950 | | | |
| 2 | 0.603 | 3.243 | 2.886 | 1.043 | 3.195 | 5.195 | 3.670 | 5.384 | -0.004 |
| | | | | 1.024 | 3.194 | 5.194 | | | |
| 3 | 0.000 | 0.000 | 0.000 | 0.000 | 0.000 | 0.000 | 0.000 | 0.000 | 0.000 |
| | | | | 0.000 | 0.000 | 0.000 | | | |
| 4 | 0.399 | 1.614 | 1.408 | 1.231 | 1.090 | 3.785 | 1.415 | 4.049 | -0.001 |
| | | | | 1.214 | 1.090 | 3.785 | | | |
| 5 | 0.603 | 2.038 | 2.414 | 0.773 | 3.705 | 3.284 | 4.181 | 3.388 | -0.007 |
| | | | | 0.748 | 3.703 | 3.283 | | | |
| 6 | 0.000 | 0.000 | 0.000 | 0.000 | 0.000 | 0.000 | 0.000 | 0.000 | 0.000 |
| | | | | 0.000 | 0.000 | 0.000 | | | |

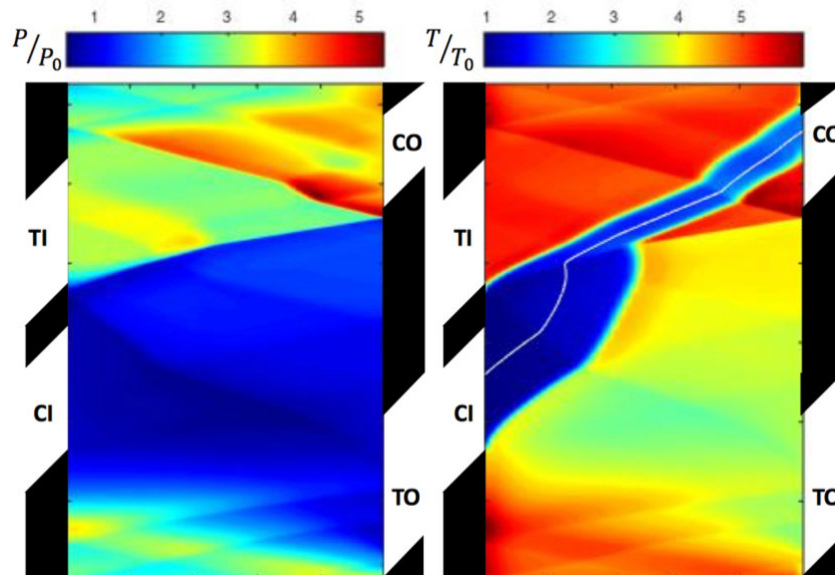Figure 46. 3 kW Power Wave Rotor Design



Figure 47. Cycle Temperature of Four x-t Diagram

Despite the difficulty in building the supporting components for this cycle, this cycle was expected to perform well. The rotor and endwalls would have have been able to withstand the temperatures and stresses this cycle would have presented.

100

Table 10. Port Conditions for Temperature Ratio 4

| CO Total Pressure | 423.6 kPa | TO Total Pressure | 143.4 kPa |
|---|---|---|---|
| CO Total Temperature | 979 K | TO Total Temperature | 1170 K |
| TI Total Pressure | 371.9 kPa | Main Mass Flow | 1.488 kg/min |
| TI Total Temperature | 1555 K | Burner Mass Flow | 2.249 kg/min |
| Power Available | 2.79 kW | Mass Flow Ratio | 1.511 |

One of the big pros to this cycle was the design point lacked the tiny amount of mass flow exiting through TO without undergoing the burner loop. The bottom right corner of Figure 47 lacks any of the blue coloring indicative of this phenomenon. The various port conditions for this cycle can be seen in Table 10. The problem, as previously said, was the combustor temperature. Not only would this temperature have caused cooling problems for the burner itself, the reducer back to the rotor and the components holding the the combustor physically in place would have been susceptible to higher temperatures as well. That does not broach the sealing issues either which would have presented greater difficulties, especially in finding gasket material.

## 4.2 Computational Results: Design of 1.5 kW Wave Rotor

Following the decision to reduce both the power, 1.5 kW, and the temperature ratio, 3.0, targets, a new cycle was designed to completion. This cycle was used to design and build the hardware for the experimental tests. Notable changes from the 3 kW cycle to this cycle other than the obvious decrease in power was the decrease in TI temperature from 1555 K to 1233 K and the decrease in rotor length by about 17%.

Table 11 lists various conditions of the design point such as the mass flows, pressures, and temperatures. The CI inlet conditions are considered to be sea level, static. As this is partially a comparison to a gas turbine engine, the correspond-

101

ing OPR would be 3.8 with a $T_{41}$ of 1235 K. Although not entirely the same, the EGR present functions similarly to how it would in a piston engine. It boosts the pre-combustion temperature assisting combustion efficiency.

Table 11.  Design Point Operation Values

| CO Total Pressure | 384.1 kPa | TO Total Pressure | 133.2 kPa |
|---|---|---|---|
| CO Total Temperature | 786 K | TO Total Temperature | 885 K |
| TI Total Pressure | 341.9 kPa | Main Mass Flow | 1.591 kg/min |
| TI Total Temperature | 1233 K | Burner Mass Flow | 2.120 kg/min |
| Power Available | 1.79 kW | Mass Flow Ratio | 1.332 |

Comparing the two cycles, it is arguable that the 2.79 kW cycle is superior to the manufactured cycle as it was predicted to generate approximately 1.56 times (2.79 kW vs 1.79 kW) the power using only 0.93 times the mass flow rate (1.51 kg/min vs 1.59 kg/min). That design utilized a rotor with the same diameter of 41.9 mm but a greater length of 76.2 mm compared to the 1.79 kW rotor. Despite these unfavorable comparisons, the 1.79 kW rotor met safety requirements and was eventually built and tested.

### 4.2.1   Design Point.

The x-t diagram shown in Figure 48 is the computational visualization of the wave rotor's design point. The expected EGR, as discussed in Section 2.3, is present entering the CO port on the temperature diagram, the streamline undergoes the strongest inflection following the hammer shock. This hammer shock was generated by the opening of the TI port. Lastly, a slight amount of fresh air exits through the TO port without undergoing combustion. On the surface, everything appears normal; i.e. the cycle correlates well with literature. Note that the coloration of the x-t diagrams is such that the pressure and temperature ratios were normalized by the CI conditions with both equal to 1.0.
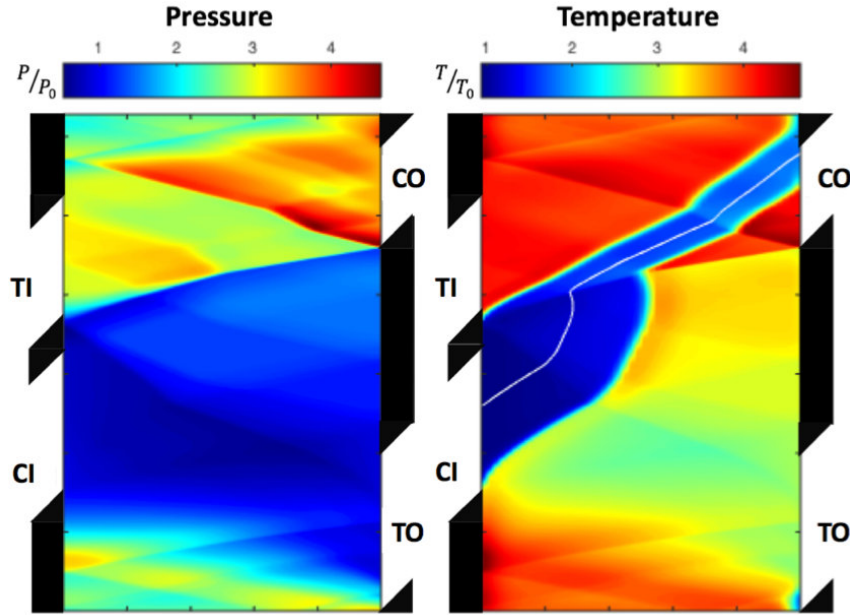
102

**Figure 48. Wave Rotor Design Point**

Though the streamline, progressing from CI to CO, undergoes the most significant inflection due to the hammer shock, it undergoes a further shift from the wave caused by CO opening. Despite all of the inflections, the streamline stays centered within the cold flow. This is significant because of its location at CO. It is not centered within the exiting port and shows that while a majority of the newly compressed flow exits through CO, some escapes to exit through TO. Note that although this air is unburnt, it still undergoes some heating and the pressurization from the energy exchange. Therefore, it is still able to contribute positively within the exhaust stream from TO. The only difference is that it does not go through the burner loop to assist the next cycle's energy exchange. The key effect here, however, is the system's indifference to this since the amount of unburnt flow is a small fraction of the total exit flow through TO and will mix out before downstream features encounter it.

In addition to viewing the x-t diagram, a property sweep can be accomplished at the ports in order to show the variation quantitatively. This can be done within the

103

MATLAB script and plotting the x-t diagrams points that are within the open ports. Each condition was plotted separately with the x-axis being a percentage of the port's circumferential location; 0 is the port opening and 100 is the port closing. While this makes all four ports appear the same size, this is not true and was only done for simplicity in data presentation. The first of these profiles, in Figure 49, depicts the static pressure profiles of each port. For all of these figures, the solid line is the CI port, the dashed line is the CO port, the line with dots and dashes is TI, and TO is the dotted line. Figure 50 presents the static temperature profiles. Note that these figures utilize dimensional values on the y-axes as they have been referenced to the ambient reference conditions.
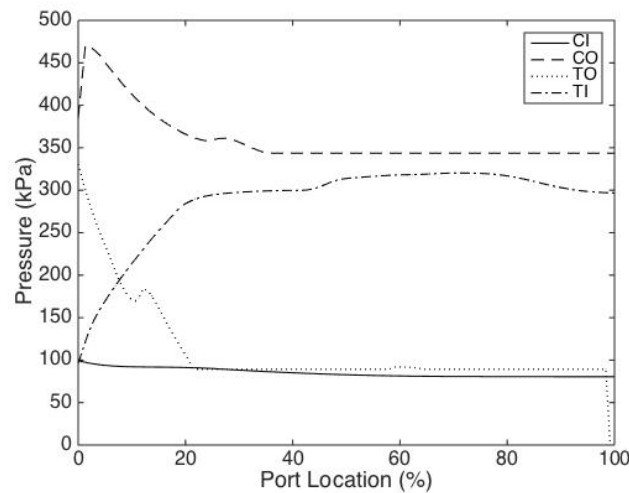


**Figure 49. Static Pressure Profile at Each Port**

104
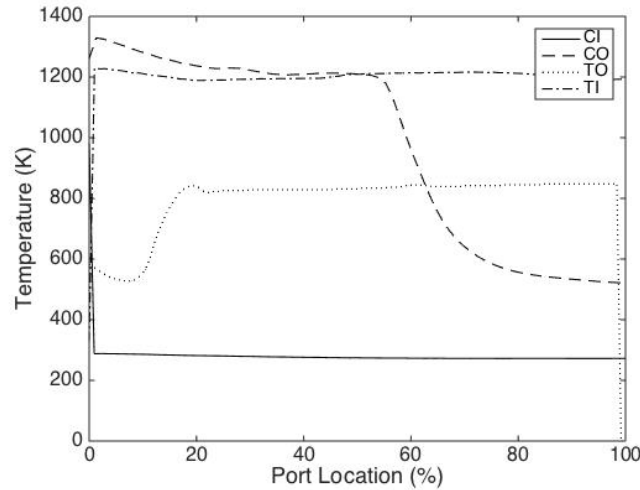
**Figure 50. Static Temperature Profile at Each Port**

Although the previous x-t diagrams have depicted static pressure and temperature and those in Section 4.2.2 will as well, x-t diagrams can also display other properties. Figure 51 depicts the density and velocity contours present during a cycle. Note the density is normalized by the ambient density and while velocity is normalized, the exact normalization was unclear within the code. While this made quantitative conclusions difficult, it still provided trends and flow magnitude. Figures 52 and 53 depict the density and velocity profiles at each port.

The density diagram primarily illustrates the compression the CI air undergoes. If the temperature and density diagrams are looked at together, the large density increase shown corresponds to the compression of the cold air which subsequently exited through CO. This dramatic increase in density also explains why the pressure and temperature diagrams appear to have a relatively even split between fresh flow and EGR at CO. The fresh flow is more than twice as dense; and, therefore, more than 50% of the total flow rate. The most important takeaway from the velocity diagram is the indications of flow reversal generated by the TO expansion fan as well as a small amount after the strong shock caused by TI's opening.
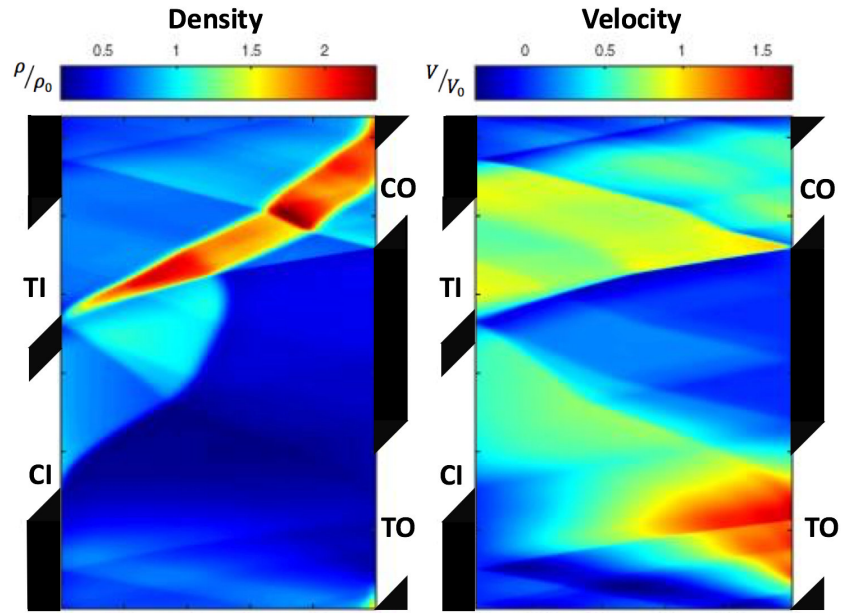
105

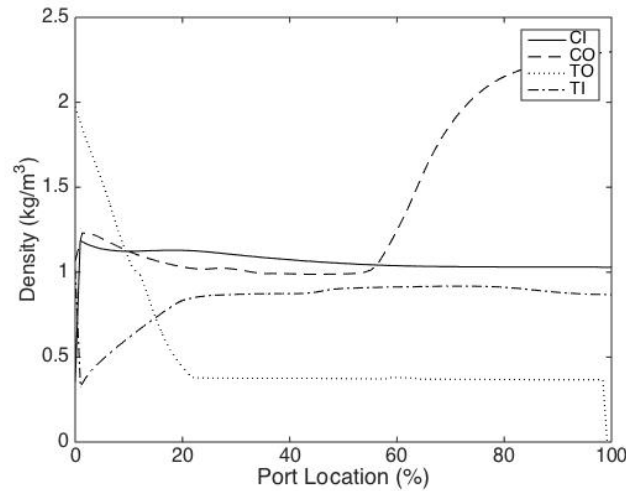**Figure 51. Wave Rotor Design Point Density and Velocity**
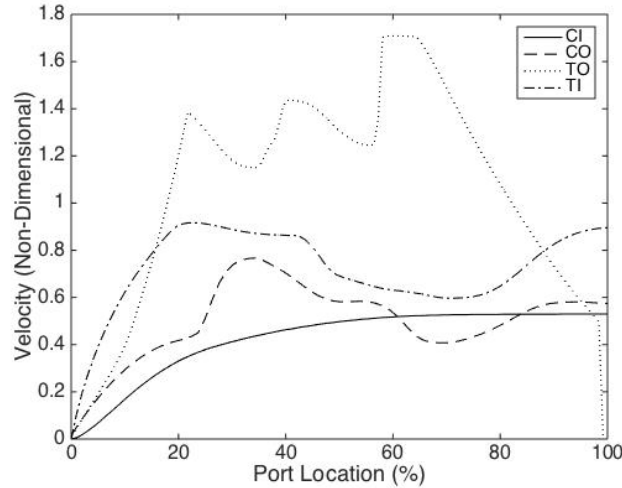


**Figure 52. Density Profile at Each Port**

Figure 54 presents the stagnation pressures and temperatures, while Figures 55 and 56 show the profiles for that stagnation pressure and temperature respectively. Note that the reference for these values was the ambient stagnation pressure and temperature, which in this case was equal to the static pressure and temperature.

106

**Figure 53. Non-dimensional Velocity Profile at Each Port**

Note that the reference for all of the conditions are the ambient, static conditions present prior to CI as all values are a ratio of CI. These two diagrams are useful for understanding how much energy is in the flow at each port as well as where the energy exchange mechanisms are occurring. The stagnation pressure diagram contains far higher indicated pressures between TI and CO due to the higher velocities present after the energized TI flow enters the rotor. Additionally, the power calculations utilized stagnation values; therefore, being able to see those values assists in understanding the cycle. This visual analysis is greatest at TO where the diagrams show the variation present within the port. This implies the stagnation properties the code outputs as given in Figure 13 are weighted averages, not point values. The weighting used for the average has yet to be replicated with the port sweeps and, therefore, their averages are not given.
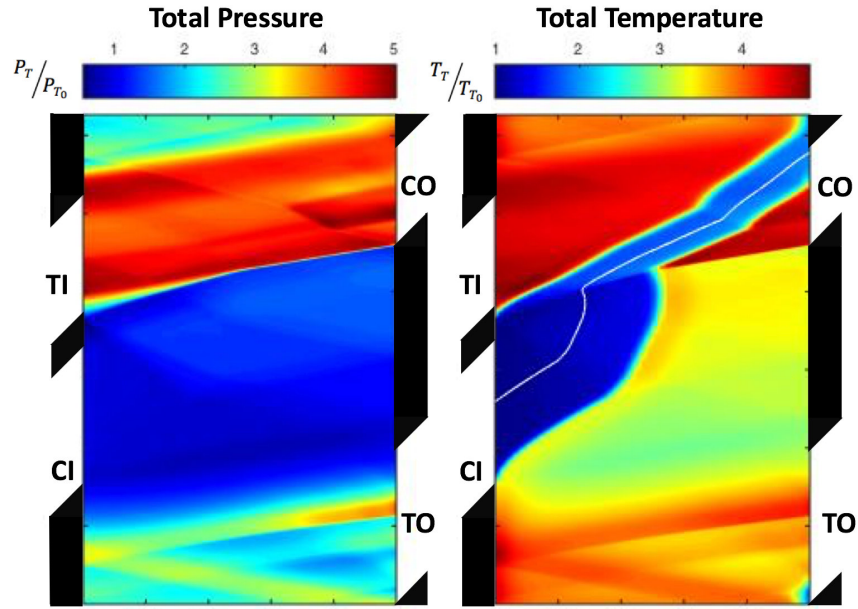
**Figure 54. Wave Rotor Design Point Stagnation Values**
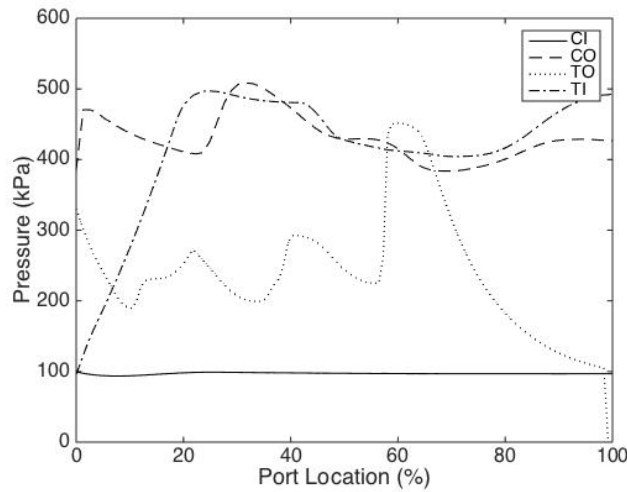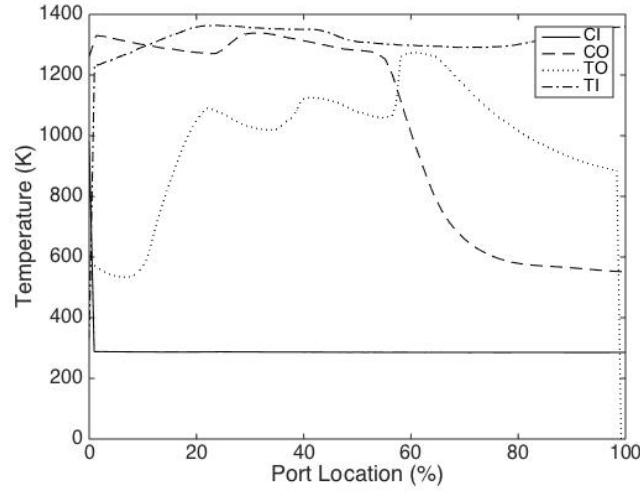


**Figure 55. Total Pressure Profile at Each Port**

The goal of this project was to design and build a wave rotor engine capable of producing 1.5 kW of power. The equations to calculate this were given in Section 3.1 Equations 5-10. Expanding the exit conditions listed above to ambient yields 1.79 kW of power. Table 12 lists the values from the equations necessary to calculate

**Figure 56. Total Temperature Profile at Each Port**

the power from the exhaust (TO) pressure, temperature, and mass flow. The design point does generate enough power to meet the design goals although it is important to note that this is the computational case.

**Table 12. Design Point Power Calculation values**

| Mach | 0.649 | Static Temperature | 824.5 K |
|---|---|---|---|
| Sonic Velocity | 565 m/s | Exit Velocity | 367 m/s |
| Power | 1787 W | | |

### 4.2.2 Off-Design Throttling.

As previously discussed, one of the hallmarks of gas turbine engines is their ability to throttle and operate at a variety of off-design values. This is done changing the fuel flow into the combustor which changes the $T_{41}$. The change in $T_{41}$ affects the available energy within the flow and thus alters the rotor speed of the turbine. The turbine is directly coupled to the compressor and therefore changing the turbine speed changes the compressor speed. Typically gas turbine operating lines appear on compressor maps where corrected RPM speed lines intersect with efficiency islands in

109

order to achieve the best performance for a given engine speed [7]. In order to ensure the wave rotor was able to operate over a similar range to a comparable small gas turbine, several off-design points were simulated to examine its operability range.

The direct method increased the rotor speed and heat addition term together and quickly revealed a relatively linear relationship. It is acknowledged that heat addition and rotor speed were independently changed and therefore any sort of relationship could be developed; however, the linear claim is made based on the performance at each point. Simple changes to heat addition without corresponding rotor speed changes resulted in increased wave mistiming and degraded cycle performance. The best performance at each speed point occurred when both the rotor speed and heat addition followed the linear trend. Best here defines the performance in terms of TO conditions, stagnation pressure and temperature, as well as reasonable EGR levels. It is also acknowledged that modulating QCORR, heat addition, and matching rotor speed would have been the preferred method to compare to a gas turbine.

The lower RPM limit was found to be 70% of the design RPM (26,950 RPM). The Q1D code was unable to converge upon a solution at a lower speed. As can be seen in the left set of x-t diagrams in Figure 57, this low of a value caused significant operating issues as this case had a lower burner loop mass flow compared to the main loop. Attempting to operate experimentally at this point would likely cause combustor stability problems. The 75% RPM case is shown in the right set of x-t diagrams. Note that all of the off-design x-t diagram colorbars have been set such that they have the same range as the design point. Similarly scaled results for all cases can be seen in Appendix D.

While examining the figure, the issues with the 70% case are readily apparent as a far greater percentage of the unburnt flow does not exit through CO to the combustor; the arrows in the bottom right of the temperature diagrams in Figures 57
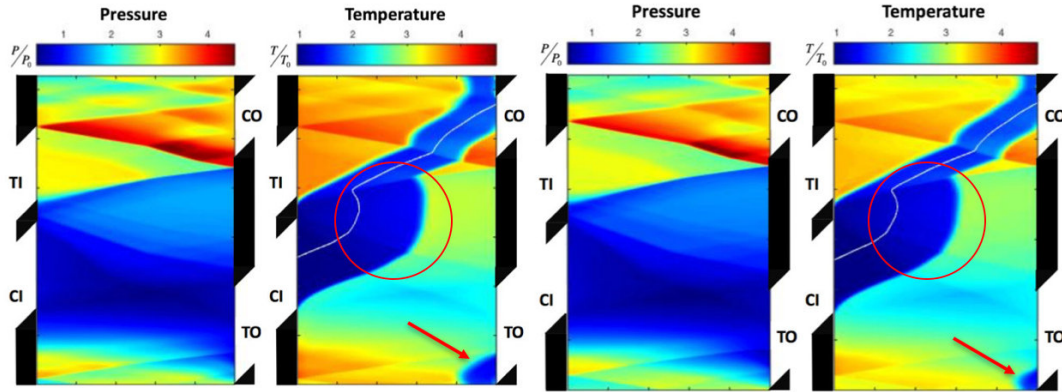
110

**Figure 57. 70% Design Speed Case (left), 75% Design Speed Case (right)**

and 58. Also note the streamline undergoing a much longer, curved path characterized by larger inflections especially from the compression waves caused by CO and TI's opening as compared to the design point in Figure 48. These cases demonstrate the weakness of the pressure waves and how, despite the relatively close timing, there are still some spurious and/or mistimed waves. The other obvious feature is the larger size of the cold regions as well as their roundness when compared to the design point. The inflections and the larger cool area are circled in the images.

At this point, it should be remembered that these are traveling pressure waves, not standing waves such as those seen in aircraft aerodynamics. Also, the usage of weaker and stronger waves here is relative to the corresponding pressure wave at a different speed point not compared to itself. The strongest wave in each figure is the compression shock generated by CO's opening, but at the lower speeds, this is weaker than it is at higher speeds.

The upper limit to the speed range, as shown in Figure 58, is 130% of the design RPM. Above this speed the temperature of the TI port exceeds the operational limit. Both of these cases have TI temperatures above 1545 K beyond the functional range for this investigation. The inflections of the streamlines are much sharper indicating the far greater strength of the pressure waves. A stronger pressure wave indicates

111

greater compression. Greater compression contributes to either better combustion efficiency (when exiting through CO) or more power within the exhaust (when exiting through TO). The size and shape of the cold area also agrees with the increased compression. The already small amount of unburnt air has decreased to essentially zero and any that does exist undergoes far greater heating compared to the design point.
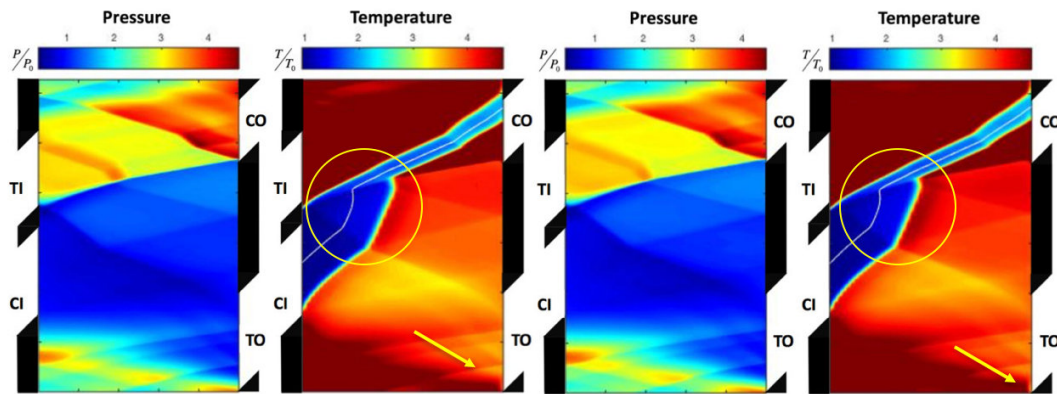


**Figure 58. 125% Design Speed Case (left), 130% Design Speed Case (right)**

Although the speed limits help to understand the cycle, the important parts are the less extreme points where real operation could be possible. Figure 59 shows the stagnation conditions at each port except CI as well as the cycle mass flow. CI was not shown because it is always ambient and thus unchanging. The cycle mass flow is the mass flow through CI and TO whereas the burner mass flow is the flow through CO and TI which includes the EGR. It presents all of this data normalized by the design point. This data is colored such that red lines are temperatures, blue lines are pressures, and the primary cycle mass flow is the black line. The TO conditions are solid lines, the CO conditions are the dots, and the TI conditions are the short dashed lines.

Examining the figure reveals that near the outer limits discussed above the functions become nonlinear. However, the range from 80% to 120% was nearly linear
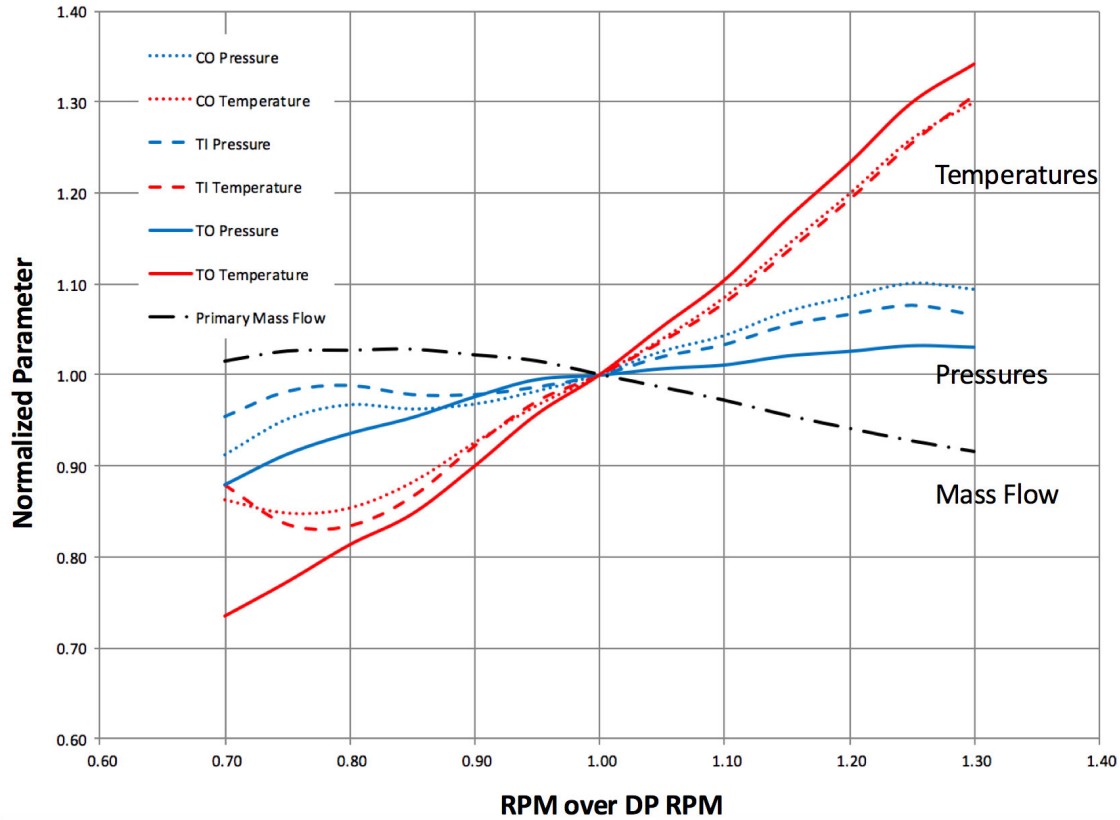
112

**Figure 59. Throttled Port Conditions and Mass Flows**

for all variables. Therefore this was selected as the experimental test range. As expected, the temperature ratios all increase with a similar slope and CO and TI are near identical. The near even slopes for CO and TI were expected due to their coupling through the combustor. This relationship is somewhat transcendental as a higher CO temperature and a given fuel flow rate will cause a proportional rise in TI temperature. Concurrently, the higher TI temperature causes more thermal energy to be transferred during the energy exchange that drives the cycle. Note that while this explanation discusses a given fuel flow rate, an increase in fuel flow rate would be needed to cause these changes once the cycle reaches thermal equilibrium. Increasing TI, thus the energy exchange, causes an increase in CO. The different slope of the TO temperature was also expected as the flow will undergo an expansion cycle, which

113

changes the pressure nonlinearly, making it more reactive to the changes in speed and combustor temperature.

An increase in pressure for all ports was also expected because the temperature rises while mass and volume are staying relatively constant. Similar to the temperature changes, the pressure of CO and TI closely follow each other. Opposite of the TO temperature, TO's pressure was more static compared to CO and TI. The slopes' variance from linearity can also be explained by the impact of rotor speed on the wave timing and strength as these results varied both rotor speed and QCORR. A simple speed change not coupled to an enthalpy change in the from of QCORR would result in horribly mistimed waves. These simulations were inferior to their counterparts with QCORR and rotor speed changes. Extrapolating these results to the intended experiment means varying the fuel flow rate and thus causing further changes in total mass flow rate are unaccounted for by the code. The pressure changes were also believed to have an effect on the nature of the mass flow rate changes.

The overall mass flow rate changes were more unexpected. The cycle (CI and TO) mass flow rate decreases by 8.4% with higher speed and increases by 2.8% at lower speed despite correlating to increased power at high speeds and decreased power at low speeds. This is counterintuitive to typical Brayton cycles as an increase in compressor speed will draw in more mass flow than a lower speed. Initially, it was believed the lessened mass flow is likely due to the shorter opening time of the port limiting the amount of ambient air that can enter. This explanation was rendered moot simply because the flow rates are per unit time and the port area is unchanging with an average of three open ports at any given time. The mass flow changes were likely caused by the change in TO pressure. The greater pressures present at higher speeds likely caused the local pressure within the channel to be higher then at the design point just prior to CI opening. Higher channel pressure resulted in a lower

114

mass flow intake and thus a lower mass flow rate.

An increase in the burner to cycle mass flow ratio (not plotted) physically means that the amount of recirculated air through the burner loop is increasing relative to the primary flow rate. This is a very important consideration as the recirculated air is vitiated and thus could lead to combustion stability issues. Although this was not an issue for this experiment given the lean equivalence ratios, it could cause dramatic effects for richer mixtures.

Although mass flow has a proportional relationship with power in the exhaust, the higher speeds have greater power available. This was caused by the increases to both temperature and pressure. The higher stagnation conditions resulted in greater increases to specific kinetic energy thus driving up power available.

In order to further illustrate the changes in operation as the rotor speed changes, the 80%, design point, and 120% cases were further examined. The x-t diagrams for pressure have less noticeable changes, as shown in Figure 60, but the temperature diagrams in Figure 61 are immediately visible. Rather than scaling the output by the design point, they have been based on the 120% range. The only easily noticeable change on the pressure diagrams is the weaker pressure wave reflecting back towards the TI port from the CO port. This is likely due to a mistimed wave impact on the end wall. Although the lower speed cases have higher pressures towards the inlet wall, the 120% speed case has the highest pressure along CO. Looking at the figures more closely however reveals a few subtle, yet important differences. The first is impact location of the reflected shock caused by CO's opening. This shock's location is important because this reflection's locations affects how the cycle will push the the air out of TO.

A stronger "push" out of TO will affect the outlet pressure and thus the available work in the exhaust stream. The other feature of interest is the triangle in the middle

115

of each diagram. This is framed by the two dotted gray lines and the relative heights are illustrated with a solid black line. The higher the speed, the smaller the angle off the inlet wall. The strength of the shocks within the channels can also be inferred by this illustration as each of the black lines is inline with the third tick mark along the horizontal axis. The greater area, thus longer black line, was caused by mistimed waves. This creates spurious waves affecting the compression strength of this area. Although the high speed case has the smallest area, this is simply due to the overall higher pressures present within the channels as well as somewhat coincidental "good" timing. The blue area reaches a higher position relative to the y-axis at the higher speeds. This is indicative of the timing of TI's opening shock and where it reaches the CO port to force the air into the burner loop.
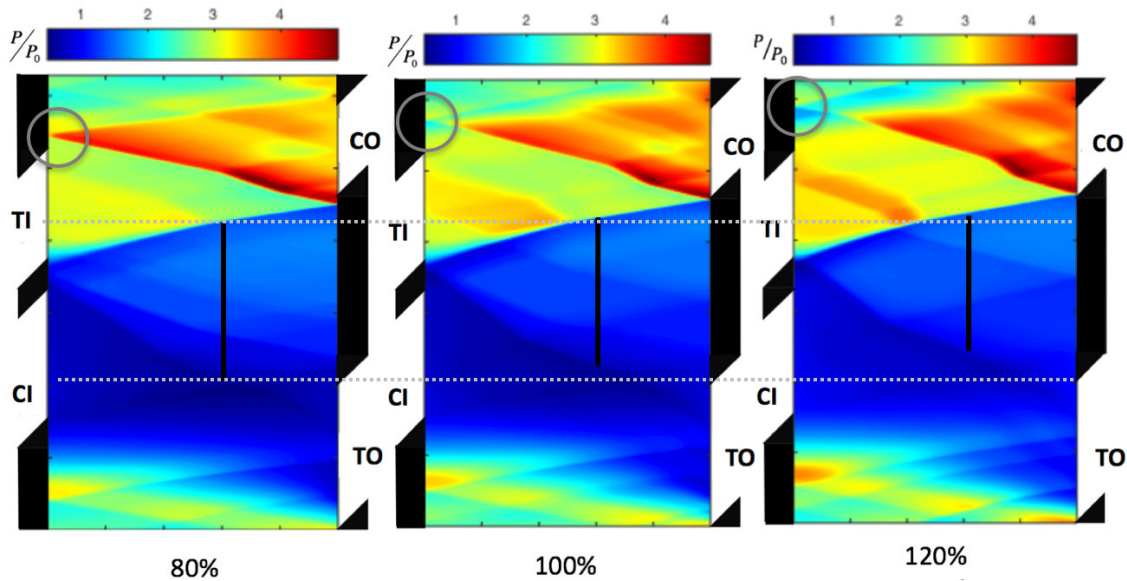


**Figure 60. Pressure x-t diagrams for Various Speeds**

The temperatures, however, vary far more with rotor speed as shown on Figures 59 and 61. The lower speeds have lower temperatures throughout and, when scaled according to the 120% case, the 80% case's shockwave lines are difficult to see above the TI port. The other obvious change was the amount of fresh air exiting through

116

TO without going through the combustor loop as indicated by the black arrows in the bottom right of each case. The 120% case has no unburnt air exiting TO as opposed to the 80% case with 2-3 times the area of the design point. Other key changes are the area of the fresh air upon entering the rotor and the changing inflections of the streamlines shown within the gray circles. The fresh air at 80% and 100% is round and bulging whereas the 120% air is flatter with relatively straight boundaries. Although the inflections of the streamlines change depending on the pressure wave strength, it is important to note that the streamline is always exiting out through CO indicating more than half of the fresh mass flow is entering the combustor loop.

The final notable streamline feature was the length from the inflection of CO's opening shock to the CO port face. Identical lines at identical angles are depicted in the top right corner of each x-t diagram of Figure 61. In the 80% case, the streamline bends upwards before bending back down, while the design point is relatively linear. The 120% case's streamline is the opposite of the low speed and has a slight downward angle to it and never bends back the other direction. This is representative of the flow direction. The stronger waves present at hotter, faster cases are able to redirect more of the fresh flow out of the CO port whereas the low pressure, low speed cases want to suck the air out through the much lower pressure TO port. This sort of change will affect cycle efficiency however experimental research is necessary to determine the exact effects and trends. Note that the unscaled 80% and 120% RPM unscaled colorbar images were included within Appendix D.

There is a further implication of the changing exit temperature and mass flow. That is the potential power within the flow. While the design point generates 1.79 kW of power at 1.59 kg/min, the 80% case only produces 1.14 kW at 1.63 kg/min, and the 120% case produces 2.24 kW at 1.50 kg/min. The numbers illustrate a few different relationships. A decrease in rotor speed increases the mass flow far less than increasing
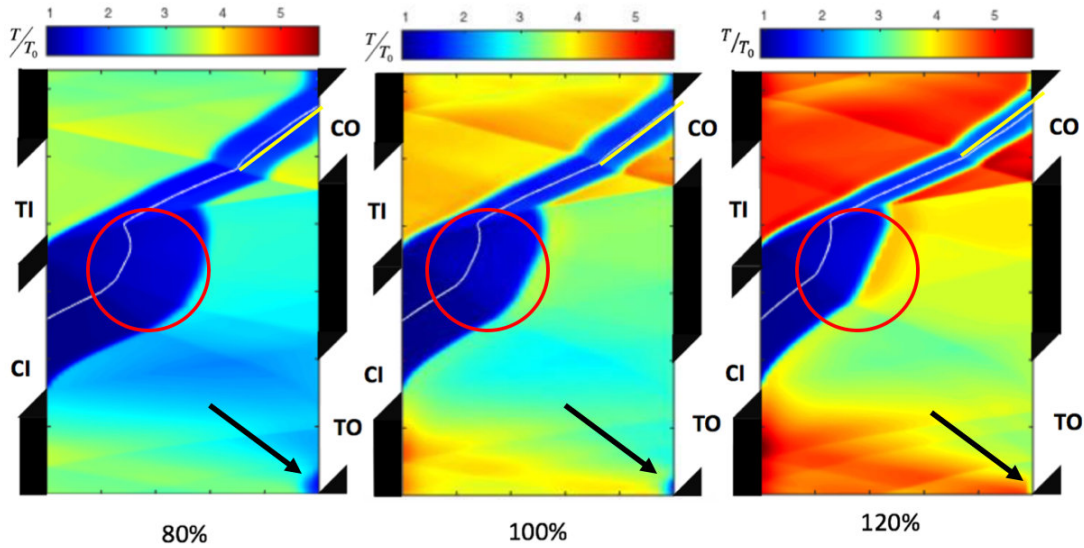
**Figure 61. Temperature x-t diagrams for Various Speeds**

the speed drops it. On average, 5% drop in speed causes a 0.01 kg/min increase whereas a 5% increase in speed causes a 0.022 kg/min decrease in mass flow. The opposite relation is true for power where decreasing the rotor speed decreases power available faster than increasing the rotor speed increases power available. Table 13 shows the power calculations for five different rotor speeds. Note that these equations used stagnation pressures as this was the output of the Q1D code whereas all of the x-t diagrams shown have displayed static conditions.

**Table 13. Selected Rotor Speeds with Available Power**

| Rotor RPM | Mach | Static Temp (K) | Sonic Velocity (m/s) | Velocity (m/s) | Power (kW) |
|---|---|---|---|---|---|
| 30,800 | 0.56 | 682 | 514 | 289 | 1.14 |
| 34,650 | 0.62 | 746 | 537 | 333 | 1.50 |
| 38,500 | 0.65 | 825 | 565 | 367 | 1.79 |
| 42,350 | 0.66 | 908 | 593 | 393 | 1.99 |
| 46,200 | 0.68 | 1010 | 625 | 425 | 2.26 |

As explained previously, Table 13 shows that power decreases with low speed

118

operation faster than it increases at higher speeds. Examining the intermediate values, the power available is closely related to the Mach number as calculated in Equation 5. The only variable that changes in the Mach equation is $P_{TO}$. Figure 59 shows that TO pressure only increases by about 3% (to 137.4 kPa) for a 30% RPM increase as opposed to a 30% RPM decrease yielding a TO pressure more than 12% lower (117.2 kPa) than the design point (133.3 kPa). All pressures, temperatures, and mass flow relations for the 70%-130% range are listed in Appendix E.

## 4.3   Combustor Characterization

The combustor testing was the first major series of testing for the research. The supply air flow was set to 2.12 kg/min and passed through the T-63 prior to entering the wave rotor combustor, as shown previously in Figure 40. The T-63 brought the air up to temperature via lean hydrogen combustion. The first time the combustor hardware was heated functioned as a hot air, pressure check. As the inlet temperature rose, the entire combustor rig heat soaked and an abundance of outgassing was visible. This was especially true around the flanges. While some of the visible vapor can be attributed to oils and other substances such as anti-seize, a majority of the outgassing was assumed to be the gaskets and RTV. After the first heating, the burner was visually inspected with no signs of leakage observed and nothing loose.

### 4.3.1   Ignition.

Ignition of the wave rotor's combustor was attempted as the inlet temperature rose. The first ignition attempts began at 450 K and while the mixture ignited, it was unable to sustain ignition indefinitely and would not reliably maintain a flame. Note that this testing saw a slow inlet temperature rise such that each ignition attempt would only see a few degree rise in temperature. However, when the wave rotor

119

is feeding the combustor, the inlet temperature will rise quickly jumping tens or hundreds of degrees in seconds. A stable, undoped ethylene flame could not be maintained until an inlet temperature of 560 K was reached. At this inlet condition 0.055 kg/min of ethylene was used, equating to an equivalence ratio of 0.38, to sustain a combustor exit temperature of 1116 K. Multiple equivalence ratios were not tested at each case due to the slow but steady temperature rise. For example, if the attempt was begun at 560 K, by the time the flame steadied out at the exit, the inlet would have increased by 5-7 K. This would have made the next equivalence ratio at a higher inlet temperature. A full sweep would have seen the inlet temperature rise to beyond the next case. Therefore, it was decided to search for the minimum equivalence ratio needed to ignite. Maintaining the inlet temperature at every point would have dramatically increased the test time and in order to maximize time efficiency, a $\phi$ sweep was done at the design point's inlet temperature.

Table 14 lists the inlet temperatures and stability results as well as the flow rates and exit temperatures. It is important to remember that this test was not trying to achieve a specific exit temperature or an equivalence ratio, rather it was looking for the minimum flow rate necessary to light and whether or not that produced a stable flame. Note that hydrogen doping was not examined during ignition because the temperature rose to the safety limits in a matter of seconds and the only active control was on or off. One of the key points from the ignition testing was the discovery that the ignitor did not require a separate air supply. This eliminated all ignitor air usage in subsequent testing.

120

**Table 14. Ignition Study Parameters**

| Inlet Temp (K) | Ethylene Flow Rate (kg/min) | Equivalence Ratio | Exit Temp (K) | Stable |
|---|---|---|---|---|
| 449 | 0.064 | 0.440 | 1155 | N |
| 478 | 0.064 | 0.440 | 1155 | N |
| 505 | 0.059 | 0.409 | 1144 | N |
| 533 | 0.055 | 0.384 | 1116 | N |
| 561 | 0.055 | 0.384 | 1116 | Y |
| 589 | 0.054 | 0.377 | 1133 | Y |
| 616 | 0.054 | 0.377 | 1144 | Y |
| 644 | 0.054 | 0.377 | 1150 | Y |
| 672 | 0.054 | 0.377 | 1156 | Y |
| 700 | 0.050 | 0.346 | 1166 | Y |
| 728 | 0.050 | 0.346 | 1166 | Y |
| 755 | 0.050 | 0.346 | 1166 | Y |
| 783 | 0.050 | 0.346 | 1166 | Y |

While stability took some time, ignition itself was an extremely fast phenomenon. The combustor's ignition would happen near instantly after the valve fully opened and hydrogen entered the can, remembering that the procedure entailed powering the ignitor then flowing the hydrogen. This was observable while watching the thermocouple readouts as the downstream temperature quickly rose from the slightly below the inlet air temperature to the temperature corresponding to fuel flow rate's heat release, well over 1100 K in all cases. In addition to the visual readout, the sound changed to a significantly higher pitch. Both of these were signs to turn off the ignitor voltage supply and, more importantly, close the hydrogen valve, as this would cause a temperature rise beyond the safety limits. After a couple of seconds of operation, visible changes to the external components occurred, particularly at the downstream reducer as shown in Figure 62. Note that more complete operation procedures are within Appendix C.

**Figure 62. Combustor Operating near 1200 K**

### 4.3.2 Combustor Design Point.

Upon reaching the design point inlet conditions, 785 K and 384 kPa, the burner was ignited. This concluded the ignition testing and immediately became the design point testing. Although the inlet condition was near the auto-ignition temperature of ethylene, this ignition still required hydrogen doping. As this was concurrent with the ignition testing, the burner was lit at a slightly lean equivalence ratio of about 0.35 using a ethylene flow rate of 0.050 kg/min; this had an exit temperature of 1166 K. The fuel flow rate was increased to match the design point's TI temperature of 1233 K. Due to the dome loader control limitations, the exact design point temperature was not achieved. An equivalence ratio of 0.39, however, correlated to an outlet temperature of about 1225 K, less than 1% (8 K) off from the desired temperature.

Upon reaching this exit temperature, the burner was allowed to run for about 10 seconds to ensure there were no stability issues. This case was not run longer in order to limit any fatigue on the metal, especially the weld. This was a concern as the exit was cantilevered instead of being supported by the flange leading to the TI ports on

122

the inlet wall. Similar to Figure 62, the reducer on the outlet glowed very brightly with a light pinkish color. While the burner was running, the upstream temperature did not see any relevant temperature increase that might have indicated flow path problems. Although the test lacked an external thermocouple monitoring the metal temperature, the exit flow temperature was unchanging as was the color of the downstream components. After about 10 seconds, it was concluded that the burner would run in a steady manner without issues. Note this is not thermal equilibrium but was sufficiently long enough to ensure that any residual hydrogen effects had fully dissipated. A post run analysis of the burner showed that none of the components had any serious detrimental effects from the combustor checkout, notably, the reducer remained completely straight with no signs of bending despite operating at greater than 1270 K further discussed in Sections 4.3.3 and 4.3.4.

Finalizing the design point analysis was calculating the combustor efficiency as well as the pressure loss. The pressure loss calculation was quite simple being outlet pressure divided by inlet pressure. This was found to be about 94%. Given that this was designed to have 5% pressure drop, this was good. The combustor efficiency was more complicated and can be calculated as shown previously in Equation 4 using emissions or as shown in Equation 25. Note the specific heat used at the TI port was a weighted average based on the specific heats of the combustion products plus oxygen given the less than stoichiometric equivalence ratio.

$$\eta_b = \frac{(\dot{m}_f + \dot{m}_{air})C_{p_{avg}}T_{t_{TI}} - \dot{m}_{air}C_{p_{CO}}T_{t_{CO}}}{\dot{m}_f * LHV_f} \tag{25}$$

The burner efficiency left much to be desired as it was calculated to be 66.6%. The low efficiency could be related to a number of issues. There was no insulation anywhere after the burner inlet and thus heat transfer out of the system could be a part of this; however, it cannot account for all of it. A more likely explanation would be

123

mixing issues causing a large amount of unburnt fuel to exit without combusting. Further testing will be done in order to resolve the exact issue in order to improve the efficiency to a more reasonable 90% or greater.

### 4.3.3 Combustor Operational Range.

In addition to examining the design point, the combustor's operational range was examined to create an operating map for use in throttling the wave rotor. The low flow rate testing began at the wave rotor flow rate of approximately 1.59 kg/min. Although at the higher flow rates unstable ignition could be achieved at 450 K, at the lower flow rates no ignition was possible until 561 K. During the testing the air flow rate gradually crept down to 1.54 kg/min. Note that the air flow creep was an unseen error until data analysis and the combustor had already been dismantled for inspection and immediate reassembly to place the combustor inline with the wave rotor, therefore the testing was not redone as the small change was considered negligible. With an ethylene flow rate of 0.045 kg/min, an outlet temperature of 1150 K was sustained. At the same air flow rate, 1.54 kg/min, ethylene flow was increased to 0.050 kg/min and produced an exit temperature of 1,183 K. Increasing the inlet temperature to 594 K, 0.050 kg/min of ethylene produced an outlet temperature of 1189 K. At an inlet temperature of 641 K, further air flow creep occurred causing an air flow rate of 1.50 kg/min. This air flow rate combined with 0.050 kg/min of ethylene produced an outlet temperature of 1231 K. Figure 63 shows these points with the 0.045 kg/min point marked.

This testing demonstrated the wave rotor combustor's ability to operate at lower than anticipated flow rates. This was important to know because the computational throttling in Section 4.2.2 showed the mass flow rate changes during off design operations and previous wave rotors struggled to reach the desired flow rate. Additionally,

124

not shown in that computational data was the change in the burner loop mass flow. This lower flow rate testing proved the combustor could operate at those lower flow rates. High flow rate testing was not done as the burner loop flow increases were a fraction of the decreased burner loop flow: an increase in 0.1 kg/min versus a decrease of 0.6 kg/min.
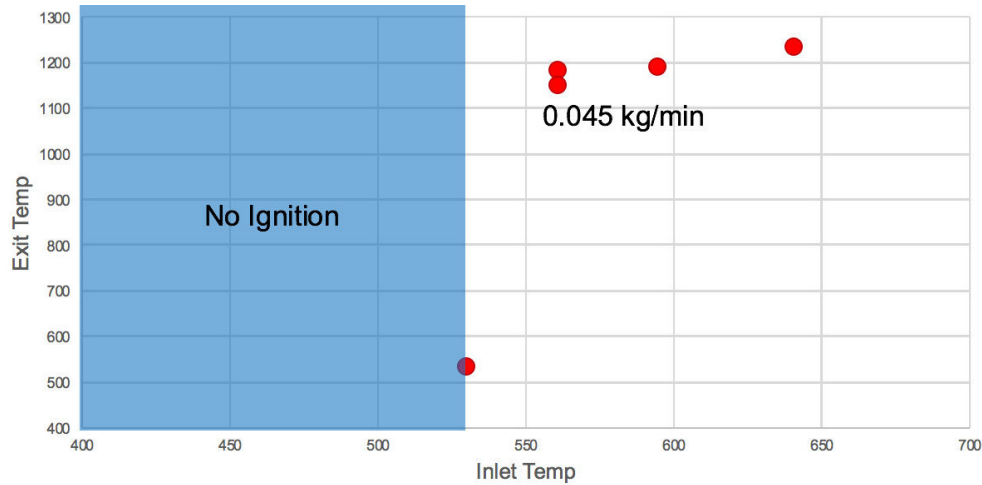


**Figure 63. Low Flow Ignition**

In addition to examining lower air mass flow rates, a $\phi$ sweep was done to fully characterize the operable conditions at the design flow rate. As previously discussed, the burner successfully ignited at an equivalence ratio of 0.35. Lowering the equivalence ratio was attempted but the flame audibly sputtered and went out. The burner was relit and the $\phi$ sweep was accomplished. The $\phi$ sweep examined equivalence ratios between 0.35 (stable flame) to 0.43 (do not exceed temperature). The do not exceed temperature was approximately 1272 K, as this was operating limit for the gaskets and was approaching the functional use temperature for the stainless steel reducer. The equivalence ratio sweep was limited by the dome loader control voltage. The power supply was capable of metering to a hundredth of a volt and greater voltage resolution would be needed for a more in-depth analysis. The results of the $\phi$ sweep can be seen in Table 15. The burner efficiency, calculated using Equation 25, is given

125

for all of these conditions as well.

Table 15. Equivalence Ratio Sweep

| Dome Loader Voltage | Fuel Flow Rate (kg/min) | Temperature (K) | $\phi$ | $\eta_b$ (%) |
|---|---|---|---|---|
| 1.51 | 0.050 | 1166 | 0.346 | 58.9 |
| 1.52 | 0.054 | 1214 | 0.377 | 65.1 |
| 1.53 | 0.056 | 1225 | 0.387 | 66.6 |
| 1.54 | 0.057 | 1241 | 0.393 | 68.6 |
| 1.55 | 0.059 | 1255 | 0.409 | 70.7 |
| 1.56 | 0.062 | 1271 | 0.428 | 73.0 |

### 4.3.4    Post Burn Hardware Inspection.

Arguably just as important as the testing itself was the inspection of the hardware afterwards. An inspection of the outer, visible surfaces revealed few issues. The reducer, Figure 64, and the backpressure plate had the sort of bluish discoloration expected of stainless steel heated to these high temperatures but nothing indicative of potential problems. The RTV on the big, upstream flange appeared to have slightly melted and the zinc plated steel bolts holding the flanges together oxidized. Despite the surface oxidation, they were still tight.

While disassembling the burner, galling was found in several places. Two of the four screws bolting the backpressure plate to the reducer were snapped off due to galling between the nuts and the ends of the screw and the coupling connecting the upstream reducer to the supply's flex line galled together. None of the Swagelok components showed any signs of galling. Beginning with the upstream reducer, significant changes in appearance were noted throughout. The stainless steel Kiel probe, the tip of the thermocouple, and the ethylene line components all changed from their previous metallic color to a tan, strawlike color as seen in Figure 65.

The injector components in Figure 65 sat with the weld flush with the rim of

126

**Figure 64. External Coloring on Reducer**



**Figure 65. Fuel Injector with Straw Coloring After Burner Testing**

swirler's center hole. This discoloration was caused by the exposure to 785+ K air flowing past it. Note that the discoloration is uniform throughout and not only on the side facing the incoming supply air. The swirler itself had no discoloration although the stainless steel screws holding the various parts of the can together, including the swirler, showed this same discoloration. The can's plenum facing surface had a variety of visible changes, as can be seen in Figure 66. Although a little difficult to see in the figure, the impact of the cooling holes and their directing ridges can be seen as there was less change and a well defined transition to internal temperature changes. The three middle segments had a large portion of their surface area turned a bluish color that can be faintly seen in Figure 66. The furthest downstream section did not contain much of the blue as seen in the previous three segments. Rather, it resembled

www.manaraa.com

the stainless steel components and had a strawlike coloring.
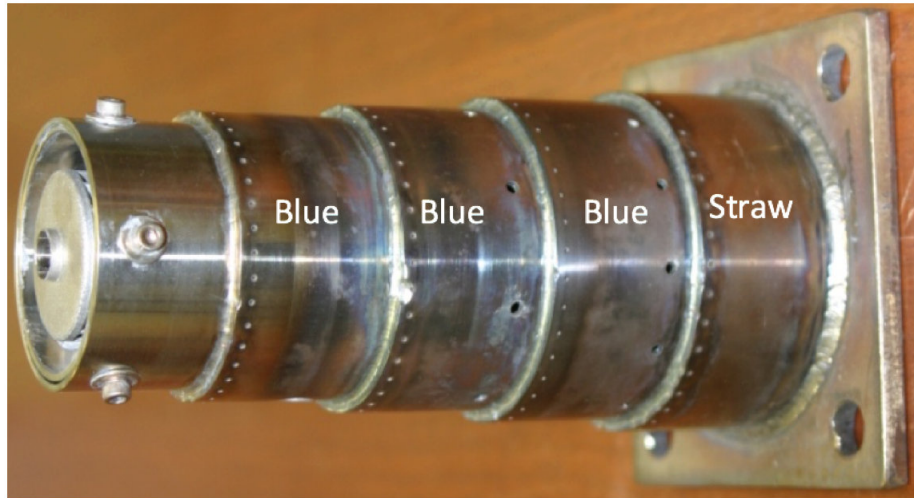


**Figure 66. Plenum Facing Surface of Can After Characterization**

Internally, significant changes were viewed. As seen in Figure 67, there was a hot spot that scorched the heat shield. Although difficult to see in the figure, the injector tube was just downstream of this can and likely created an inadvertent recirculation zone. Additionally, this possible recirculation zone may have been locally rich due to hydrogen doping when the ignitor was on. Close inspection of the cooling holes around this location did not show any blockages making the recirculation zone the more likely cause. The internal coloration of the can had blue sections similar to the plenum facing side, however, it also had some greener coloration. This greener color has been seen in previous experiments using ethylene at the test facility. The most important aspect of the internal view of the can was the lack of change to the shape. No deformation was seen as well as no blockages of any of the holes.

The same greenish blue coloring was also seen on the inner surface of the downstream reducer as well as coating the Inconel Kiel probe and the thermocouple. No indications of metal fatigue such as local hot spots were present within the reducer. The only component showing any signs of carbon scoring was the ignitor tube that

128
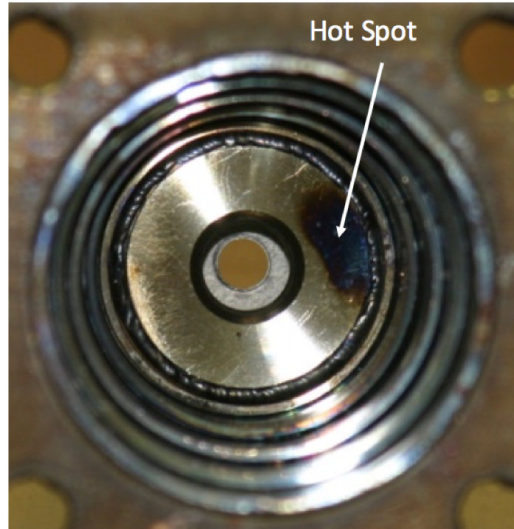
**Figure 67. Internal View of Can Burner**

caused the recirculation zone. In order to mitigate the recirculation zone, the tube was ground down slightly so that less length protruded into the flow.

The combustor characterization demonstrated the operability of the combustor and showed it possessed a relatively narrow, though well-defined, operating range with an artificial upper limit imposed by material limits. The post test examination showed no significant problems with the only issue having a relatively simple mitigation. No deformation occurred and none of the cooling holes were blocked. The testing also simplified the run procedure eliminating the need for a separate air line on the ignitor. With the combustor ready for integration to the wave rotor, the wave rotor checkout was completed next.

## 4.4    Wave Rotor Mechanical Checkout

### 4.4.1    Ping Test.

The ping test, performed by AFRL/RQTI, mounted the rotor a few different arrangements in an effort to constrain the rotor similarly to the boundary conditions

generated by the air bearing. The test used Laser Scanning Vibrometry to induce the natural frequencies within the rotor. Each test utilized highly reflective tape on the rotor in order to ensure the laser would reflect well. Three pieces were placed axially on the rotor and a single piece on each shaft. This can be seen in Figure 68. The tests reported vibromechanical modes as a frequency. This frequency corresponds to an RPM when multiplied by 60. For example, the design point rotation of 38,500 RPM corresponds to a frequency of 641.67 Hz. Although the specific results will be discussed, the different arrangements all produced a large amplitude frequency excitation well below 100 Hz. These frequencies correspond to bending moments for the shaft. Because they occur at relatively low rotational speeds, they imply greater than expected power requirements at startup as these vibrational modes must also be overcome in addition to the air bearing's start up torque. In addition to these low frequency modes, a couple of cases also had excitation at frequencies up to 641.67 Hz. These will be discussed on a case by case basis.



**Figure 68. Rotor with Reflective Tape for Ping Test**

### 4.4.1.1   Single Point Clamp.

This arrangement, fixed on the left side of Figure 70, held the rotor on the exit wall shaft where the aft bearings would normally be placed. The other shaft was unconstrained. This arrangement was used in two separate tests both of which analyzed the 0-1000 Hz frequency response range. The first utilized magnetic resonance while

the second was a piezoelectric shaker test. The magnetic resonance test placed a small Cobalt magnet on the rotor and used an electric magnet to modulate the magnetic field along the frequency range. Although there were a couple of small peaks, only one frequency produced a noteworthy response. This occurred at a frequency of 70.6 Hz. The full spectrum of this test can be seen in Figure 69.
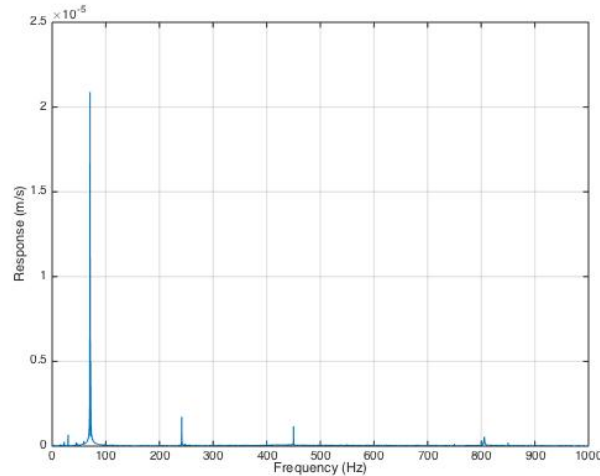


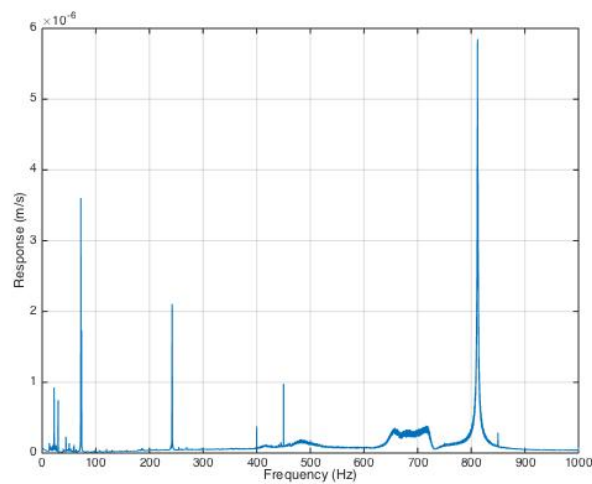**Figure 69. Magnetic Resonance Response Excitation**

The 70.6 Hz response was the first bending mode of the rotor. The implied bending would occur at the intersection of the rotor and the shaft. This frequency, 70.6 Hz, corresponded to a rotor rotational rate of 4,236 RPM. Because this response occurs at such a low frequency or RPM, it was not considered detrimental. Additionally, the dampening effects of the air bearing were not modeled exceptionally well by this arrangement either given the comparatively minor damping effects; however, the air bearing would serve to lower both the frequency of the bending moment and its amplitude. A test image showing the first bending mode is shown in Figure 70.

The piezoelectric test utilized a small piezoelectric motor to oscillate a small shaker table that held the clamp. This test resulted in stronger excitation responses than the magnetic resonance at all frequencies. Three frequencies stuck out the most. These

131
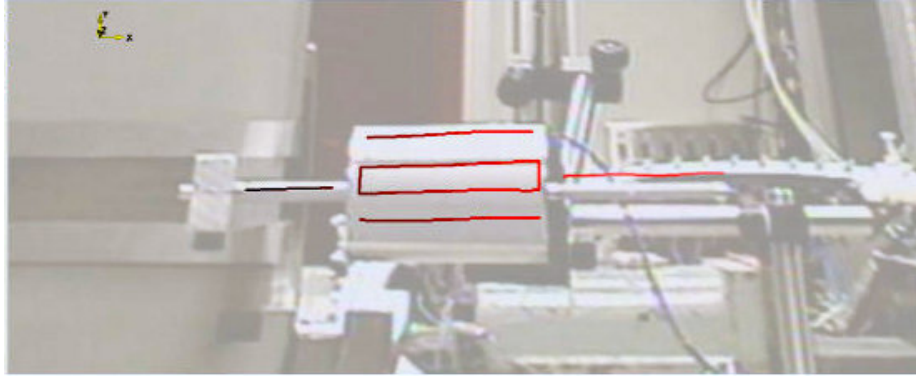
**Figure 70. First Bending Mode**

were the first bending moment, this time at 72.0 Hz, the second bending moment, at 811.8 Hz, and what appears to be the first torsional mode, at 242.3 Hz. This can all be seen in Figure 71.



**Figure 71. Piezoelectric Response Excitation**

Although the first bending moment had a greater amplitude and a slightly higher peak in the piezoelectric testing compared to the magnetic resonance testing, the same argument holds, and therefore, this was not a detrimental frequency. Similarly, the second bending mode was not a detrimental frequency as 811.8 Hz corresponded to a rotational rate of 48,708 RPM, well above the design speed. This could have

132

indicate potential issues at over-speed throttling, however, further testing would have been required to accurately model the air bearing. Rotor spin up, further discussed in Section 4.4.2, showed this mode likely happened at a lower frequency and speed requiring mitigation for continued operation. The second bending mode can be seen in Figure 72.
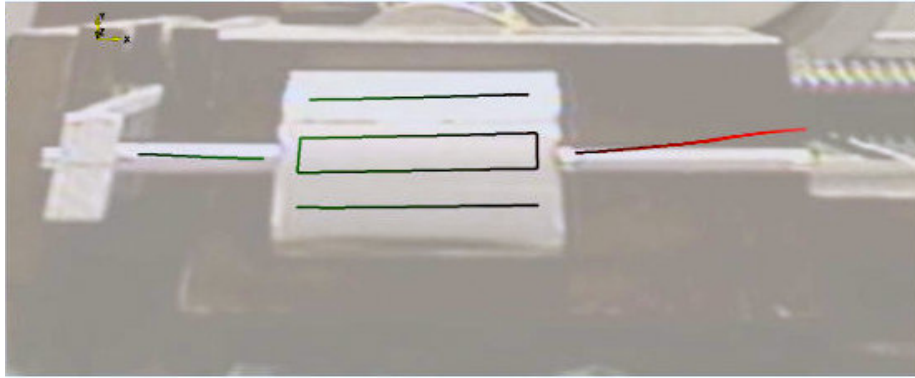


**Figure 72. Second Bending Mode**

The final mode of interest was the apparent first torsional mode at 242.3 Hz or 14,538 RPM. This mode was interesting as the test vibrated the rotor in a horizontal planar motion such that rotation of the rotor should not have been possible. Therefore, it was theorized by the experts that this frequency may have excited some sort of vertical oscillation of the rotor. Spinning the rotor was necessary to determine the effects of this potential mode and is discussed in Section 4.4.2. An image from this can be seen in Figure 73.

There is one potentially minor concern from the piezoelectric test that has not been detailed to this point. That is the slight uptick in response amplitude between 650 Hz and 730 Hz. Although the response was small, depending on how the other unmodeled aspects of the wave rotor system affect the dampening, this could indicate potential issues near the design point. Experimental testing was required to determine any significant problems. Though a more in-depth discussion is in Section 4.4.2,

133
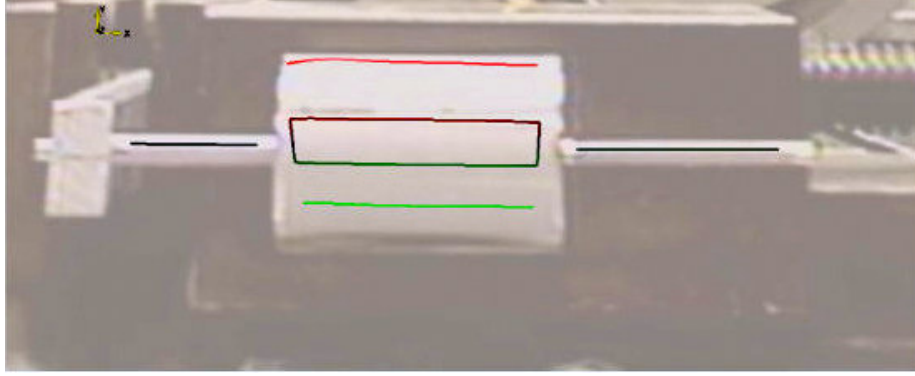
**Figure 73. Other Mode of Interest, Assumed First Torsional**

testing showed these modes caused significant affects and require further mitigation and damping to the system.

### 4.4.1.2 Double Support.

This test differed from the previous test in the manner at which the rotor was held. Rather than clamping the shaft at the aft bearings location, the rotor was simply supported at that location and just ahead of the rotor. This configuration, though undamped, reveals the natural frequencies of the rotor. The frequency was seen relatively close to the first bending moment at 59.1 Hz. The greatest peak occurred at 269.8 Hz and there were other smaller amplitudes throughout. Notably, there was no elevation in response near the operating frequency as seen in the piezoelectric test. The increasing amplitude for this test delayed until approximately 780 Hz. All of these data can be seen in Figure 74.
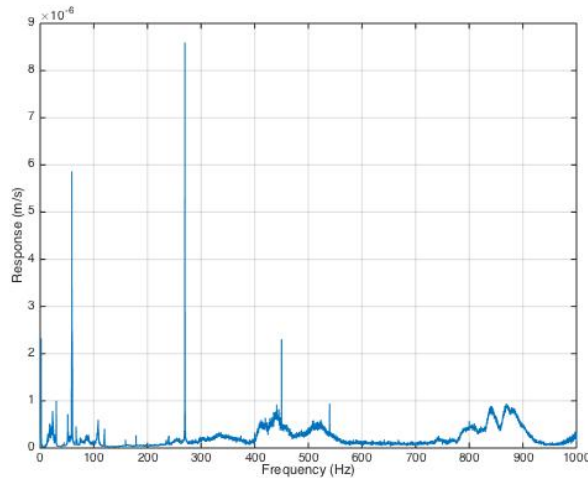
**Figure 74. Double Simple Support**

### 4.4.2   Spin Up.

The final component level test was to spin the fully assembled wave rotor in the configuration shown in Figure 41. Prior to attaching the motor, the rotational direction of the motor was checked. After ensuring the electric motor was spinning in the correct direction, the motor was connected to the wave rotor and a start was attempted. The motor's sensitivity to start up was such that it would go from zero rotation to a couple of thousand RPM with a minimal increase in signal pulse length. This caused a high torque loading and the first attempt with the standard coupling-set screw setup resulted in the set screw failing. The set screw was unable to maintain enough force upon the shaft to impart enough torque to the rotor to begin rotation. The set screw slipped and the few hundred to a few thousand RPM rotation rate resulted in the mid steel set screw quickly grinding down with the Inconel shaft acting similarly to a grinding stone. Note that images of the various set screw configurations were previously discussed in Section 3.8.3.

Initially the design change added a flat on both sides of the shaft but only kept the single set screw, however, a subsequent attempt demonstrated the necessity for a set

135

screw on both sides as the coupling would slip every few revolutions. Also important to achieving rotor start up was using the Teflon lubricant to reduce the static friction between the rotor and the air bearing. The double set-screw configuration, as shown in Figure 44, with Teflon based lubricant enabled rotor takeoff and the addition of Loctite to the set-screws to prevent them from vibrating loose enabled reliable start up of the wave rotor.

With the Loctite in place, rotor takeoff was achieved. Low speed difficulties required rapidly increasing the speed to 6000+ RPM in order to ensure rotation was sustained. Both the rotor and speed controller would heat up rapidly, especially if multiple starts were attempted. This issue led to a few testing modifications. The first was blowing air on both the speed controller and the motor in order to convectively cool them. The other change was spacing out start up attempts early on until it would reliably start every time. Coupling these two changes together allowed the electric components to remain relatively cool and functional. In one test sequence, the rotor speed was increased peaking around 30,000 RPM, however, a small puff of smoke was visually observed so the experiment was quickly shut down. The cause of the smoke was not seen during the test.

An inspection of all components was done as well as testing the motor and speed controller unattached to the rotor. The motor still spun indicating that none of the components short circuited or melted internally. However, there was suspicion of the high amperage components of either the ESC or motor being damaged. The wave rotor showed no signs of impacting the end walls although the lubricant showed signs of high friction likely occurring while the air bearing was establishing the boundary layer. Due to the immense start up power required and the ESC's 100 A limit, a larger ESC was purchased. Prior to the installation of the higher amp limit ESC, an attempt to use the 100 A ESC in an air-assisted spin up test was conducted. However,

136

this test is pending. Plugging the ESC into the battery generated a short circuit and rendered the ESC inoperable.

Using the higher amperage, Phoenix Edge 200, ESC, the design rotor speed was successfully reached. The air-assisted (2.12 kg/min) start had no problems with the start-up torque and easily powered the rotor, as seen in Figure 75. A slight mode around 27,000 RPM seemed to be present but a minor throttle increase easily overcame this. The approximate design speed was briefly maintained with some speed oscillations of a few hundred RPM peaking at 39,263 RPM, shown in Figure 75. Other takeaways from Figure 75 are the current draw and the throttle settings. The throttle setting shows where extra power was needed to push through tiny modes whereas the current shows the power draw to the motor. Most of the high speed operation required a current between 55 A and 95 A.

At some point around the peak, a flash was noticed near the motor-shaft coupling and the rotor speed instantly dropped to about 34,500 RPM; Figure 75 correlates well with this as it shows a large current spike to almost 190 A. Following this, the test was ended to inspect all components. Neither the motor nor ESC were very warm to the touch, although inspecting the wave rotor, some of the lubricant was noticed to have leaked out the shroud.
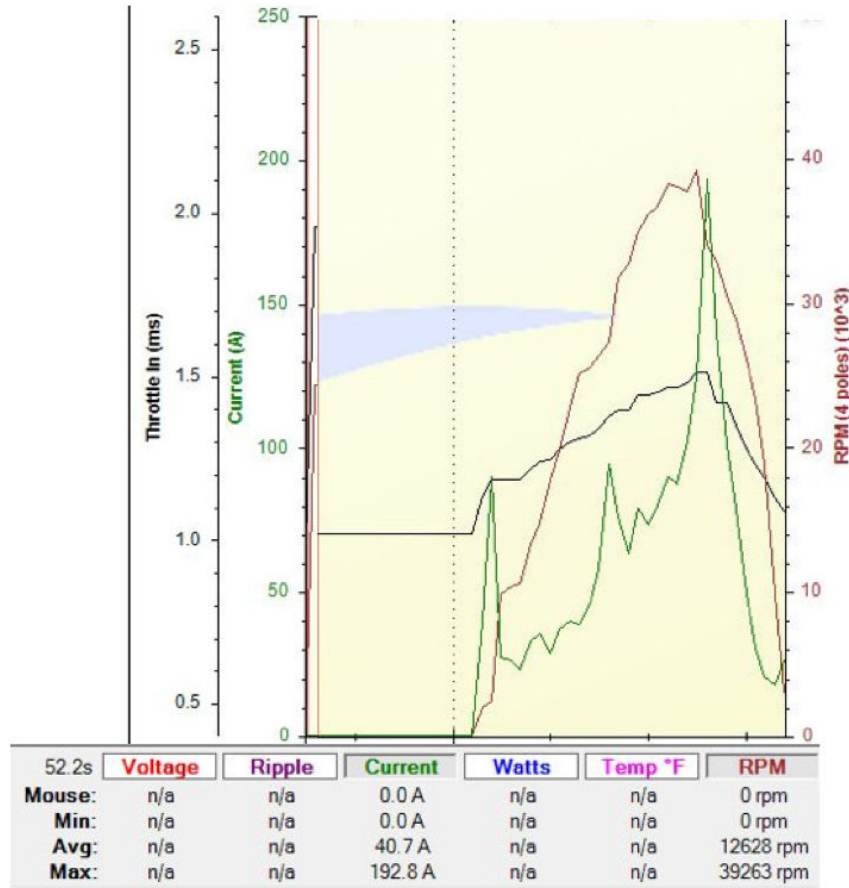
**Figure 75. ESC Data Log**

After taking the wave rotor apart, damage was observed to a few components; however, the damage was negligible to non-existent for most of them. The rotor, shown in Figure 76, had a few noticeable changes. The first is the minor scarring from the air bearing visible around the rotor. This marking was somewhat expected and not considered detrimental to operation. There was also a slight impact mark on the inlet side indicating an endwall impact; the inlet wall (not shown) mirrored this; however, the end of the shaft was cause for major concern. Note all of this testing occurred on rotor 1; however, the same result would likely occur with rotor 2.

Figure 77 shows the damage to the end of the shaft that connects to the motor with Figure 78 zooming in further. It is theorized that something caused a portion of

138
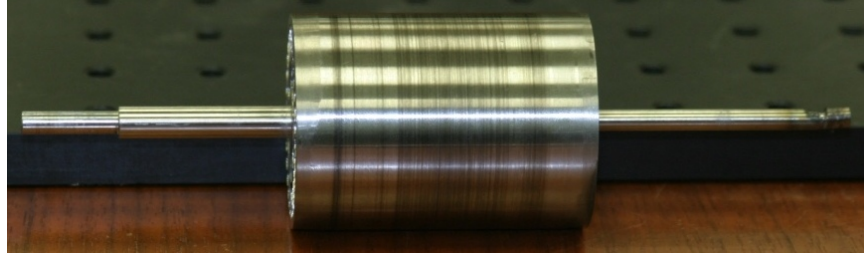
**Figure 76. Rotor After Spin Up**

the shaft to impact the stainless steel of the motor mount. The impact generated the visible spark due to metal grinding on metal. This heat allowed the tip to bend and remain in contact with the motor mount and ground down causing the damage shown. Currently, it is believed that, although the ping test showed the second bending mode to be present at 812 Hz, the air bearing and/or the motor couplings generated further damping in the system that pulled the mode down to the 650 Hz range. The second bending mode has the correct type of excitation to cause the tip of the shaft to deflect into the motor mount. Current mitigation to solving this is ongoing; however, it has been decided that a bearing must be placed on the inlet side shaft. The anticipated solutions requires a modification to the inlet wall in order to place a bearing within the the motor mount in order to prevent the shaft from this movement.

## 4.5   Conclusion

This chapter has detailed the results of this research. First, the computational results were discussed for two different cycles: a 3 kW cycle and a 1.5 kW cycle; however, only the 1.5 kW cycle included off design operation. The 1.5 kW cycle was chosen for manufacture due to the aggressive combustor exit temperature required for the 3 kW cycle. The 1.5 kW modeling predicted 1.79 kW of power within the exhaust stream and also showed potential for reasonable off design operation. Following the cycle design, the components were all manufactured. Included within the

139
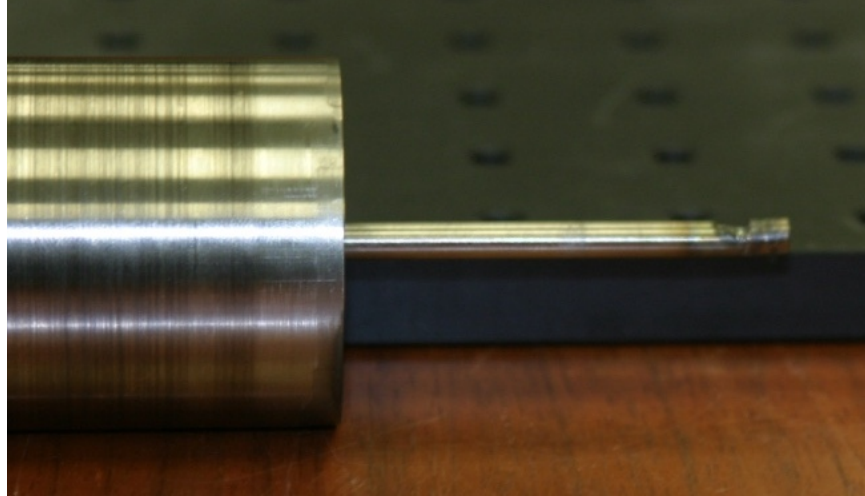
**Figure 77. Rotor Shaft After Spin Up**



**Figure 78. Rotor Shaft After Spin Up, Zoomed**

manufacturing was a custom-design combustor to drive the cycle.

After all of the components were built, several components underwent performance testing for either characterization or mechanical checkout. The discharge coefficients were determined for the venturis and the spray angles for the fuel nozzles were found. The combustor was characterized for ignition, design point operation, and mass flow range. The last series of testing occurred on the wave rotor itself. The rotordynamic analysis did not present any serious causes for concern and the rotor was spun up. After an ESC change and utilizing air at start up, the rotor achieved the design point speed. An unanticipated grinding issue brought the test to a halt and revealed

significant damage to the inlet side shaft requiring ongoing modification.

# V. Conclusion

Today's drone market is rapidly expanding. The advancements in small computers and high speed video uplinks is pushing the range and altitude of these small aircraft like never before. One significant problem preventing more widespread application is that the hardware advancements are not keeping pace with the electronics advancement nor the demand of the users. The key hardware issue for many is the power supply. While battery energy density is improving, the energy density of an internal combustion engine such as a jet engine or a piston engine is unmatched by anything an electric powered motor can supply.

A combustion engine needs only about 5% efficiency to exceed the breakeven point [12]. Although 5% may seem very inefficient, typically small engines only have efficiencies around 10%. However, as the size decreases further, that value will approach 5%. This does not account for increases in battery efficiency increasing the break even point to greater than 5%. This is the problem. Therefore, there is a desire to increase the efficiency of small engines. Additionally, the efficiency drops faster than the size scales down. Although through great effort, it might be possible to push existing technologies slightly smaller, they are rapidly approaching the physics based limit where electric motors are better. A possible solution to maintaining the superiority of hydrocarbon based combustion engines is to utilize a wave rotor. This research has designed, manufactured, and tested a kilowatt power class wave rotor working towards demonstrating the greater efficiency of pressure wave based energy exchangers as opposed to turbine based or cylinder based devices.

## 5.1 Objectives

Chapter 1 outlined a series of tasks for this project to accomplish in order to achieve the project's objective of a kilowatt sized engine for a Class 2 UAV and they have been restated below for reference.

1. Computationally model the Brayton cycle wave rotor using the NASA code developed by Paxson [1] [2] [3].

2. Design and manufacture the wave rotor hardware and accessories necessary to achieve the modeled cycle via computer aided design software.

3. Design and build the combustor necessary to drive the energy exchange for the wave rotor.

4. Test the wave rotor and combustor in an uncoupled manner.

5. Couple the wave rotor and the combustor for cycle validation.

6. Analyze off-design operation of the wave rotor.

In support of the first task, two wave rotor cycles were designed. The first, although arguably a better cycle, required a combustor temperature greater than the safety threshold desired within the lab. Therefore, the second cycle reduced the combustor exit temperature and was designed to produce approximately 1.79 kW of power within the exhaust stream. Note this power does not account for the power of the electric motor driving the wave rotor. This was done in order to show proof of concept for wave rotor technology.

With a computationally designed wave rotor cycle completed, work for the second task began. This work encompassed the design of the wave rotor, the endwalls, and all of the supporting components. Some of the other components were designed by other companies such as the air bearing and the venturis, while others were designed in house such as the motor mount, the shroud, and all of the combustor components.

This combustor branched into a separate task entailing the design and manu-

143

facture of a combustor for the 1.79 kW cycle. This design utilized the simple, yet efficient, can-type combustor design. Using the wave rotor's CO and TI conditions for the desired inlet and outlet, the internal arrangement of the air injection scheme, sizing, and cooling was chosen. This design was examined by an expert and, with his approval, manufactured.

After the manufacture of the various components, component assembly was completed so testing could begin in support of the fourth task. Component testing expanded from only testing the wave rotor for mechanical issues and characterizing the combustor to a host of other smaller tests. These other tests included flow testing to determine the discharge coefficient of the venturis and the cone angle of the fuel injector as well as the rotordynamic analysis of the wave rotor via ping testing. Although this was part of the fourth task, various aspects of it were needed to complete the second task, such as the final shroud dimensions. This objective also yielded many problems or potential problems that required solutions prior to coupling all components. Notable in this was the ESC current (amperage) issue.

Given the length required for completion of task four and the lead time to obtain parts to mitigate some of the issues, the final two objectives were not completed. However, the coupling of the rig is near completion and testing to finish these objectives will commence when the final parts are finished.

## 5.2  Conclusions and Significance of Research

Although coupled testing has not yet started, the component testing revealed many of the problems that may have occurred during coupled testing. The necessity of a hot-air assisted start was one of these important revelations. It is also possible to establish a rough efficiency estimate, using Equation 1, based on the estimated power produced from the computational results and the fuel flow rate found during

144

combustor testing. This sort of estimate would place the efficiency around 11%, on par with small engines of this power class if electric power is not included. If electric power is included, this efficiency is only about 3%. These values are poor estimates as they combine computational work with partial experimental work. True efficiency can not be determined until the coupled system has been tested.

Further work is required to accurately calculate the system efficiency and based on the lessons learned from this research, future designs would improve system efficiency to a level unseen by small engines. Traditional small engines, both jet and piston, suffer from physics based limits that wave rotors possess greater immunity to. By taking advantage of these systems, it is possible that while a wave rotor based system may cost more upfront, the savings over the lifetime due to reduction in fuel costs will more than make up for shelf price.

## 5.3  Recommendations for Future Research

The immediate recommendation is to finish the modifications to add a bearing to the inlet side then complete the coupled testing: both the design point and the off-design throttling. This will provide concrete data to support the efficiency claims and also provide valuable insight on how to modify the design to improve the efficiency.

Concerning this wave rotor specifically, research into utilizing a liquid rather than gaseous fuel could be an area of research, but greater emphasis should be placed on reducing the combustor size to something more realistic in terms of volume in order to fit on a Class 2 UAV.

Further research is also desired to modify the wave rotor passage design such that it is capable of operating without a motor in a configuration far more similar to a traditional turbomachinery powered jet engine. This would make the rotor RPM dependent on the TI temperature and therefore, on the fuel flow rate.

145

## 5.4 Summary

At this point, the wave rotor research has shown promise in projected efficiency. This project designed a wave rotor cycle using a NASA GRC developed Q1D CFD code. A majority of the components were designed in house via CAD software and manufactured in order for testing. In addition to the wave rotor, a small, can-type combustor was designed and built specifically to drive the energy exchange inherent to wave rotor operation. After the manufacture of the components, extensive setup was done in order to test all of the various components including, but not limited to, the wave rotor and the combustor.

A majority of the work necessary to test the coupled rig in a closed loop configuration has been completed, and tests are pending. Based upon the results of the component testing, further research should be done demonstrate the outstanding capability this technology has, including the potential to revolutionize power generation for Class 2 UAVs.

# Appendix A: Code Terms Defined

| Q1D Term | Non-Dimensional Meaning | Physical Components/ Definition |
|---|---|---|
| OMEGA | Rotational Velocity | $\frac{RPM(\frac{rad}{s})*Length}{RefSonicVelocity}$ |
| RESTAR | Reynolds Number | $\frac{RefDensity*RefSonicVelocity*Length}{RefViscosity}$ |
| DONL | Rotor Diameter | $\frac{HydralicDiameter}{Length}$ |
| HONL | Cell Height | $\frac{PassageHeight}{Length}$ |
| PGAP/WGAP | Leakage Spacing Between Rotor and Endwalls | $\frac{EndwallSpacing}{ChannelHeight}$ |
| RADIUS | Rotor Radius | $\frac{\frac{InnerRadius+OuterRadius}{2}}{Length}$ |
| THETOT | Opening Time | $\frac{2\pi}{\#ofCells}$ |
| BETA# | Port Incidence Angle | $atan\left(\frac{OMEGA*RADIUS}{UBAR}\right)$ |
| $A_{port}$ | Port Area | $\frac{(r_o^2-r_i^2)*ArcLength_{port}}{2}$ |
| MFCORR | Corrected Flow Rate | $\frac{\dot{m}\sqrt{T_{t_{CI}}}}{P_{t_{CI}}*A_{CI}}$ |

148

# Appendix B: Code Usage Guide

## Useful Commands

nano - edit files cd - change directory ./name - run executable files e.g. ./wr executes wr

## Compiling Executables

### THIS STEP IS ONLY DONE THE FIRST TIME

### Compile WRITR.

In the command prompt, type the following and press enter:
1. gfortran c writrrtf.f bc.f roeint.f
2. gfortran o writr writrrtf.o bc.o roeint.o

### Compile WR.

In the command prompt, type the following and press enter:
1. gfortran c wrf.f bc.f roeint.f
2. gfortran o wr wrf.o bc.o roeint.o

### Compile SIMBC.

In the command prompt, type the following and press enter:
1. gfortran c 4psim.f bc.f roeint.f
2. gfortran o simbc 4psim.o bc.o roeint.o

## Using WRITR

### DESIGNING A NEW CYCLE BEGINS WITH THIS STEP AFTER COMPILATION OF EXECUTABLES

### a Priori Inputs.

Know a priori inputs i.e. T4T1, GAM. Guess EXPRAT, THETOT in input.dat
i. FSSC=0.4826
ii. PRI, NCT, BLEED, IDLAND=1.00000
iii. PNTS = 51
iv. DX=0.02000
v. DTI=0.01000

**Bottom vs Full Cycle.**

i. Iterate through EXPRAT, THETOT until output conditions converge and are desirable, If targeting power output, use the T4/T1 for exit temperature and P4/P1 for exit pressure ratio

ii. With desirable exit, UPCYC = 1, further iterate until desirable output conditions converge

iii. This will generate an output file titled wrbc.new, This is the file for WR

**Using WR**

**Normalize.**

Normalize conditions in wrbc.new and resave as wrbc.dat

i. P1, P2, P4, P5 are all divided by P1

ii. T1, T2, T4, T5 are all divided by T1

iii. All THETAL1-4 and THETAR1-4, DTI, THETOT and THETMX are divided by the square root of T1

iv. THETCY=THETMX

v. In the middle of the file are four columns, they are pressure, density, velocity and temperature

1. Every term in the pressure column must be divided by P1

2. Every term in the density column must be divided by P1 and multiplied by T1

3. Copy four columns into wrbc.dat from wrbc.new and run. Repeat until minimal to no changes in columns.

**Sizing.**

Turn on sizing parameters, DONL, HONL, RADIUS, OMEGA, RESTAR

i. $DONL = \frac{d*}{L}$ d* is hydraulic diameter

ii. $HONL = \frac{h_c}{L} L$

iii. $RADIUS = r_{avg} L$

iv. $OMEGA = \frac{rotorspeed(rad/s)L}{a*}$ Note a* is ref sonic velocity

v. $RESTAR = \frac{\rho*a*L}{\mu*}$

**Number of Cells.**

When determining the number of cells, it is $\frac{2*\pi}{THETOT} = \#$, then round up the number of cells to nearest whole number. $\frac{2*\pi}{\#(integer)} = THETOT$

**Port Sizing.**

Reference port locations to 0 to pi radians

i. $\frac{\pi}{THETMX} = refnum$

ii. Multiply all port locations (THETR/Ls) by refnum

150

**BETA.**

Add in beta terms, $beta = atan(\frac{OMEGA*RADIUS}{UBAR})$

**Match Mass Fluxes.**

Iterate upon length and rotor velocity until MF1 MF4 and MF5 MF2

## Using SIMBC

i. Add SIMULATE terms to bottom of wrbc.dat. see sample 4psimbc file. 4psimbc is now active file

ii. Modulate QCORR and BLOSS to match wr output values running SIMBC each time

iii. Add in PGAPs and WGAPs $xGAPs = \frac{wall_{spacing}}{channel_{height}}$

iv. WALONL=0.03000

v. Run SIMBC and copy 4psimbc.new as 4psimbc.dat (cp 4psimbc.new 4psimbc.dat)

vi. CD=0.8000

vii. RUN SIMBC

viii. PRANDTL=0.7

ix. MESS WITH OMEGA THROUGHOUT HERE TO MAINTAIN MF Matching, if needed for Ps and Ts modulate QCORR and BLOSS

x. Slowly turn on RHLVC and RHLVB. Begin with 0.00050 and double each time until no longer converges. Split difference from last usable case and try again. DO NOT EXCEED 0.5000 for RHLVC and 0.05 for RHLVB

xi. Engage RHLVV slowly. This will not get as high as the other terms

xii. Increase AV until no more convergence

xiii. Save 4psimbc.new as 4psimbc.dat

xiv. Delete SIMULATE Terms and save as wrbc.dat

## Visualization

i. Run new wrbc.dat file in wr

ii. Run MATLAB Script from same location as wrbc.dat file

## Real Conditions Results

i. Copy SIMBC output screen.

ii. Space appropriately to put into excel file

iii. Put in excel file

# Appendix C: Operating Procedure for Combustor Test

## Introduction

This Standard Operating Procedure (SOP) applies to all personnel, government and contractor, that will be operating the T63 combustor/vitiator in Bldg 71A, D-Bay. This document establishes step-by-step procedures for conducting the operation to protect workers from physical harm. It addresses the emergency action to follow. All personnel involved in the operation must understand the hazards prior to starting this operation.

## Document References

AFRL/RZ OI 91-202, Environmental, Safety and Occupational Health (ESOH) Programs
AFRLI 91-101, Laboratory System Safety Program
RQ Chemical Hygiene Plan
PDRF Safety Hazard Analysis

## Area Access and Control

Take appropriate steps to warn personnel of the hazardous operation and action to prevent unauthorized personnel access.

### Personnel Protective Equipment (PPE) Requirements.

Safety Glasses/Goggles required for handling fluids, high pressure systems, and machining operations
Ties/ID badges/loose items shall be appropriately secured when working in the lab.
Hearing protection required for exposure to elevated noise levels
Lab coats, coveralls, or suitable fire resistant clothing required for handling fluids.
When specific tasks are performed, additional appropriate PPE will be mandated.

## PRETEST

### GENERAL FACILITY PRETEST OPERATIONS.

1. Turn on test cell lights (2 switches).
2. Turn on doorbell.
3. Turn on closed-circuit television systems and select appropriate channel and views.
4. Verify that vapor detectors are on and indicating a normal condition. (green light on)

5. Turn on 5 and 24 VDC power supply switch on control console. (below vapor detectors)

6. Pull emergency stop button on control console.

7. Energize reset switch (light on).

### TEST CELL SETUP and INSPECTION.

8. Verify test cell door safety switch is operational.

9. Verify that fire extinguishers are in their proper location.

10. Verify caps and covers for open ports, lines, hoses, electrical connections, ducts, tubes, and cavities are properly configured.

11. Inspect area for objects or materials that might adversely affect testing and/or personnel safety.

### CAN BURNER SETUP and INSPECTION.

12. Manually connect hot outlet line from T63 to flex line attaching to inlet reducer on can burner.

13. Ensure all thermocouples (2) and pressure transducers (2) are functional and powered with 28V.

14. From control room, ensure laptop is talking to the DAQ and pressure/temperature measurements match ambient conditions.

15. Check all sonic nozzles for proper size and instrumentation.

### TESTING

### TEST STARTUP.

1. Turn on Red Warning Light using switch on console.
2. Secure the fuel room and test cell.
3. Sound horn and verify all personnel have left the test cell.
4. Close inner test cell door and display "Test in Progress" sign.
***TEST CELL MUST BE SEALED FROM NOW ON***

### T63 COMBUSTOR/VITIATOR START AND RUN PROCEDURE.

1. Make sure Emergency Stop is not engaged
2. Press reset button next to E-Stop
3. Turn on AC/DC power for test setup and solenoids
4. Verify camera feeds and set view
5. Enable data acquisition and control
6. Check the COM channels
7. Turn on combustor/vitiator air
8. Turn on ignitor power
9. Verify that all the data reads correctly

153

10. Turn on combustor/vitiator fuel

11. Monitor surface temperature of combustor/vitiator output to verify that combustor/vitiator is lit.

12. If output temperature does not rise within 10-15 seconds, stop fuel flow, turn off ignitor, and continue air flow to purge the device for 30-60 seconds before returning to step 8 and trying again.

## CAN BURNER START AND RUN PROCEDURE

1. Ensure valves to ignitor are closed. Begin ethylene fuel flow. If inlet air from T63 is hot enough, auto-ignition within burner may happen. If auto-ignition occurs, go to step 3. Ignition will be known as outlet temperature will rise dramatically.

2. Cease ethylene flow to burner. Plug voltage BNC into appropriate terminal and begin current flow. Open valves to ignitor and begin both air flow and fuel flow. Once flame is established, unplug voltage BNC move to step 3.

3. Begin ethylene flow to burner. If ignitor is on, close valves and monitor temperature. If temperature begins dropping to inlet temperature, repeat step 2.

4. Monitor both inlet and outlet temperatures for fluctuations and alter fuel flow rate as necessary.

## SHUTDOWN

### CAN BURNER SHUTDOWN.

1. Turn off fuel flow
2. Proceed to T63 shutdown

### T63 COMBUSTOR/VITIATOR SHUTDOWN.

1. Turn off fuel flow
2. Continue to flow air while monitoring surface temperature of combustor/vitiator output to verify shutdown
3. Turn off ignitor power
4. Turn off AC/DC power for test setup and solenoids
5. If necessary, purge the fuel line(s) between the bottles and rig.
   ***TEST CELL MAY BE UNSEALED AT THIS POINT***
6. De-energize red warning light switch located on console.
7. Push emergency stop (panic button).
8. De-energize 5/24 VDC power supply.

### FUEL SHUTDOWN.

1. Close valve(s) on the fuel supply bottle(s).
2. Check for empty fuel bottles–replace or note for future reference.
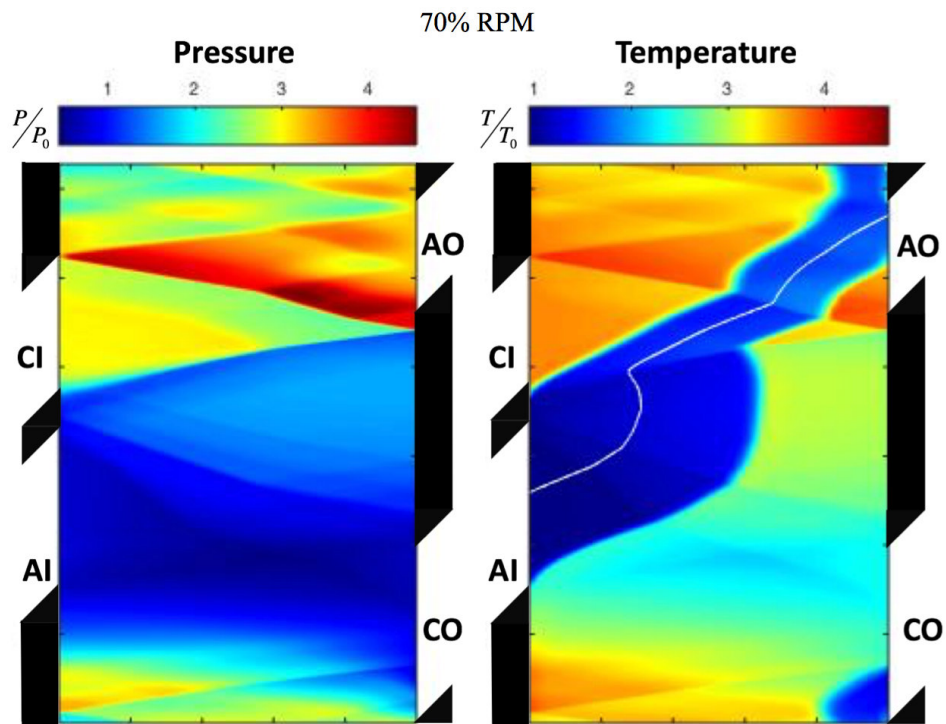3. Close exhaust door.

154

## CAN BURNER FINAL SHUTDOWN.

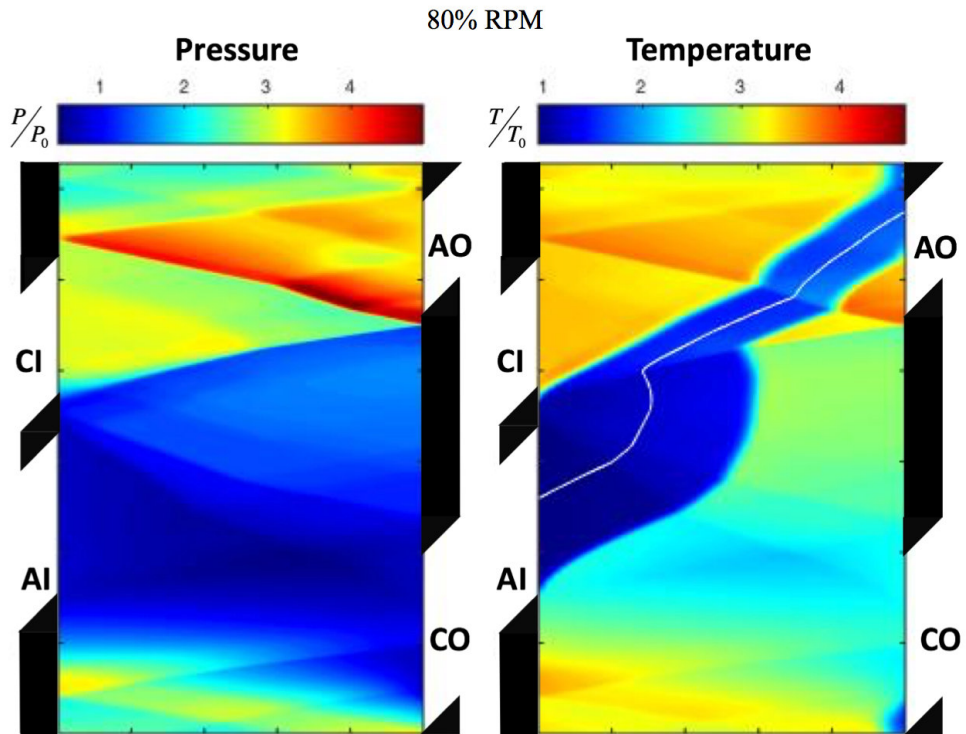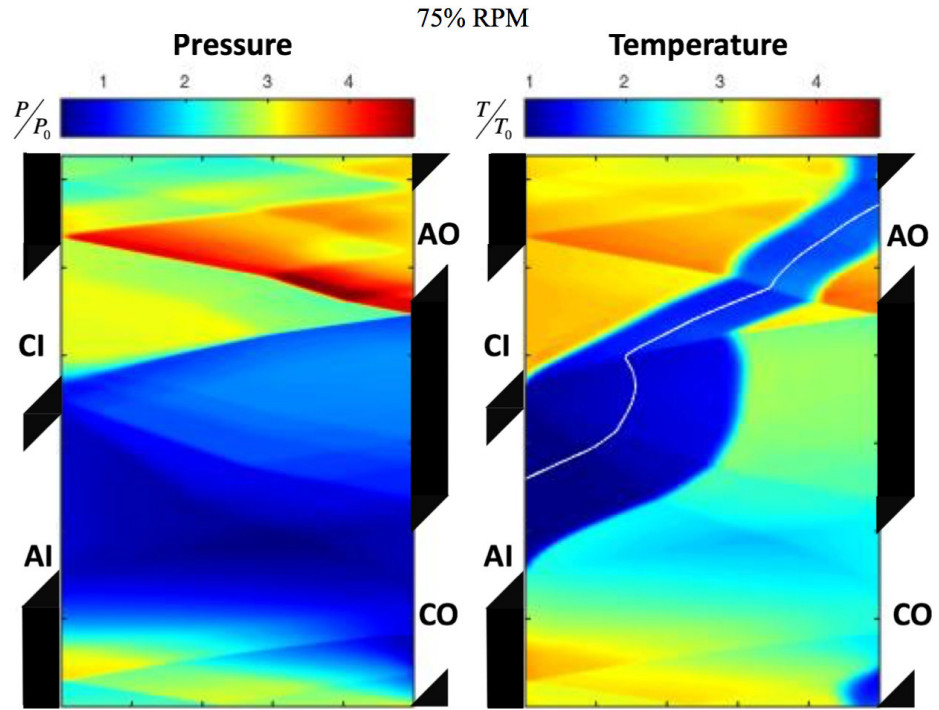1. Unplug power.
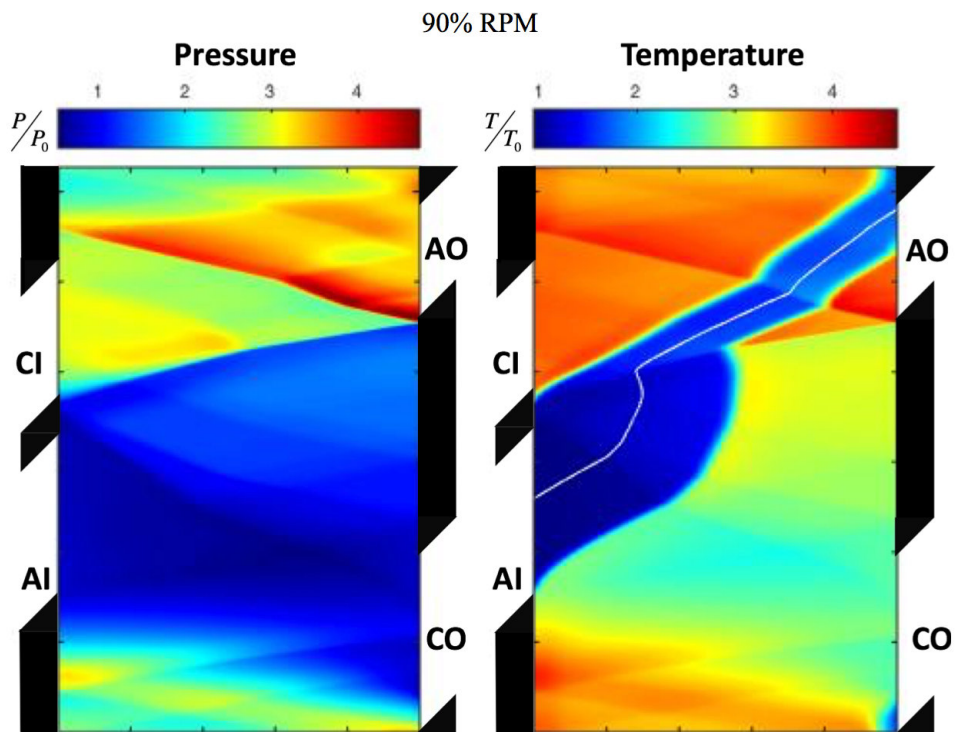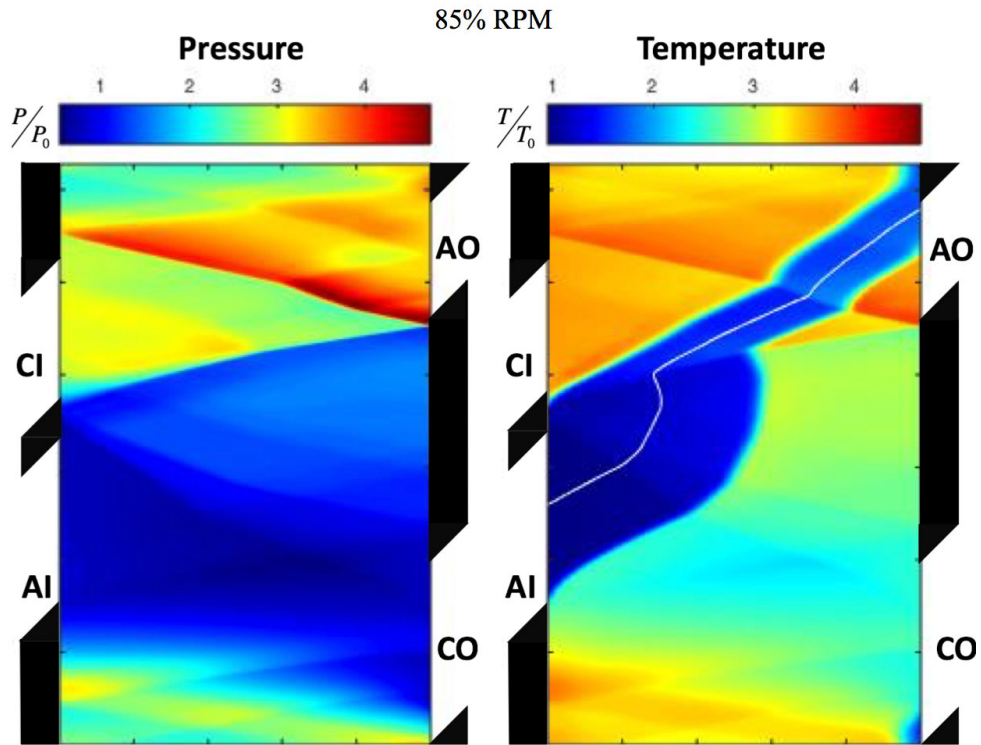2. Check all parts for heat stress when cool.

## FINAL SHUTDOWN.

1. Shut down facility software program.
2. De-energize Berkeley box(es).
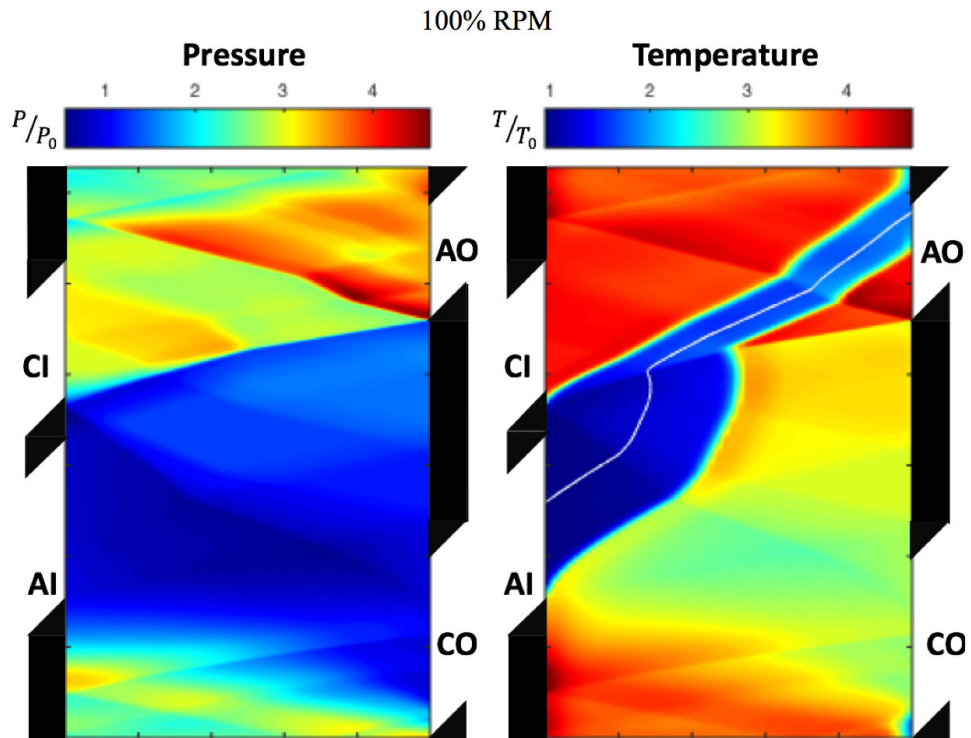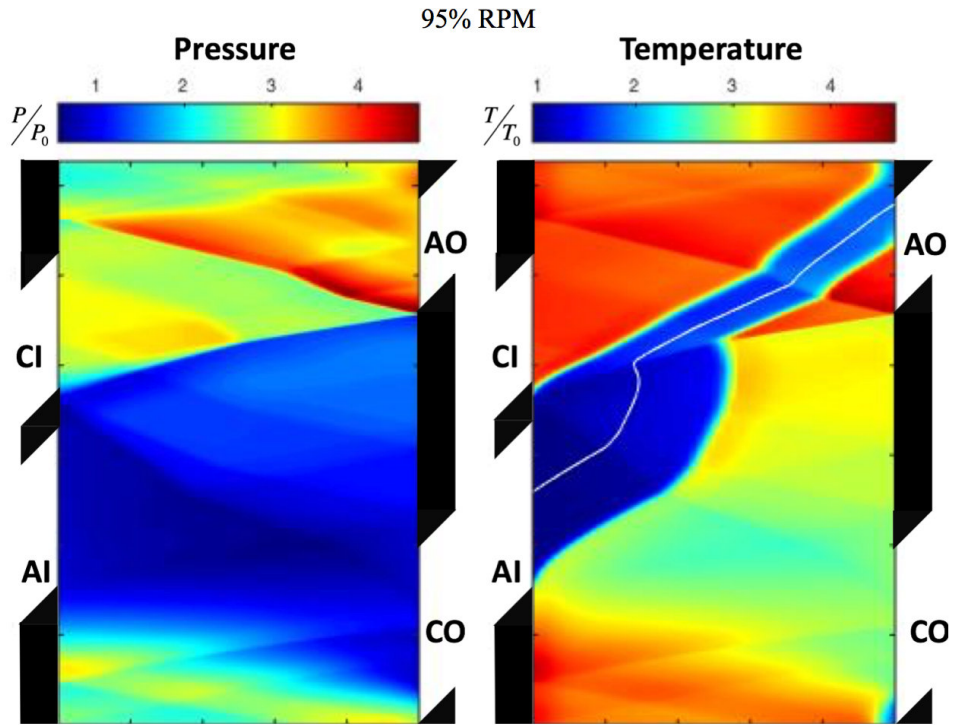3. Turn off closed-circuit televisions and system controller.

# Appendix D: Modified Color x-t Diagrams

This appendix contains the off-design x-t diagrams. Every x-t diagram utilizes the same color scheme such that the 100% case is the previously seen design point and all others are colored over the same range. This leads to low speed cases being more bluer and high speed cases being more red.



70% RPM

75% RPM

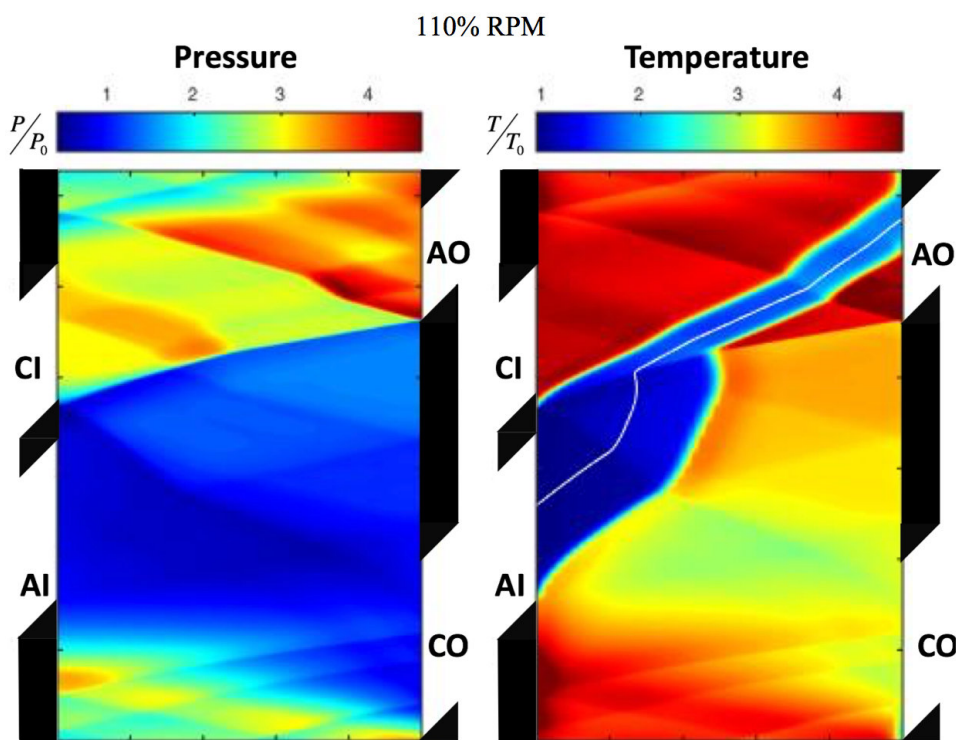Pressure    Temperature

80% RPM

Pressure    Temperature

157

85% RPM

Pressure — $P/P_0$

Temperature — $T/T_0$

90% RPM

Pressure — $P/P_0$

Temperature — $T/T_0$

95% RPM

100% RPM

105% RPM

Pressure — Temperature

110% RPM

Pressure — Temperature

115% RPM

120% RPM

125% RPM

Pressure — $P/P_0$

Temperature — $T/T_0$

AO  CI  AI  CO

130% RPM

Pressure — $P/P_0$

Temperature — $T/T_0$

AO  CI  AI  CO

162
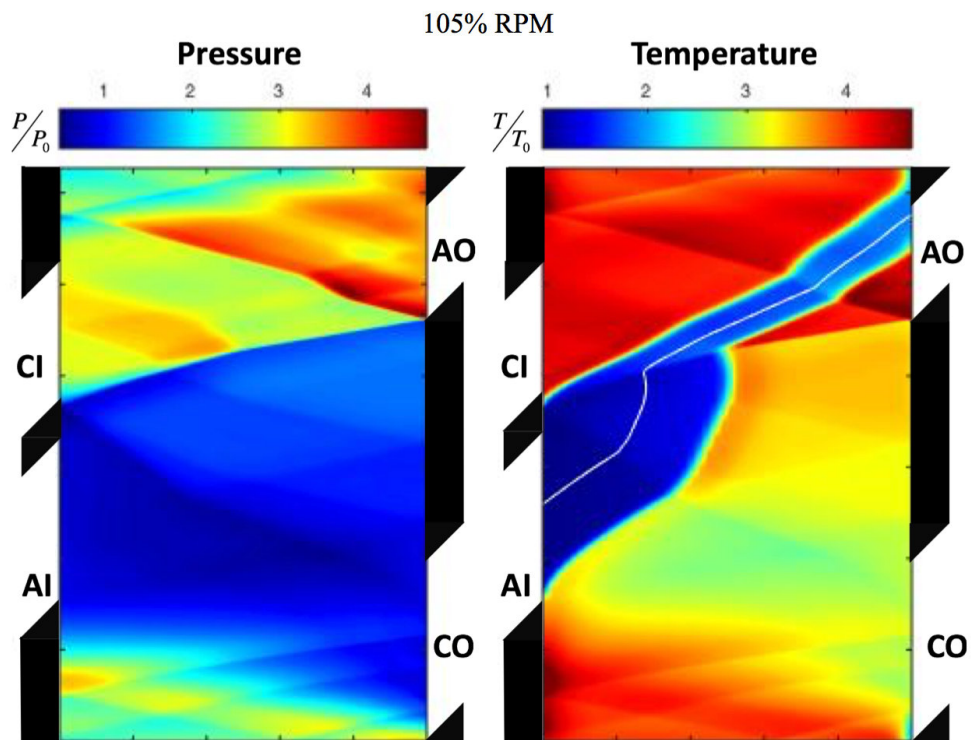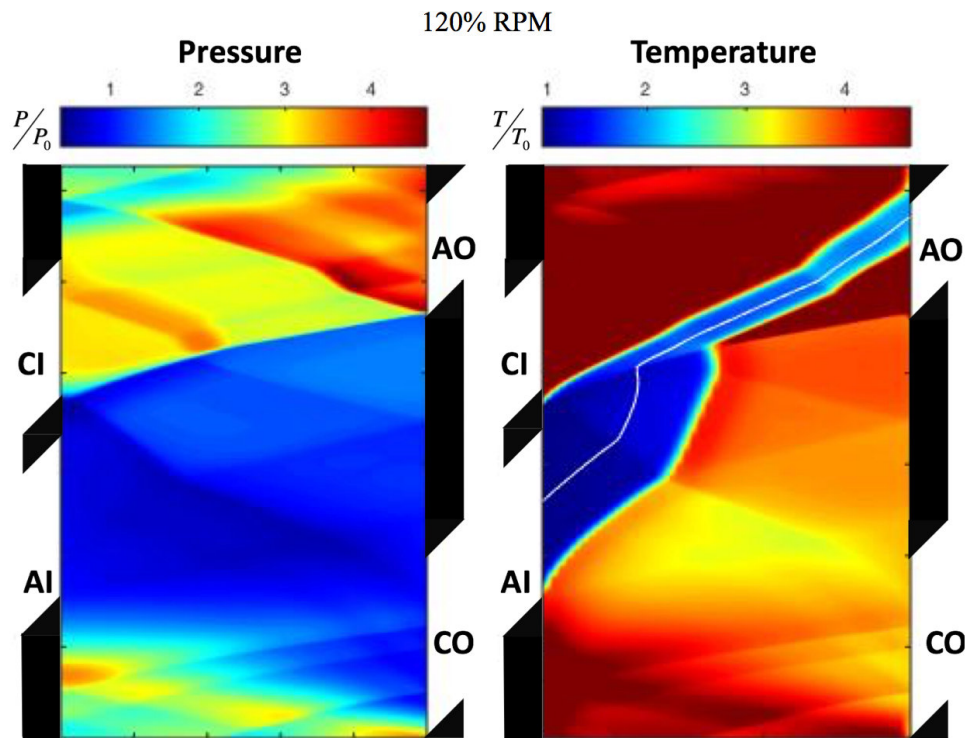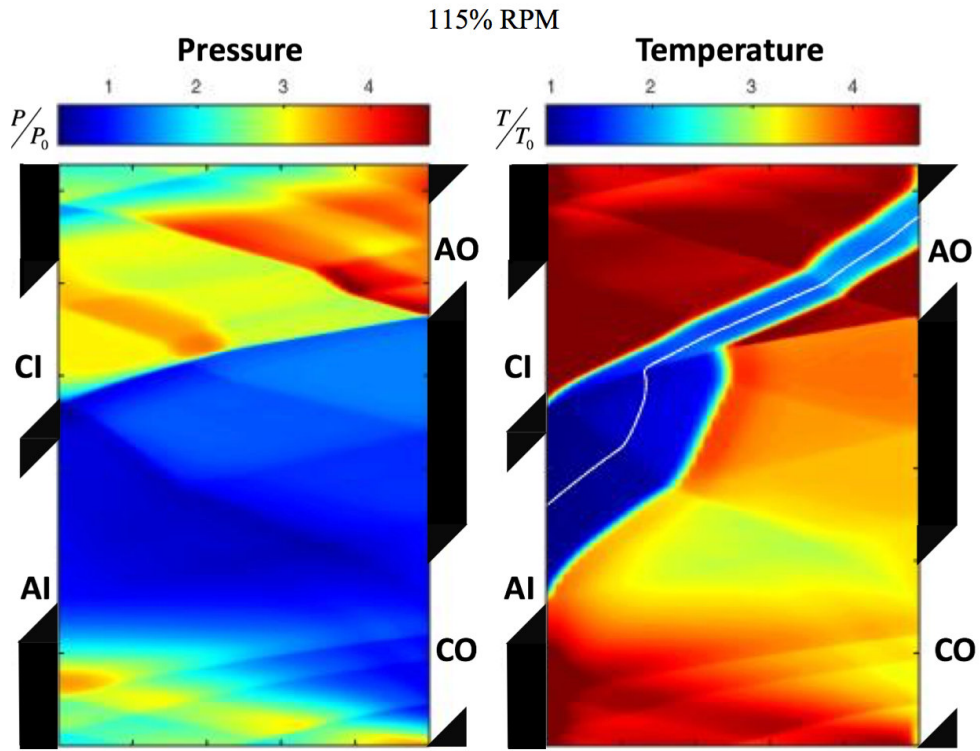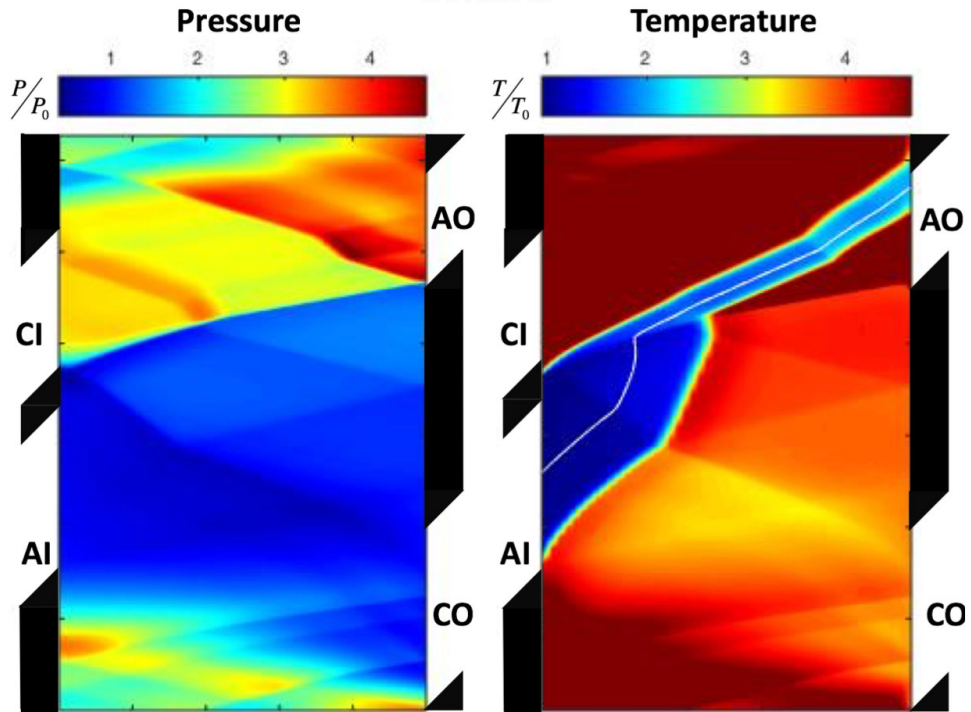
www.manaraa.com

The final two images in this Appendix are the unaltered 80% and 120% Design RPM images for the reader's reference.

80% Design RPM-Unaltered Colorbar



120% Design RPM-Unaltered Colorbar



163

# Appendix E: Throttled Port Conditions

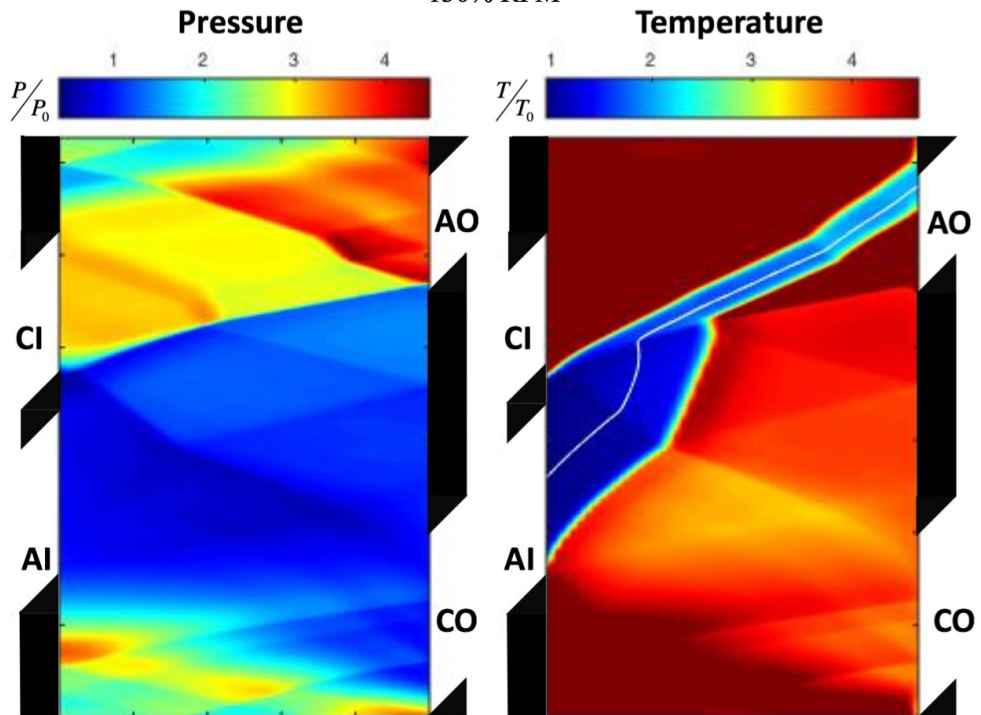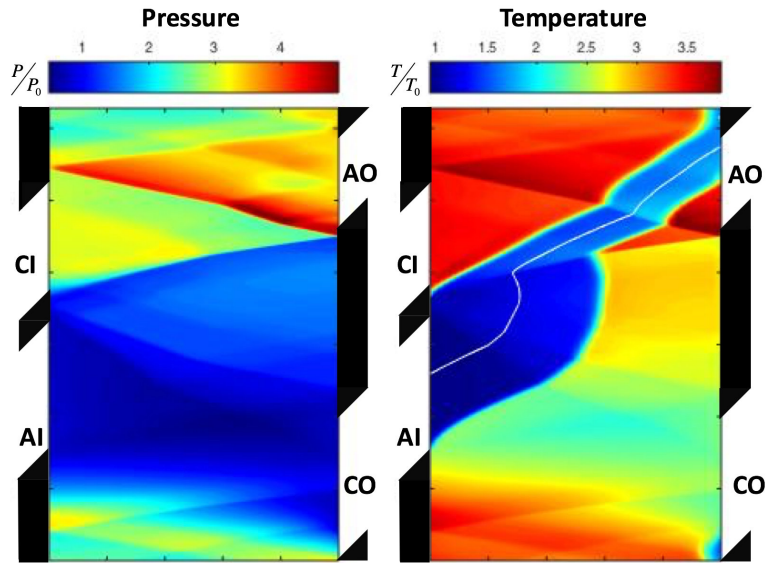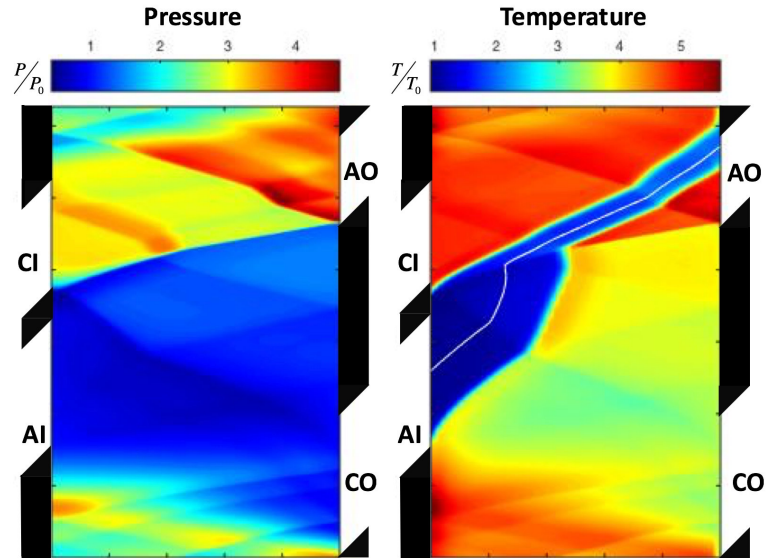| RPM | Air Mass Flow Rate (kg/min) | CO T (K) | CO P (kPa) | TI T (K) | TI P (kPa) | TO T (K) | TO P (kPa) | Power (W) |
|---|---|---|---|---|---|---|---|---|
| 26,950 | 1.61 | 678 | 350.0 | 1084 | 326.4 | 650 | 117.2 | 717 |
| 28,875 | 1.63 | 666 | 365.1 | 1031 | 335.8 | 683 | 121.7 | 954 |
| 30,800 | 1.63 | 671 | 371.3 | 1029 | 338.0 | 719 | 124.7 | 1137 |
| 32,725 | 1.64 | 693 | 369.4 | 1068 | 334.6 | 749 | 127.1 | 1289 |
| 34,650 | 1.63 | 727 | 371.5 | 1137 | 334.6 | 796 | 130.1 | 1498 |
| 36,575 | 1.61 | 759 | 377.0 | 1198 | 337.4 | 847 | 132.7 | 1702 |
| 38,500 | 1.59 | 786 | 384.1 | 1233 | 341.8 | 885 | 133.3 | 1782 |
| 40,425 | 1.57 | 817 | 393.8 | 1278 | 348.7 | 932 | 134.2 | 1897 |
| 42,350 | 1.55 | 853 | 400.5 | 1331 | 353.3 | 977 | 134.8 | 1989 |
| 44,275 | 1.52 | 898 | 410.7 | 1399 | 360.5 | 1,037 | 136.1 | 2141 |
| 46,200 | 1.50 | 942 | 416.9 | 1470 | 364.6 | 1,091 | 136.8 | 2257 |
| 48,125 | 1.48 | 990 | 422.7 | 1547 | 368.0 | 1,150 | 137.6 | 2389 |
| 50,050 | 1.46 | 1,022 | 420.1 | 1611 | 364.4 | 1,188 | 137.4 | 2245 |

# Bibliography

1. Paxson, D. E., "A General Numerical Model for Wave Rotor Analysis," *NASA Technical Manual 105740*, July 1992.

2. Paxson, D. E., "An Improved Numerical Model for Wave Rotor Design and Analysis," *AIAA Paper No. 1993-0482*, January 1993.

3. Paxson, D. E. and Wilson, J., "Recent Improvements to and Validation of the One Dimensional NASA Wave Rotor Model," *NASA Technical Manual 106913*, May 1995.

4. Mataczynski, M. R., Paxson, D. E., Polanka, M. D., and Hoke, J., "Experimental Performance of a Small Scale Pressure Wave Supercharger," *54th AIAA Aerospace Sciences Meeting, AIAA SciTech, San Diego, CA*, January 2016, AIAA Paper No. 2016-0768.

5. *Nees Seminar 20140822*, 2014, UNPUBLISHED.

6. Jacobson, S. A., "Aerothermal Challenges in the Design of a Microfabricated Gas Turbine Engine," 1998.

7. Mattingly, J. D., *Elements of Propulsion: Gas Turbines and Rockets*, AIAA, Washington D.C., 1987.

8. Bianchi, M., Pascale, A. D., and di Montenegro, G. N., "Micro Gas Turbine Repowering with Inverted Brayton Cycle," *ASME Turbo Expo 2005. Reno-Tahoe, NV*, July 2005, GT Paper No. 2005-68550.

9. Crosbie, S. C., Polanka, M. D., Litke, P. J., and Hoke, J. L., "Increasing Reliability of a Small 2-Stroke Internal Combustion Engine for Dynamically Changing Altitudes," *50th AIAA Aerospace Sciences Meeting, AIAA SciTech, Nashville, TN*, 2012, AIAA Paper No. 2012-0950.

10. Husaboe, T. D., Rittenhouse, J. A., Polanka, M. D., Litke, P. J., and Hoke, J. L., "Small Internal Combustion Engine Dependence on Inlet Pressure and Temperature at Altitude," *49th AIAA/ASME/SAE/ASEE Joint Propulsion Conference, San Jose, CA*, 2013, AIAA Paper No. 2013-3649.

11. Menon, S. and Cadou, C. P., "Scaling of Miniature Piston Engine Performance, Part 2: Overall Engine Performance," *Journal of Propulsion and Power*, Vol. 29, July-August 2013, DOI: 10.2514/1.B34639.

12. Ausserer, J. K., *The Scaling of Loss Pathways and Heat Transfer in Small Scale Internal Combustion Engines*, Ph.D. thesis, Air Force Institute of Technology, WPAFB OH, 2016, Sept. 2016.

13. Horn, K. P., Ausserer, J. K., Polanka, M. D., Litke, P. J., and Jr., K. D. G., "Dynamic Friction Measurements on a Small Engine Test Bench," *53rd AIAA Aerospace Sciences Meeting, AIAA SciTech Kissimmee, FL*, January 2015, AIAA Paper No. 2015-1474.

14. Menon, S. and Cadou, C. P., "Scaling of Miniature Piston Engine Performance, Part 1: Overall Engine Performance," *Journal of Propulsion and Power*, Vol. 29, July-August 2013, DOI: 10.2514/1.B34638.

15. Akbari, P., Nalim, M. R., and Mueller, N., "A Review of Wave Rotor Technology and Its Applications," *ASME Journal of Engineering for Gas and Turbine Power*, January 2006, DOI:10,1115/1.2204628.2006.

16. Snyder, P. H., Alparslan, B., and Nalim, M. R., "Gas Dynamic Analysis of the CVC, A Novel Detonation Cycle," *38th AIAA/ASME/SAE/ASEE Joint Propulsion Conference, Indianapolis, IN*, July 2002, AIAA Paper No. 2002-4069.

17. Wilson, J., Welch, G. E., and Paxson, D. E., "Experimental Results of Performance Tests on a Four-Port Wave Rotor," *AIAA Paper No. 2007-1250*, January 2007.

18. Welch, G. E., "Wave Engine Topping Cycle Assessment," January 2007, AIAA Paper No. 97-0707.

19. Mataczynski, M. R., Polanka, M. D., Paxson, D. E., and Nees, J. B., "Testing and Simulation of a Small-Scale Pressure Wave Supercharger," *53rd AIAA Aerospace Sciences Meeting, AIAA SciTech Kissimmee, FL*, January 2015, AIAA Paper No. 2015-1345.

20. Smith, B. D., Polanka, M. D., Paxson, D. E., and Hoke, J. L., "Scaling Study of Wave Rotor Turbo Normalization of an Internal Combustion Engine," *41st AIAA/ASME/SAE/ASEE Joint Propulsion Conference, Atlanta, GA*, July-August 2012, AIAA Paper No. 2012-3837.

21. Mataczynski, M. R., *Design and Simulation of a Pressure Wave Supercharger for a Small Two-Stroke Engine*, Master's thesis, Air Force Institute of Technology, WPAFB, OH, 2014, AFIT-ENY-14-M-34.

22. Knauff, R., "Converting Pressures of Liberated Gas Energy into Mechanical Work," 1906, Patent No. 2818.

23. Burghard, H., 1913, Patent No. 19421.

24. Lebre, A. F., 1928, Patent No. 290669.

25. Nalim, M. R., "Assessment of Combustion Modes for Internal Combustion Wave Rotors," *ASME Journal of Engineering for Gas and Turbine Power*, Vol. 121, April 1999.

166

26. Nalim, M. R., Li, H., and Akbari, P., "Air-Standard Aerothermodynamic Analysis of Gas Turbine Engines with Wave Rotor Combustion," *ASME Journal of Engineering for Gas and Turbine Power*, Vol. 131, September 2009.

27. Snyder, P. H., Elharis, T. M., S. D. Wijeyakulasuriya, M. R. N., Matsutomi, Y., and Meyer, S. E., "Pressure Gain Combustor Component Viability Assessment Based on Initial Testing," *47th AIAA/ASME/SAE/ASEE Joint Propulsion Conference, San Diego, CA*, July-August 2011, AIAA Paper No. 2011-5749.

28. Akbari, P. and Mueller, N., "A Review of Wave Rotor Technology and Its Applications," *ASME Journal of Engineering for Gas and Turbine Power*, Vol. 128, January 2006, DOI:10,1115/1.2204628.2006.

29. Smith, B. D., *Scaling Study of Wave Rotor Turbo-Normalization of a Small Internal Combustion Engine*, Master's thesis, Air Force Institute of Technology, WPAFB, OH, 2012, AFIT/GAE/ENY/12-S48.

30. Diehl, L. A. and Biaglow, J. A., "Swirl-Can Combustor Performance to Near-Stoichiometric Fuel-Air Ratio," 1976, ASME Paper No. 76-FT-10.

31. Bicen, A. F., Tse, D. G. N., and Whitelaw, J. H., "Combustion Characteristics of a Model Can-Type Combustor," *Combustion and Flame*, Vol. 80, 1990, pp. 111-125.

32. Goebel, S. G., Abuaf, N., Lovett, J. A., and Lee, C. P., "Measurements of Combustor Velocity and Turbulence Profiles," *ASME 1993 International Gas Turbine and Aeroengine Congress and Exposition*, 1993, ASME Paper No. 93-GT-228.

33. *The Jet Engine*, Rolls Royce plc, Derby, England, 1996, 5th Edition.

34. Turns, S. R., *An Introduction to Combustion*, McGraw-Hill, Inc, New York, 1996, 2nd Edition.

35. Weigand, P., W. Meier, X. D., Stricker, W., and Aigner, M., "Investigations of swirl flames in a gas turbine model combustor I. Flow field, structures, temperature, and species distributions," *Combustion and Flame*, Vol. 144, September 2006.

36. Weigand, P., W. Meier, X. D., Stricker, W., and Aigner, M., "Investigations of swirl flames in a gas turbine model combustor II. Turbulencechemistry interactions," *Combustion and Flame*, Vol. 144, September 2006.

37. Howard, S. A., Bruckner, R. J., DellaCorte, C., and Radil, K. C., "Gas Foil Bearing Technology Advancements for Closed Brayton Cycle Turbines," *NASA TM-2007-214470*, 2007.

167

38. Agrawal, G. L., "Foil Air/Gas Bearing Technology-An Overview," *American Society of Mechanical Engineers International Gas Turbine and Aeroengine Congress and Exhibition. Orlando, FL*, June 1997, ASME Paper No. 97-GT-347.

39. Kim, D. and Soongook, P., "Hydrostatic air foil bearings: Analytical and experimental investigation," *Tribology International*, Vol. 42, 2009, pp. 413-425.

40. Kim, D. and McClearn, M. J., 2015, Personal Communication about Air Bearings.

41. Paxson, D. E. and McClearn, M. J., 2015, Personal Communication about Code Usage.

42. Wheeler, A. J. and Ganji, A. R., *Introduction to Engineering Experimentation*, Pearson Eduction, Inc, Upper Saddle River, NJ 07458, 2004, 2nd Edition.

# REPORT DOCUMENTATION PAGE

**Form Approved**
**OMB No. 0704–0188**

The public reporting burden for this collection of information is estimated to average 1 hour per response, including the time for reviewing instructions, searching existing data sources, gathering and maintaining the data needed, and completing and reviewing the collection of information. Send comments regarding this burden estimate or any other aspect of this collection of information, including suggestions for reducing this burden to Department of Defense, Washington Headquarters Services, Directorate for Information Operations and Reports (0704–0188), 1215 Jefferson Davis Highway, Suite 1204, Arlington, VA 22202–4302. Respondents should be aware that notwithstanding any other provision of law, no person shall be subject to any penalty for failing to comply with a collection of information if it does not display a currently valid OMB control number. **PLEASE DO NOT RETURN YOUR FORM TO THE ABOVE ADDRESS.**

| 1. REPORT DATE *(DD–MM–YYYY)* | 2. REPORT TYPE | 3. DATES COVERED *(From — To)* |
|---|---|---|
| 01-08-2014 | Masters' Thesis | Sept 2014 — Jun 2016 |

**4. TITLE AND SUBTITLE**

DESIGN, MANUFACTURING, AND TESTING OF A SMALL THROUGH-FLOW WAVE ROTOR FOR USE WITHIN THE BRAYTON CYCLE

**5a. CONTRACT NUMBER**

**5b. GRANT NUMBER**

**5c. PROGRAM ELEMENT NUMBER**

**6. AUTHOR(S)**

Michael J. McClearn, 2d Lt, USAF

**5d. PROJECT NUMBER**

**5e. TASK NUMBER**

**5f. WORK UNIT NUMBER**

**7. PERFORMING ORGANIZATION NAME(S) AND ADDRESS(ES)**

Air Force Institute of Technology
Graduate School of Engineering and Management (AFIT/EN)
2950 Hobson Way
WPAFB OH 45433-7765

**8. PERFORMING ORGANIZATION REPORT NUMBER**

AFIT-ENY-MS-16-J-054

**9. SPONSORING / MONITORING AGENCY NAME(S) AND ADDRESS(ES)**

Mass. Institute of Technology, Lincoln Labs
Dr. Marc Viera, mviera@ll.mit.edu, 781-981-1077
244 Wood Street, Lexington, MA 02420-9108

**10. SPONSOR/MONITOR'S ACRONYM(S)**

MIT-LL

**11. SPONSOR/MONITOR'S REPORT NUMBER(S)**

**12. DISTRIBUTION / AVAILABILITY STATEMENT**

DISTRIBUTION STATEMENT A:
APPROVED FOR PUBLIC RELEASE; DISTRIBUTION UNLIMITED.

**13. SUPPLEMENTARY NOTES**

**14. ABSTRACT**

With the ever growing popularity of drones and other unmanned aerial vehicles for military, commercial, and private usage, their is a desire to improve performance in terms of range, altitude, and flight speed. Current technology uses either electric motors or internal combustion engines: both piston and jet engine types. These sorts of engines undergo significant efficiency degradation as their size decreases. While some efficiency may be recovered via intensive design studies, they are approaching the limit to their operating physics. A possible solution to this is to change these physics to something more immune to scaling losses; a pressure exchange device known as a wave rotor does just that. A wave rotor operates via oscillating pressure waves in order to compress the gas as opposed to the mechanical compression utilized by conventional engines. This thesis outlines the design, manufacture, and component testing of a wave rotor within the Brayton cycle. While the focus of this research was the wave rotor, included in the design and testing were the many support components necessary to drive the cycle, notably including a small can-type combustor. By using a NASA developed quasi one dimensional CFD code, the wave rotor cycle was designed to power Class 2 UAVs as kilowatt class combustion engine. After the CFD modeling, hardware design and manufacture began on the various components. When the manufacturing was completed, the various components were tested including the venturis, the combustor, and the wave rotor itself. The component testing showed great promise for the full rig testing. Hardware build up and the test plan to test this is ongoing but expected to show efficiency gains when compared to similar sized combustion engines. Improved efficiency gains will significantly decrease operating costs of small drones while improving range and altitude performance to all operators.

**15. SUBJECT TERMS**

Brayton Cycle, Wave Rotor, Can-Combustor, RPA, UAV

| 16. SECURITY CLASSIFICATION OF: | | | 17. LIMITATION OF ABSTRACT | 18. NUMBER OF PAGES | 19a. NAME OF RESPONSIBLE PERSON |
|---|---|---|---|---|---|
| a. REPORT | b. ABSTRACT | c. THIS PAGE | | | Dr. M. D. Polanka, AFIT/ENY |
| U | U | U | U | 166 | **19b. TELEPHONE NUMBER** *(include area code)* (937) 255-3636, x4714; marc.polanka@afit.edu |

**Standard Form 298 (Rev. 8–98)**
Prescribed by ANSI Std. Z39.18